A LOW-DRIFT SILICON MEMS RESONANT ACCELEROMETER

A THESIS SUBMITTED TO
THE GRADUATE SCHOOL OF NATURAL AND APPLIED SCIENCES
OF
MIDDLE EAST TECHNICAL UNIVERSITY

BY

HASAN DOĞAN GAVCAR

IN PARTIAL FULFILLMENT OF THE REQUIREMENTS
FOR
THE DEGREE OF DOCTOR OF PHILOSOPHY
IN
ELECTRICAL AND ELECTRONIC ENGINEERING

JANUARY 2023

Approval of the thesis:

A LOW-DRIFT SILICON MEMS RESONANT ACCELEROMETER

submitted by **HASAN DOĞAN GAVCAR** in partial fulfillment of the requirements for the degree of **Doctor of Philosophy** i**n Electrical and Electronic Engineering, Middle East Technical University** by,

Prof. Dr. Halil Kalıpçılar
Dean, Graduate School of **Natural and Applied Sciences** _____

Prof. Dr. İlkay Ulusoy
Head of the Department, **EEE, METU** _____

Prof. Dr. Tayfun Akın
Supervisor, **EEE, METU** _____

Examining Committee Members:

Prof. Dr. Haluk Külah
Electrical and Electronics Eng., METU _____

Prof. Dr. Tayfun Akın
Electrical and Electronics Eng., METU _____

Assoc. Prof. Dr. Kıvanç Azgın
Mechanical Engineering, METU _____

Asst. Prof. Dr. Erdinç Tatar
EEE, Bilkent University _____

Asst. Prof. Dr. Serdar Tez
EEE, Pamukkale University _____

Date: 23.01.2023

I hereby declare that all information in this document has been obtained and presented in accordance with academic rules and ethical conduct. I also declare that, as required by these rules and conduct, I have fully cited and referenced all material and results that are not original to this work.

Name Last name : Hasan Doğan Gavcar

Signature :

ABSTRACT

A LOW-DRIFT SILICON MEMS RESONANT ACCELEROMETER

Gavcar, Hasan Doğan
Doctor of Philosophy, Electrical and Electronic Engineering
Supervisor: Prof. Dr. Tayfun Akın

January 2023, 142 pages

This thesis presents the design, fabrication, and experimental verification of low temperature drift silicon resonant accelerometers for tactical grade applications. The working principle of a silicon resonant accelerometer is based on force sensing, in which the sensor output is a frequency proportional to the input acceleration. The stress-insensitive sensor design prevents the thermal stress produced by the mismatch of the thermal expansion coefficients (CTE) of glass and silicon from transmitting to the DETF resonators.

In the scope of this thesis, three different silicon resonant accelerometer structures are sequentially designed, fabricated, characterized, and tested with the frequency readout circuit. The first sensor structure consists of two differential DETF resonators and a large proof mass connected to a stationary outer frame. The second sensor structure utilizes microlevers to magnify the inertial force acting on the DETF resonators in addition to the sensor frame of the first sensor structure. Although specially designed stress release beams are implemented in the first and second sensor structures, they suffer from thermal stress caused by the stationary outer frame after fabrication. In the third sensor design, the sensor structure is placed on a

specially designed single anchor to overcome the stress problem encountered in the first two sensor designs. The FEM simulations are performed to analyze and optimize the mode shapes, force sensitivity, and temperature sensitivity of the sensor structures. The designed resonant accelerometers are fabricated using the aMEMS1 process with wafer-level hermetic encapsulation. The fabricated sensor chips are integrated with the capacitive preamplifier and digital signal processor (DSP)-based phase-locked-loop (PLL) system implemented on a Zurich Instrument HF-2 lock-in amplifier. The functionalities of the accelerometers are verified by the resonance and 4-point tumble tests, and their performances are experimentally evaluated in terms of thermal sensitivity and bias stability by temperature and Allan variance tests.

Test results show that the single-anchor silicon resonant accelerometer achieves a bias instability of 1.25 μg, a bias stability of 2.8 μg, a bias repeatability of 6.6 μg, a velocity random walk of 6.1 μg/√Hz for the sensor bandwidth of 33 Hz at room temperature, and a maximum bias change of 4.3 mg for the temperature range from -40 °C to +85 °C. It has a measurement range up to ±60 g with a 500-ppm deviation from the linear scale range. Compared to the commercial capacitive MEMS accelerometer developed by Mikrosistemler, the silicon resonant accelerometer developed in this work exhibits at least a 20-fold improvement in bias temperature sensitivity, a 7-fold improvement in bias instability, a 112-fold improvement in bias stability, and a 2-fold improvement in noise floor. More importantly, although the bias of the commercial capacitive MEMS accelerometer tested in this study moves 1.7 mg in 50 minutes at constant 25°C, the bias of the silicon resonant accelerometer shifts less than 0.25 mg in 10 hours at ambient temperature.

Keywords: MEMS, Resonant Accelerometer, Bias Drift, Temperature Sensitivity

ÖZ

DÜŞÜK SABİT KAYMA HATASI KAYMASINA SAHİP SİLİSYUM TABANLI REZONANT İVMEÖLÇER

Gavcar, Hasan Doğan
Doktora, Elektrik ve Elektronik Mühendisliği
Tez Yöneticisi: Prof. Dr. Tayfun Akın

Ocak 2023, 142 sayfa

Bu tez çalışması, taktik seviye uygulamalar için sabit kayma hatası sıcaklıkla az değişen silisyum tabanlı rezonant ivmeölçerlerin tasarımını, üretimini ve deneysel olarak doğrulanmasını sunmaktadır. Silisyum tabanlı rezonant ivmeölçerin çalışma prensibi kuvvet algılamaya dayanmaktadır ve sensör çıkışı uygulanan ivme ile değişen bir frekans değeridir. Stresten etkilenmeyen bir sensör tasarımı, silisyum ile camın sıcaklıkla genleşme katsayısı farkından dolayı oluşan stresin ivmeye duyarlı rezonatörleri etkilemesini önler.

Bu tez kapsamında, üç farklı silisyum tabanlı rezonant ivmeölçer yapısı tasarlanmış, üretilmiş karakterize edilmiş ve frekans okuma devresi ile test edilmiştir. İlk sensör tasarımı, diferansiyel olarak yerleştirilmiş iki adet rezonatör ve sabit bir dış çerçeveye bağlı büyük bir ataletsel kütleden oluşmaktadır. İkinci sensör yapısı ise, ilk sensör yapısına ek olarak algılama yapan rezonatöre etkiyen kuvveti artırmayı sağlayan mikro kaldıraç yapılarını içermektedir. İlk iki sensör yapısı stresi sönümleyen özel tasarlanmış yaylar içermesine rağmen, üretim sonrası sabit dış çerçevenin ataletsel kütle üzerinde yarattığı stresten oldukça etkilenmiştir. Üçüncü

sensör yapısında, ilk iki sensör tasarımında karşılaşılan stres problemini ortadan kaldırmak amacıyla ataletsel kütle tek bir sabit çapa üzerine özel bir şekilde yerleştirilmiştir. Sensör tasarımları sonlu elemanlar yöntemi ile mod yapıları, ivme hassasiyeti ve sıcaklık hassasiyeti bakımından simüle edilmiştir. Tasarlanan sensörler aMEMS1 üretim prosesi ile pul seviyesi vakum paketlenerek üretilmiştir. Üretilen sensör çipleri, kapasitif ön okuma devresi ve sayısal işaret işleyici tabanlı faz kilitlemeli döngü devresi ile birleştirilmiştir. İvmeölçerlerin fonksiyonelliği rozanans ve döndürerek yer çekimi ivmesi uygulama testleri ile doğrulanmış, performans değerleri ise sıcaklık ve Allan varyans testleri ile sabit kayma hatası kararlılığı ve sıcaklıkla değişimi bakımından ölçülmüştür.

Test sonuçlarına göre, tek çapa yapısına sahip silisyum tabanlı rezonant ivmeölçerin oda sıcaklığında, 33 Hz bant genişliği için sabit kayma hatası kararsızlığı değeri 1.25 µg, sabit kayma hatası kararlılığı değeri 2.8 µg, sabit kayma hatası tekrarlanabilirliği değeri 6.6 µg, hız rastgele yürüyüş hatası değeri 6.1 µg/√Hz, -40 °C ile +85 °C arasında sabit kayma hatasının sıcaklıkla maksimum değişimi 4.3 mg'dir. Tasarlanan sensör ölçüm aralığı, 500-ppm doğruluktan sapma sınırı içinde minimum ±60g'ye kadardır. Elde edilen sonuçlar Mikrosistemlerin ürün olarak geliştirdiği kapasitif MEMS ivmeölçerler ile karşılaştırıldığında, sabit kayma hatasının sıcaklıkla değişiminde en az 25 kat, sabit kayma hatası karasızlığı değerinde 7 kat, sabit kayma hatası kararlılığı değerinde 112 kat, gürültü değerinde ise 2 kat iyileşme vardır. Daha da önemlisi, test edilen kapasitif MEMS ivmeölçerin sabit kayma hatası değeri kontrollü 25 °C sıcaklıkta 50 dakika içinde 1.7 mg kayarken, bu çalışmada geliştirilen silisyum tabanlı rezonant ivmeölçerin sabit kayma hatası değeri sıcaklık kontrolsüz ortamda 10 saat sonunda 0.25 mg'den daha az kaymaktadır.

Anahtar Kelimeler: MEMS, Rezonans Tabanlı İvmeölçer, Sabit Kayma Hatsı Kayması

Dedicated to those who care

ACKNOWLEDGMENTS

First of all, I would like to thank my thesis advisor Prof. Dr. Tayfun Akın for his support, guidance, and encouragement during my graduate studies. It is a great chance for me to do research with him.

I also would like to thank Prof. Dr. Haluk Külah and Assoc. Prof. Dr. Kıvanç Azgın for their comments and suggestions during the development of this thesis.

Special thanks to Dr. Said Emre Alper and Ferhat Yeşil for sharing their deep knowledge and experiences in all phases of this research, and also for their friendship. I would like to express my gratitude to Taylan Töral for his help in the fabrication and his friendship.

I would like to express my gratitude to Dr. M. Mert Torunbalcı, Gülşah Demirhan, Orhan Şevket Akar, Selçuk Keskin, Gürkan Gök, Fikret Tatar, Evren Erdil, Dr. Mustafa Yıldırım, Adem Saraç for their supportive friendship throughout this thesis process. I am also very grateful to Büşra Erdoğan, Seval Şahin, Orçun Şengöz and Sedat Mert for their sincere friendship during the writing phase of this thesis.

I would like to thank to Mikrosistemler staff for their helps during the chip fabrication and test phases of this study, especially to İsmail Gökşen. I also would like to thank all members of the METU-MEMS family for providing a nice research environment.

I would like to express my deepest gratitude to my parents for their endless support, love, and encouragement throughout my whole life.

TABLE OF CONTENTS

ABSTRACT v

ÖZ vii

ACKNOWLEDGMENTS x

TABLE OF CONTENTS xi

LIST OF TABLES xiv

LIST OF FIGURES xvi

LIST OF ABBREVIATIONS xx

CHAPTERS

1 INTRODUCTION 1

1.1 Operation Principle of Silicon Resonant Accelerometers 3

1.2 Metrics and Performance Grades of Accelerometers 4

1.3 Challenges for Silicon Resonant Accelerometers 8

1.4 Overview of Silicon Resonant Accelerometers 9

1.5 Silicon Resonant Accelerometers Developed in This Thesis Study 18

1.6 Research Objectives and Thesis Outline 20

2 MECHANICAL DESIGN OF SILICON RESONANT ACCELEROMETER 23

2.1 Mechanical Model of Silicon Resonant Accelerometer 23

2.1.1 Force Sensitivity of DETF Resonator 25

2.1.2 Microlever Mechanism and System Amplification Factor 28

2.1.3 Scale Factor of Overall System 31

2.1.4 Stiffness Nonlinearity 33

2.1.5 Temperature Sensitivity and Thermal Stress 35
2.1.6 Capacitive Actuation and Sensing Mechanism 37
2.2 Designs of Silicon Resonant Accelerometers for This Thesis Work 38
2.3 Finite-Element Simulations 44
2.3.1 Modal Analysis of DETF Resonator 45
2.3.2 Modal Analysis of Silicon Resonant Accelerometer Designs 47
2.3.3 Force Simulations 55
2.3.4 Temperature Simulations 61
2.4 Summary 63
3 FABRICATION OF MEMS RESONANT ACCELEROMETERS 65
3.1 Advanced MEMS1 (aMEMS1) Process with Anodic Bonding 65
3.1.1 Sensor Wafer Fabrication Based on the SOG Process 65
3.1.2 Wafer-Level Hermetic Packaging of Silicon MEMS Resonant Accelerometers 69
3.2 Fabrication Results 73
3.3 Summary 78
4 CONTROL ELECTRONICS FOR SILICON RESONANT ACCELEROMETERS 79
4.1 General Block Diagram of Control Electronics for Silicon Resonant Accelerometer 79
4.2 Analog Front-End Electronics 81
4.3 Phase-Locked Loop 82
4.4 Automatic Amplitude Control Circuit 85
4.5 Summary 91
5 TEST RESULTS 93

5.1 Resonance Characterization of the Silicon Resonant Accelerometers..... 94
5.2 Test Set-up for the System Level Tests of the Silicon Resonant Accelerometers..... 98
5.3 4-Point Tumble Test for Scale Factor Measurements..... 100
5.4 Temperature Tests..... 106
5.5 Allan Variance and Bias Repeatability Tests..... 114
5.6 Summary of Test Results..... 120
6 CONCLUSION.....123
REFERENCES 131
CURRICULUM VITAE.....141

LIST OF TABLES

TABLES

Table 1.1 Accelerometer specifications for missile guidance and high-performance navigation [8]. 7
Table 2.1 Sensor design parameters for SRA Design-1. 43
Table 2.2 Sensor design parameters for SRA Design-2. 43
Table 2.3 Sensor design parameters for SRA Design-3. 44
Table 2.4 Modal analysis results of the SRA Design-1. 48
Table 2.5 Modal analysis results of the SRA Design-2. 50
Table 2.6 Modal analysis results of the SRA Design-3. 53
Table 2.7 Force simulation results for SRA Design-1 in COMSOL. 55
Table 2.8 Force simulation results for SRA Design-2 in COMSOL. 57
Table 2.9 Force simulation results for SRA Design-3 in COMSOL. 59
Table 2.10 Temperature simulation results for three different conditions of SRA Design-3 in COMSOL. 62
Table 4.1: Sensor and circuit parameters used for the design of automatic gain control loop of the accelerometer Acce#4 for 10V proof mass voltage (for one resonator). 88
Table 5.1 List of the silicon resonant accelerometer sensors tested in this study. .. 93
Table 5.2 Resonance characteristics of the DETF resonators of the silicon resonant accelerometers. 96
Table 5.3 Results for the scale factor measurements of the silicon resonant accelerometers. 104
Table 5.4 Results for the cross-axis sensitivity or the equivalent axis-misalignment measurements for the silicon resonant accelerometers. 105
Table 5.5 Temperature test results of the silicon resonant accelerometers. 113
Table 5.6 Bias repeatability test results of the evaluated accelerometers. 118
Table 5.7 Comparison of the Allan variance results of the accelerometers 120
Table 5.8 Summary of the test results of the accelerometers. 121

Table 6.1 Comparison between this work and results in the literature. 130

LIST OF FIGURES

FIGURES

Figure 1.1. The structural diagram of a silicon resonant accelerometer. 3
Figure 1.2. Accelerometer performance grades [7]. 7
Figure 1.3. The geometry of silicon resonant accelerometer developed by Draper Laboratory [8]. 11
Figure 1.4. The SEM image of the fabricated laterally-driven resonant silicon accelerometer developed by Seoul National University [15]. 12
Figure 1.5. The SEM picture of the resonant accelerometer using a single-anchor point developed by Stanford University [22]. 13
Figure 1.6. The SEM picture of the silicon resonant accelerometer with a stress isolation frame [45]. 16
Figure 1.7. The silicon resonant accelerometer structure mounted on single anchored isolation frame [48]. 17
Figure 1.8. Simplified structural view of the “SRA Design-1” accelerometer. 18
Figure 1.9. Simplified structural view of the “SRA Design-2” accelerometer. 19
Figure 1.10. Simplified structural view of the “SRA Design-3” accelerometer. 20
Figure 2.1. The structure of the silicon resonant accelerometer utilizing micro levers. 24
Figure 2.2. Simple model of DETF resonator consisting of two flexure beams. 27
Figure 2.3. Simple model of microlever structure. 28
Figure 2.4. The axial spring model of the DETF resonator integrated to the lever structure. 30
Figure 2.5. The relation between the resonator frequency and input acceleration. . 33
Figure 2.6. The mechanical structure of the “SRA Design-1”. 40
Figure 2.7. The mechanical structure of the “SRA Design-2”. 41
Figure 2.8. The mechanical structure of the “SRA Design-3”. 42
Figure 2.9. The in-phase mode of DETF in COMSOL: 22849Hz. 46
Figure 2.10. The out-of-phase mode of DETF in COMSOL: 24316Hz. 46

Figure 2.11. The mode shapes for SRA Design-1. 49
Figure 2.12. The mode shapes for SRA Design-2. 52
Figure 2.13. The mode shapes for SRA Design-3. 54
Figure 2.14. Responses of the SRA Design-1 to the accelerations applied along the measurement axis in FEM simulations. 56
Figure 2.15. Responses of the SRA Design-2 to the accelerations applied along the measurement axis in FEM simulations. 58
Figure 2.16. Responses of the SRA Design-3 to the accelerations applied along the measurement axis in FEM simulations. 60
Figure 2.17. Change of the DETF resonator frequency with temperature for SRA Design-3 under three different conditions in FEM simulations..... 63
Figure 3.1: Fabrication process of the silicon resonant accelerometer wafer. 69
Figure 3.2: Fabrication process for wafer-level hermetic packaging of the sensor wafer with the SOI cap wafer. 72
Figure 3.3: SEM pictures of the first silicon resonant accelerometer design, i.e., SRA-Design-1, fabricated using aMEMS1 process..... 73
Figure 3.4: SEM pictures of the second silicon resonant accelerometer design, i.e., SRA-Design-2, fabricated using aMEMS1 process..... 74
Figure 3.5: Deflection and crack on the springs connecting the proof mass to the outer frame. 75
Figure 3.6: SEM pictures of the third silicon resonant accelerometer design, i.e., SRA-Design-3, fabricated using aMEMS1 process..... 76
Figure 3.7: SEM picture of comb fingers and DETF flexure after the fabrication. 77
Figure 3.8: Top and bottom side pictures of the fabricated silicon resonant accelerometer using aMEMS1 process. 78
Figure 4.1: Block diagram of the control electronics for the silicon resonant accelerometer implemented on the lock-in amplifier. 80
Figure 4.2: Schematic of the front-end circuit. 82
Figure 4.3: Block diagram of a PLL. 83
Figure 4.4: Step response of the closed-loop PLL controller. 84

Figure 4.5: Block diagram of the closed-loop automatic gain control unit. 86
Figure 4.6: Schematic of signal conversions during the resonance test of DETF resonator of the silicon resonant accelerometer. 87
Figure 4.7: Step response of the closed-loop automatic controller. 89
Figure 4.8: SIMULINK model for the automatic gain control system of the DETF resonator. 90
Figure 4.9: Front-end output and displacement signals of the simulated DETF resonator. 90
Figure 5.1: Die-level resonance test setup of the fabricated silicon resonant accelerometer. 94
Figure 5.2: Silicon resonant accelerometer integrated to the front-end electronics: (a) top and (b) bottom view. 95
Figure 5.3: Resonance characteristics of the DETF Resonator-1 of the accelerometer Acce#4 for different proof mass voltages. 97
Figure 5.4: Resonance characteristics of the DETF Resonator-2 of the accelerometer Acce#4 for different proof mass voltages. 98
Figure 5.5: Test set-up with the lock-in amplifier for the system-level tests of the silicon resonant accelerometers. 99
Figure 5.6: Schematic of test set-up for the 4-point tumble test. 100
Figure 5.7: The differential DETF resonator outputs of the accelerometer Acce#1 as a response to the different gravity loads in the tumble test. 101
Figure 5.8: The differential DETF resonator outputs of the accelerometer Acce#2 as a response to the different gravity loads in the tumble test. 102
Figure 5.9: The differential DETF resonator outputs DETF resonators of the accelerometer Acce#3 as a response to the different gravity loads in the tumble test. 103
Figure 5.10: The differential DETF resonator outputs DETF resonators of the accelerometer Acce#4 as a response to the different gravity loads in the tumble test. 104

Figure 5.11: Test set-up for the temperature test of the silicon resonant accelerometers. 106
Figure 5.12: Temperature characteristics of the accelerometer Acce#1. 109
Figure 5.13: Temperature characteristics of the accelerometer Acce#2. 110
Figure 5.14: Temperature characteristics of the accelerometer Acce#3. 111
Figure 5.15: Temperature characteristics of the accelerometer Acce#4. 112
Figure 5.16: Temperature characteristics of a typical commercial MEMS accelerometer developed by Mikrosistemler for the temperature range from -32°C to +55 °C. 113
Figure 5.17: A general Allan variance plot for accelerometer. 114
Figure 5.18: Allan Variance plots of the accelerometer Acce#1 and Acce#2 at room temperature. 115
Figure 5.19: Allan Variance plots of the accelerometer Acce#3 and Acce#4 for 10 hour-data at room temperature. 116
Figure 5.20: Allan Variance plot of the capacitive MEMS accelerometer at 25°C in the temperature-controlled environment. 117
Figure 5.21: Comparison of the raw data of SRA Design-3 accelerometers and the typical commercial capacitive MEMS accelerometer developed by Mikrosistemler. 119

LIST OF ABBREVIATIONS

MEMS	Micro Electro Mechanical System
SRA	Silicon Resonant Accelerometer
DETF	Double Ended Tuning Fork
aMEMS1	Advanced MEMS
SOG	Silicon-on-Glass
SOI	Silicon-on-Insulator
DRIE	Deep Reactive Ion Etching
CTE	Coefficient of Thermal Expansion
PLL	Phase Locked Loop
DSP	Digital Signal Processor
PI	Proportional-Integral
PCB	Printed Circuit Board
SNR	Signal-to-Noise-Ratio
IC	Integrated Circuit

CHAPTER 1

INTRODUCTION

Micro-electro-mechanical systems (MEMS) refer to microdevices or systems which integrate microtransducers, microactuators, and microstructures with signal processing and control circuits. Their manufacturing process originates from the fabrication technology of integrated circuits (IC). Over the last three decades, continuous developments in microelectronic and micromachining technologies have generated precise, compelling, and advanced microsystems for applications in a wide range of fields, including consumer products, agriculture, food industry, automation, bioengineering, and even military electronic products [1]. Compared to bulky traditional sensors, MEMS products provide lower cost, smaller size, higher reliability, and compatibility with high-volume batch fabrication. Thus, they have already taken the place of their macro-scale counterparts in low-to-medium-end applications and drive the market for new products such as smart glasses, smart phones, self-driving cars, and drones. Rising popularity of the Internet of Things (IoT), strong demand in the automation area, and advancements in the portable electronics market all contribute to the expansion of the overall MEMS sensor industry [2]. MEMS inertial sensors, particularly micro accelerometers and micro gyroscopes, are located at the core of this technology transformation.

Since the commercialization of MEMS accelerometers in the 1990s, they have enabled unique features and applications in consumer, automotive, and industrial applications such as automotive airbag systems, platform stability, and motion sensing. With the rapid growth of micromachining technologies, tactical and navigation-grade MEMS accelerometers have been developed for high-end applications including gravimetry, inertial navigation, and seismometry. There are

various types of MEMS accelerometers based on their operating principles, such as capacitive, piezoresistive, optical, piezoelectric, or resonant beam accelerometers. Research on capacitive MEMS accelerometers has been intensely conducted for tactical-grade applications since the early 2000s in the METU-MEMS Center [3]. Although these sensors have reached performance values below 20 μg/Hz of velocity random walk, they have suffered from the long-term drift of bias, which restrains their utilization in long-term flight control and navigation. The temperature drift characterization and day-to-day repeatability of an accelerometer are vital for the reliability of many systems requiring high performance. On the other hand, silicon-based MEMS resonant accelerometers are promising for high-end applications due to their high-sensitivity, wide dynamic range, and direct frequency-to-digital conversion [4]. The need for low-drift MEMS accelerometers and the inadequacy of capacitive MEMS accelerometers to meet this demand force the research towards developing a low-drift silicon-based resonant accelerometer to replace the capacitive ones in short-term and long-term navigation applications.

This thesis reports the design and implementation of a low-temperature drift silicon MEMS resonant accelerometer. The stress induced by the thermal expansion coefficient difference between the silicon and glass is minimized by placing the sensor structure on a specially designed single anchor. The sensors are fabricated using the aMEMS1 process with vacuum packaging [5] and experimentally verified in terms of bias stability and thermal sensitivity.

The content of this chapter is as stated below: Section 1.1 presents the overview of the silicon-resonant accelerometer. Section 1.2 briefly gives the performance parameters and grades of accelerometers. Section 1.3 mentions the challenges for the development of high-performance silicon resonant accelerometers. Section 1.4 provides the literature review for the silicon resonant accelerometers. Section 1.5 introduces the silicon resonant accelerometer structures designed in this work. Section 1.6 gives the research goals and the organization of the thesis.

1.1 Operation Principle of Silicon Resonant Accelerometers

Micromechanical silicon resonant accelerometer (SRA) belongs to the accelerometer class known as vibration beam accelerometer (VBA), whose direct output is a frequency proportional to the input acceleration. The working principle of silicon resonant accelerometers are based on force sensing. Figure 1.1 shows a simplified structural view of a silicon resonant accelerometer. In most SRAs, two identical double-ended tuning fork (DETF) resonators are connected to a single proof mass such that the proof mass axially loads to the resonator pairs. Each DETF resonator is kept vibrating at its out-of-phase mode natural frequency by electrostatic actuation. Under the applied load, the accelerating proof mass loads one resonator in tension while loading the other one in compression. As a result, the tension loading increases the resonance frequency of one resonator, and the compression loading decreased the resonance frequency of the other resonator. The acceleration is measured by taking frequency difference of two DETF resonators.

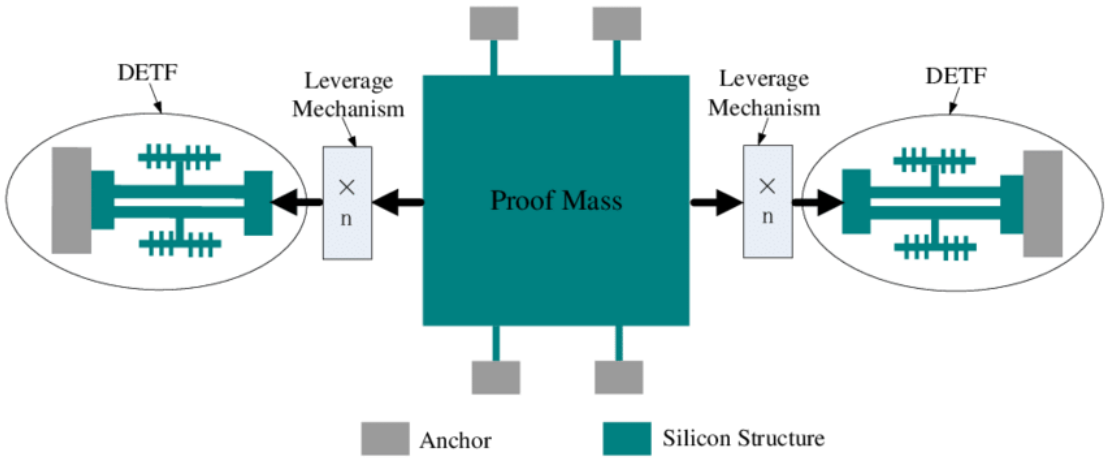


Figure 1.1. The structural diagram of a silicon resonant accelerometer.

A differential configuration doubles the mechanical sensitivity to the acceleration and suppresses common-mode error such as temperature, nonlinearity and off-axis

acceleration. The movable proof mass is connected to the stationary anchors with beams. The beams are flexible in the direction of the input axis, but they are rigid along the other axes so that the proof mass can move only along the sense axis.

Utilizing a microlever mechanism in the device structure may greatly decrease the dimension of the proof mass while maintaining high sensitivity. In a microlever mechanism, mechanical translation is accomplished by elastic deformation of its flexure beams. A pin-joint allowing for free rotation may be used to create a pivot structure like in the macroworld.

1.2 Metrics and Performance Grades of Accelerometers

The performance of an accelerometer is specified by a variety of parameters. Since micromachined accelerometers are employed in a broad range of applications, their performance requirements are dependent on the application. The complete definitions and standards for evaluating accelerometer performance may be found in [6] some of which are simply given below:

Bias: It can be defined as the offset of an accelerometer's output signal from the actual value. It can be expressed in the unit of "μg" or "mg".

Short-term stability of bias: It is defined as the standard deviation of bias from its mean value over a period time in the range of second, minute hour or day under constant conditions. It can be expressed in the unit of "μg" or "mg".

Long-term stability of bias: It is defined as the standard deviation of bias from its mean value over a period time in the range of hour, day or year under constant conditions. It can be expressed in the unit of "μg" or "mg".

Bias repeatability: It is the standard deviation of bias from the mean of a certain number of successive measurements taken under constant conditions. It can be expressed in the unit of "μg" or "mg".

Bias instability: It indicates the random fluctuation in bias as estimated across given limited sample time and averaging time intervals. It is represented in the unit of μg. It is measured using Allan variance method.

Temperature sensitivity of bias: It specifies the sensitivity of the bias to the temperature variation. It can be expressed in the unit of "μg/°C" or "mg/°C".

Scale factor: It is the measure of the accelerometer output variation to the corresponding input acceleration. It is generally obtained vias a tumble test. It can be expressed in the unit of "LSB/g", "mV/g", or "Hz/g".

Scale factor error: It is the deviation of the scale factor for its calibrated value. It can be expressed in the unit of "%" or "ppm".

Scale factor short-term stability: It is the standard deviation of the scale factor from its mean value over a period of time [second, minute, hour or day] of continuous operation under constant conditions.

Scale factor long-term stability: It is the standard deviation of the scale factor from its mean value over a period of time [hour, day, year] of continuous operation under constant conditions.

Scale factor repeatability: It is the standard deviation of the scale factor from the mean of a certain number of measurements taken under constant conditions. It can be expressed in the unit of "%" or "ppm".

Temperature sensitivity of scale factor: It specifies the sensitivity of the scale factor to the temperature variation. It can be expressed in the unit of "ppm/°C".

Velocity random walk (VRW): It is the accumulation of velocity inaccuracy over time owing to white noise in acceleration. It is represented in the unit of "m/sec/√hr" or μg/√Hz.

Measurement Range: It is the highest amount of acceleration that an accelerometer can detect. It is expressed in the unit of "±g".

Vibration Rectification Error (VRE): It is defined as the shift in accelerometer bias due to the applied vibration. It has the unit of "$\mu g/g^2$" or "mg/g^2".

Although all the design specifications mentioned above should be regarded to develop an accelerometer, the priority of these parameters are determined by the application. There is no agreed-upon criteria or standards for high, medium, and low-grade performance for the inertial sensors, thus what one expert thinks high-end can be low-end to another. In general, however, inertial sensors fall into four performance categories described below [7]:

- Automotive/Consumer grade
- Industrial grade
- Tactical grade
- Navigation grade

These performance categories are often determined based on the in-run bias stability. Although several system-derived performance criteria are defined for inertial-grade accelerometers, accelerometer performance may be described in general terms by two factors: bias and scale factor stability. Figure 1.2 show the accelerometer performance grades [7]. As shown in Figure 1.2, there are two major types of accelerometers that comprise the various accelerometer performance categories: mechanical accelerometers and quartz/MEMS accelerometers. Quartz and MEMS accelerometers have in-run bias stability ranging from 1000 μg to 1 μg and cover all four performance categories, whereas mechanical accelerometers can achieve in-run bias stabilities less than 1 g but are typically only used for navigation grade applications due to their large size and high cost. Similarly, Table 1.1 shows the performance goals of an accelerometer for missile guidance and high-performance navigation [7].

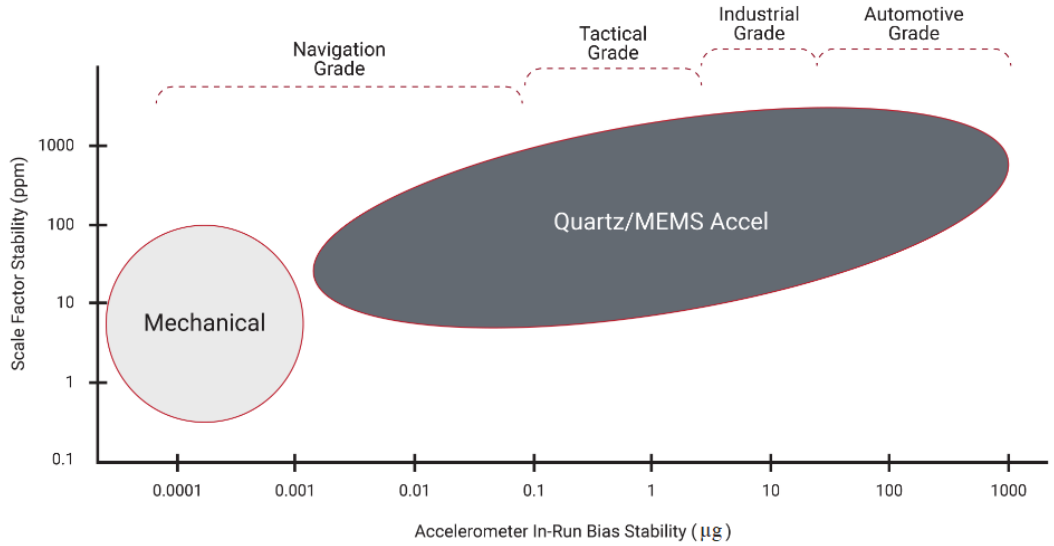


Figure 1.2. Accelerometer performance grades [7].

Table 1.1 Accelerometer specifications for missile guidance and high-performance navigation [8].

Parameter	**Units**	**Missile Guidance**	**High-Performance Navigation**
Bias Long-Term Stability	µg	1-100	1
Bias Short-Term Stability	µg	1-5	0.5
Scale Factor Short-Term Stability	ppm	1-100	10
Scale Factor Long-Term Stability	ppm	1-5	5
Velocity Random Walk	ft/s√h	0.014-0.030	0.0014

1.3 Challenges for Silicon Resonant Accelerometers

There are several design concerns for a silicon resonant accelerometer to achieve the requirements for high-end applications. A large-scale factor is desired for a silicon resonant accelerometer because the acceleration-equivalent noise of the readout circuity decreases with increasing sensor sensitivity. There are two straightforward ways to increase the scale factor: by increasing the proof mass area and by narrowing and extending resonating flexures to increase their force sensitivity. However, these device parameters are usually restricted by the process limits. Adding a microlever mechanism to the structure of a resonant accelerometer is another way to improve its scale factor. Microlevers are utilized to increase the inertial force acting on the resonator beams. A multistage microlever mechanism can be used to increase the scale factor even more, but this method might make the device less stable.

The resolution of the silicon resonant accelerometers is determined by the amplitude noise and phase noise related to the frequency readout circuit. The noise in the amplitude control circuit itself, specifically the flicker noise, should be mitigated. Moreover, a high-gain and low-noise front-end interface circuit is required to achieve good bias stability and a low noise floor. High quality factors in silicon resonators (~100,000) substantially decrease the frequency noise by improving the signal-to-mechanical-noise ratio of the accelerometer and reducing phase jitter. To achieve very high mechanical quality factors in silicon resonant accelerometers, the sensor structure should be in vacuum ambient. In addition to these techniques, increasing the oscillation amplitude improves the resonator's signal-to-noise ratio by decreasing the frequency of the noise. However, there is a trade-off between signal-to-noise ratio and stiffness nonlinearity for oscillation displacement.

Stiffness-related nonlinearity is another important concern affecting the resonators' frequencies [9]. This situation can be described as a spring softening or stiffening as the displacement amplitude of the flexure increases. As a consequence of the stiffness change of the flexure, the resonator frequency decreases or increases. If the springs get stiffer as the amplitude rises, the resonance frequency will increase.

Therefore, the nonlinearity of the flexures' stiffness should be minimized for a stable sensor output.

The temperature stability of MEMS resonant accelerometers is a great concern because the sensitivity of the resonator output to temperature variation destroys the long-term stability of the sensor. A change in the temperature of the accelerometer causes complicated coupled effects in material properties such as the coefficient of thermal expansion (CTE) and elastic modulus, deformation of the structure, and thermo-mechanical stress [10]. Temperature change affects the resonator frequency in two significant ways. Firstly, the elastic modulus of silicon changes with temperature, which directly leads to a drift in the resonator's natural frequency. Secondly, thermal stresses inevitably arise because of the different thermal expansion coefficients (CTE) of the silicon structure and the substrate. The temperature drift of the elastic modulus can be greatly reduced by a differential structure design with two symmetric resonators, in spite of small manufacturing differences between the two oscillators. Thus, the thermal stress on the sensor structure should be minimized the output stability of the silicon oscillating accelerometer.

1.4 Overview of Silicon Resonant Accelerometers

Certain advantages over other types of MEMS accelerometers, such as high sensitivity, wide dynamic range, and direct frequency-to-digital conversion, have pushed the research on silicon resonant accelerometers for high-end applications.

In 1994, AlliedSignal Inc. (which merged with Honeywell in 1999) published their early findings for the development of a silicon vibrating beam accelerometer that was intended to be implemented into a system with a navigational accuracy of one knot [11]. This challenging objective corresponds to an accelerometer with a bias of 50 μg and a long-term scale factor accuracy of 50 ppm. Over a temperature range of -40 °C to 70 °C, the accelerometer demonstrates a bias performance of 318 μg.

In 1996, Honeywell introduced sealed-cavity resonant micromachined accelerometers with a scale factor of 700 Hz/g and resonance frequencies between 500-700 kHz [12]. The device structure was fabricated from thin films of fine-grained polysilicon with vacuum packaging. The temperature decency of the frequency output is about 45 ppm/°C.

In 1997, T. A. Roessig *et al.* showed the feasibility of vibrating beam accelerometers in a surface-micromachining technology using the BiMEMS foundry process. [13]. The sensor has a resonance frequency of 68 kHz. The sensitivity of accelerometer is 45 Hz/g with a microlever structure. However, the spring stiffening was a problem for this sensor structure.

Draper Laboratory was among the first research groups to work on the silicon resonant accelerometers. The results of their work are still at the frontline of research for the silicon vibrating beam accelerometers. [8, 14]. Figure 1.3 depicts the geometry of the silicon resonant accelerometer sensor developed by Draper Laboratory. The sensor structure consists of a pair of double-ended tuning-fork oscillators connected to a single proof mass. It does not employ a microlever structure to amplify the applied force, and the sensors were fabricated on the silicon-on glass with the bulk dissolved-wafer process of Draper Laboratory. In this study, they achieved the bias instability of below 1 μg, the standard deviation in the scale factor of 3 ppm, and the standard deviation in bias of 5 ppm, which is close to the performance required of the strategic missile applications.

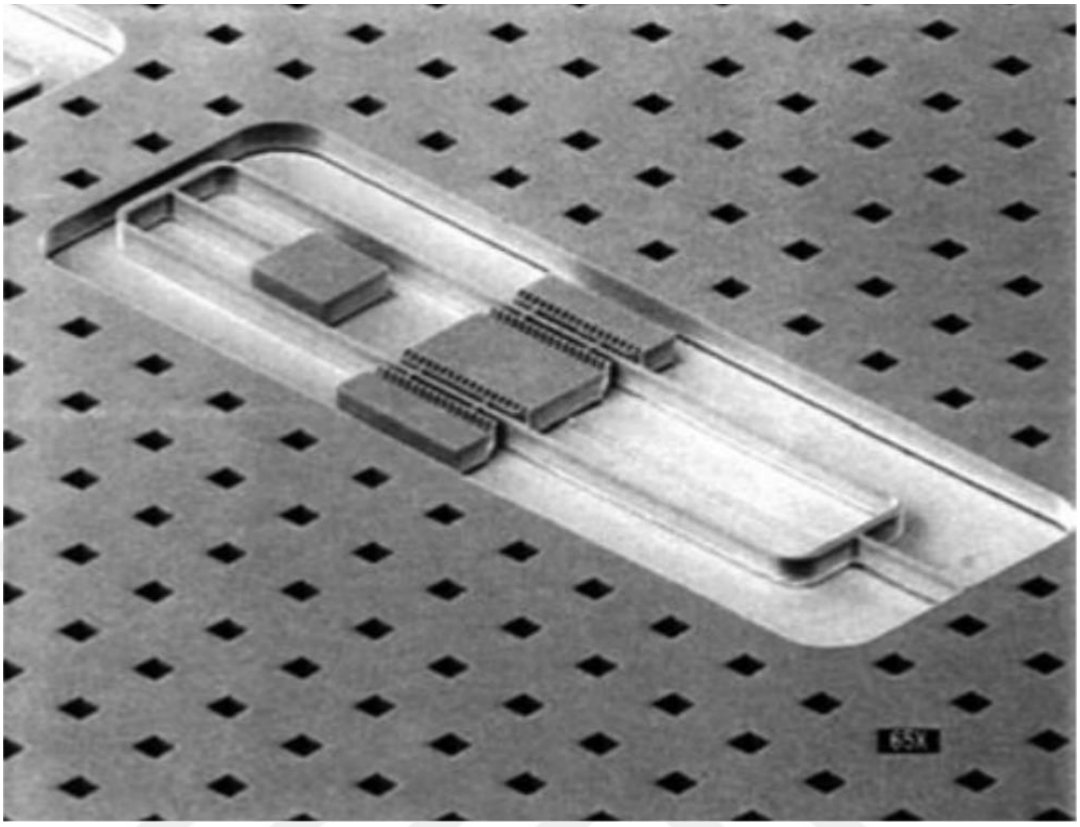


Figure 1.3. The geometry of silicon resonant accelerometer developed by Draper Laboratory [8].

Seoul National University demonstrated a differential resonant accelerometer with lateral drive (DRXL). This structure utilizes the gap-sensitive electrostatic stiffness change effect [15]. Figure 1.4 depicts the SEM picture of the fabricated laterally-driven resonant silicon accelerometer developed by Seoul National University. The electrostatic force reduces the mechanical stiffness of the spring, resulting in a change in output frequency. The resonance accelerometer includes a DETF resonator centered between two identical proof masses. The sensor was fabricated using a pyrex glass substrate, single crystal silicon with 40-um thickness, and a glass cap for wafer-level vacuum packaging. The manufactured accelerometer demonstrates a sensitivity of 64 Hz/g per resonator at a resonance frequency of 24,888 Hz, a bias instability of 5.2 μg and a bandwidth of 110 Hz. The same research group also

presented vertical-type and lateral-type differential resonant accelerometers consisting of one out-of-plane accelerometer and two in-plane accelerometers using the same process with single crystal silicon [16].

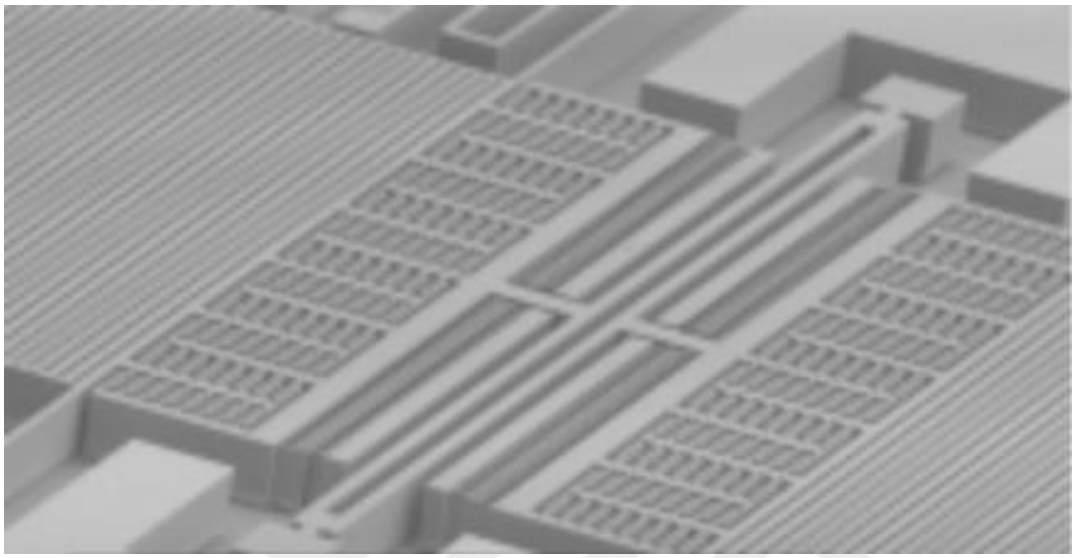


Figure 1.4. The SEM image of the fabricated laterally-driven resonant silicon accelerometer developed by Seoul National University [15].

In 2009, D. Pinto *et al.* showed a compact, sensitive, resonant accelerometer with a surface area of 0.05 mm^2 [17]. The frequency readout circuit is implemented using a phase lock loop (PLL) constructed with a computer-controlled lock-in amplifier (LIA). The observed sensitivity is 22 Hz/g, and the resolution is better than 5 mg. In 2010, C. Comi *et al.* reported an in-plane resonant accelerometer with a sensitivity 455 Hz/g and a resonance frequency of about 58 kHz [18]. The size area of device is 0.25 mm^2 with a thickness of 15 μm. In 2016, the same research group reported another study about a new polysilicon resonant accelerometer for out-of-plane measurements [19].

Stanford University reported the first resonant accelerometer fabricated with the Stanford epitaxial polysilicon encapsulation process in 2013 [20]. They improved their fabrication process in 2016 to allow for narrow and wide lateral transduction

gaps in-plane and out-of-plane electrodes, and to eliminate the need for release etch-holes in the device layer [21]. In 2017, they demonstrated a temperature-compensated resonant accelerometer with a scale factor of 427 Hz/g and a bias instability of 0.16 μg [22]. The device employs a single-point anchor to reduce frequency changes caused by environmental and packaging stress. Figure 1.5 shows the SEM picture of the resonant accelerometer studied in [22]. In [23], they integrated a micro-oven with the resonant accelerometer in [22] to enhance the scale factor and bias stabilities.

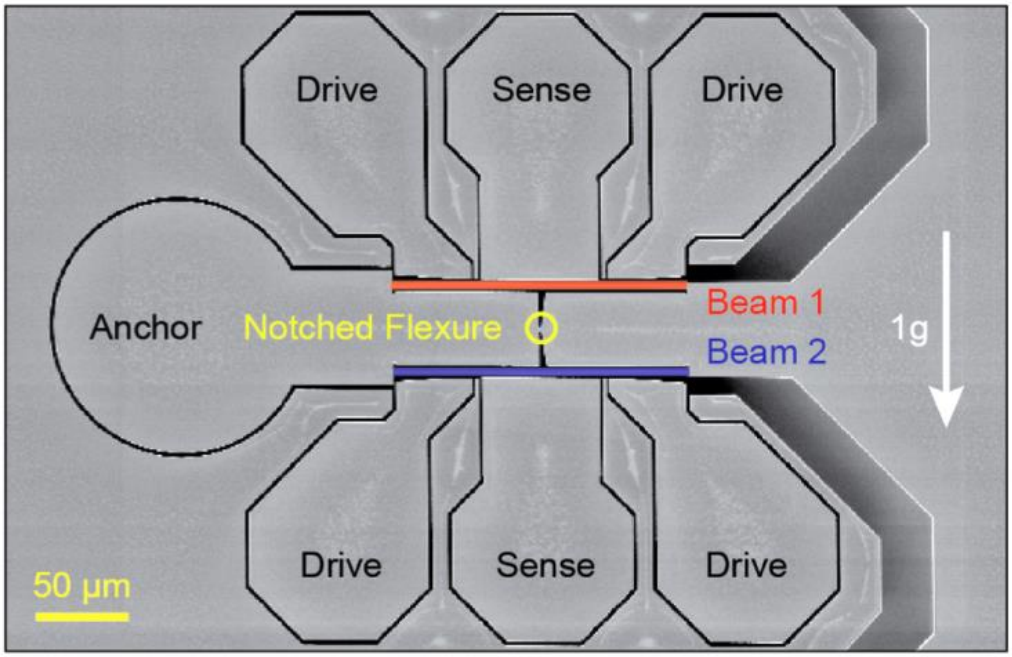


Figure 1.5. The SEM picture of the resonant accelerometer using a single-anchor point developed by Stanford University [22].

The University of California, Berkeley demonstrated a vacuum-packaged surface micromachined resonant accelerometer with a noise floor of 40 μ/√Hz for an input acceleration frequency of 300 Hz in 2002 [4]. As a follow-up to this first study, the University of Cambridge reported a high-resolution MEMS tilt sensor based on the resonant sensing principle with a temperature sensitivity of nearly 0.007 °/K and a

dynamic range of 90 ° [24]. The microfabricated prototype has a bias stability of less than 500 ng for an average time of 0.8 s. In 2019, they presented a high-performance resonant MEMS accelerometer with a bias stability of 56 ng and a noise floor of 98 ng/√Hz for a dynamic range of ±1g [25]. The device comprises of a single force-sensitive resonating beam placed between two proof masses. In the same year, they reported another high-resolution resonant MEMS accelerometer with a bias stability of 17ng and a noise floor of 17.8ng/√Hz for a dynamic range of ±1g [26]. In 2021, the collaboration of the University of Cambridge and Silicon Microgravity Ltd. developed a navigation-grade MEMS resonant accelerometer with a size of 3.5 mm x 3.5 mm, a bias instability of 0.123 μg, a velocity random walk of 0.7μg/√Hz, a scale factor of 1110 Hz/g for a range of ±25g [27]. One drawback of this work is that it is encapsulated at the die level, which could affect the sensor's long-term stability and vacuum level.

Several research institutions in China have also published work on micromechanical silicon resonant accelerometers. Nanjing University of Science and Technology reported a wafer-level vacuum packaged silicon resonant accelerometer with a bias instability of 10 μg, a resolution of 10 μg/√Hz, a scale factor of 120 Hz/g, a resonance frequency of 25 kHz, and a measurement range of ±50g [28]. The same research group presented another silicon vibrating beam accelerometer with a bias instability of 1 μg, a resolution of 13 μg/√Hz, a bias stability of 10 μg (1σ, one hour), a scale factor of 160 Hz/g, a resonance frequency of 22.1 kHz, and a measurement range of ±20g [29]. They also established the nonlinear vibration models of the micro-resonator to optimize the design of silicon resonant accelerometer [30]. The State Key Laboratory of Transducer Technology reported a method to enhance sensitivity of MEMS resonant accelerometer by using electrostatic softening effect [31]. Zhenjiang University developed a biaxial resonant micro accelerometer with a single proof-mass [32]. They also reported a MEMS resonant accelerometer with a method for adjusting sensitivity. [33]. This prototype consists of a proof mass, a pair of fishbone-shaped clamped beams serving as sensing components, a pair of single-stage microlever mechanisms for magnifying the inertial force

Some research groups have focused on the CMOS read-out electronics of silicon resonant accelerometer to improve its performance. National University of Singapore presented a fully differential CMOS readout circuit for silicon resonant accelerometer with a resolution of 20μg /√ Hz and a bias instability of 4μg in 2008 [34]. They presented an ultra-low-noise CMOS read-out circuit for MEMS oscillating accelerometer in 2015. The accelerometer with a fully differential CMOS continuous-time read-out circuit achieves a bias instability of 0.6 μg, a bias stability of 6.3 μg (1σ, one hour), and a noise floor of 2 μg/√Hz with a scale factor of 140 Hz/g for ±20g full range [35]. In 2017, they demonstrated the improved version of the previously reported CMOS read-out circuit [36]. They also constructed a phase noise model for a silicon resonant accelerometer [37]. Nanjing University of Science and Technology developed a silicon resonant accelerometer with an ASIC read-out circuit [38].

Micromachined resonant accelerometers, particularly those manufactured with silicon-on-glass technology, are susceptible to temperature drift due to inherent thermal stress. It is still a great concern because the sensitivity of the resonator output to temperature variation destroys the long-term stability of the sensor. Several methods to reduce the temperature drift of silicon-based resonant accelerometers have been reported in the literature. External temperature sensors or additional resonator have been integrated next to the accelerometer to sense temperature and calibrate the sensor output [39, 40, 41, 42]. However, this method is often inadequate for determining the real local temperature because of the distance between the position of the accelerometer and temperature sensor. Self-compensation techniques are also implemented without using additional temperature sensors to minimize the temperature drifts [43, 44]. These techniques enhance the temperature sensitivity of the resonant accelerometers up to a certain point, but they are not adequate to obtain a navigation-grade accelerometer. Using a micro-oven or micro-cooler within the sensor structure for active temperature correction is another technique to mitigate the temperature drift of a resonant accelerometer [23]. Although this method is effective

for temperature compensation, the operating temperature range of a micro-oven is limited by its size and power consumption.

Some research groups focused on the optimization of the sensor structure to minimize the temperature drift of resonant accelerometers. J. Cui *et al.* reported a silicon resonant accelerometer with a stress isolation frame and axis-symmetric anchoring to enhance temperature performance. [45]. Figure 1.6 shows the SEM picture of the fabricated SRA. The accelerometer demonstrates a scale factor of 516 Hz/g for a resonance frequency of 138.4 kHz, nearly matched temperature coefficients of frequency of 5.72 Hz/°C and 5.92 Hz/ °C, and a bias thermal sensitivity of 0.42 mg/°C for the differential reading over the temperature range from -40 °C to 40 °C.

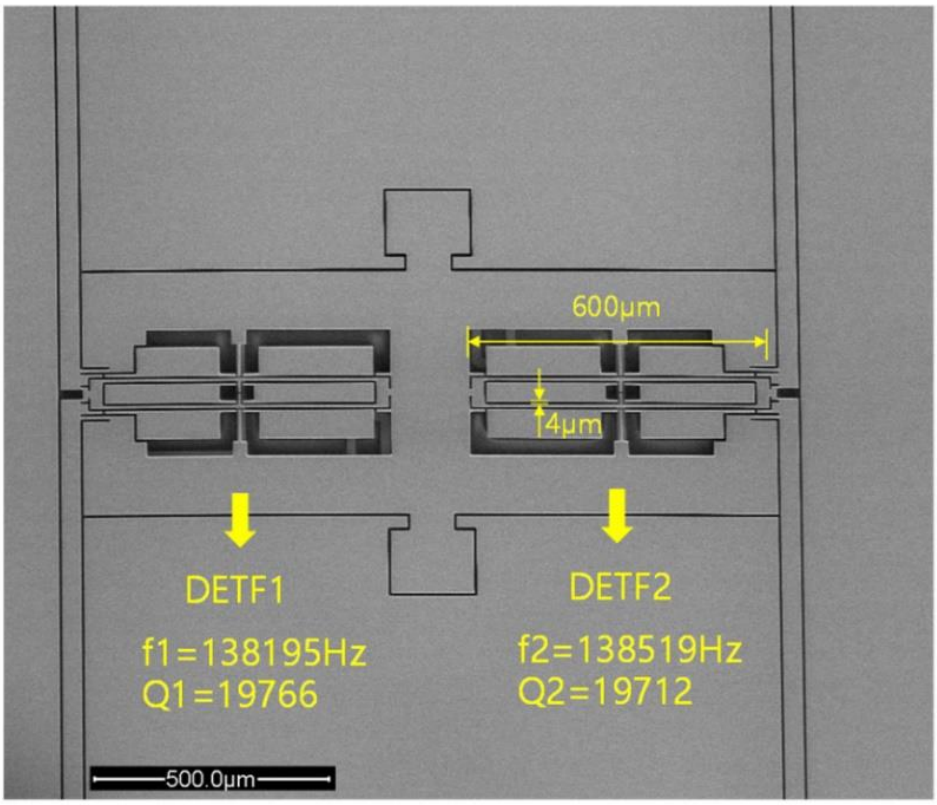


Figure 1.6. The SEM picture of the silicon resonant accelerometer with a stress isolation frame [45].

Stanford University presented a differential resonant accelerometer with a single-point anchor [23]. This design may significantly reduce frequency variations caused by package stress. Still, the structure might be weak and have a large cross-axis coupling error because a small anchor was used to hold up the proof mass.

Tsinghua University reported two different sensor structures with a reduced thermal stress sensitivity either utilizing optimized anchor locations [46] or a single anchor isolation frame [47,48]. Figure 1.7 shows the schematic of the structure with single-anchored isolation frame. The die size is 8.7 mm x 8.7 mm x 0.58 mm, which means the device has a quite large proof mass for a large-scale factor. The accelerometer fabricated on a single-anchored isolation frame shows a bias temperature drift coefficient of 4.4 μg/°C for differential reading (0.55 Hz/°C for single resonator) over the temperature range from 20 °C to 60 °C.

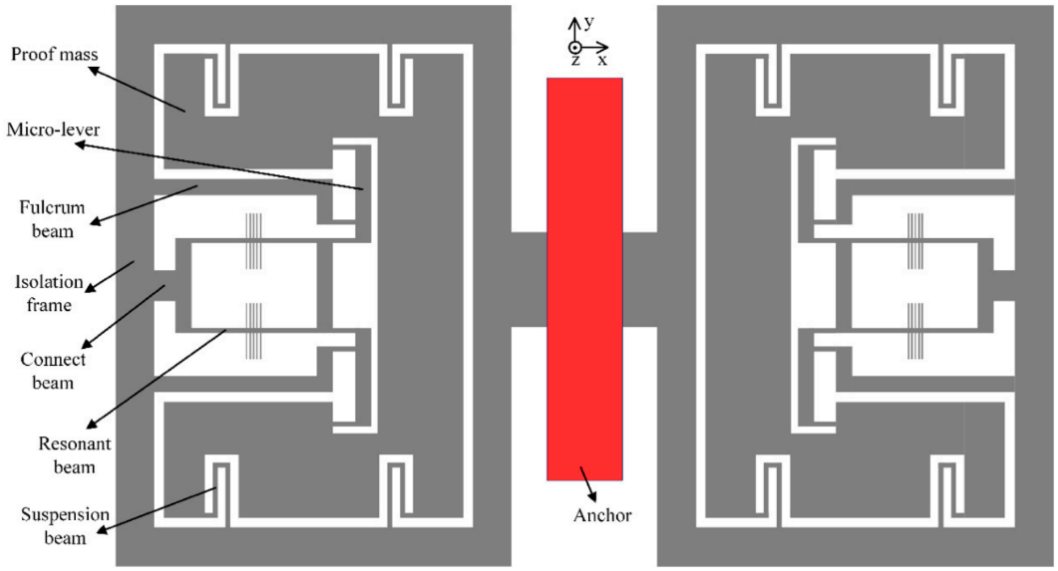


Figure 1.7. The silicon resonant accelerometer structure mounted on single anchored isolation frame [48].

In conclusion, many research institutions and companies have already reported different studies for a silicon resonant accelerometer aimed at high-end applications. Although silicon-based resonant accelerometers have a high potential to replace quartz accelerometers in navigation-grade applications, bias temperature drift remains the most significant source of error, limiting long-term stability.

1.5 Silicon Resonant Accelerometers Developed in This Thesis Study

In the scope of this thesis, three different silicon resonant accelerometer structures are sequentially designed, fabricated, characterized, and tested with the frequency readout circuit. The same DETF resonator design is used as the sensing element in all sensor designs. Moreover, the stationary parts of the DETF resonators are connected to the stationary anchors using specially designed stress release structures to mitigate the thermal stress effect. Figure 1.8 shows the simplified structure of the first design, namely “SRA Design-1”, consisting of a large proof mass and two DETF resonators. This design does not employ a microlever structure. The proof mass is connected to the stationary outer frame.

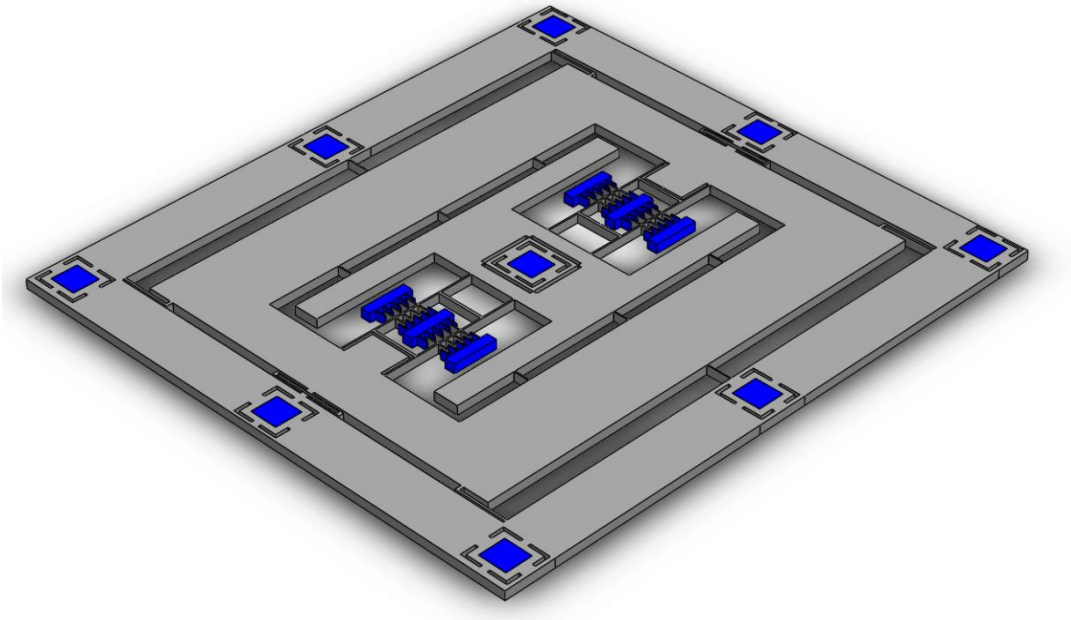


Figure 1.8. Simplified structural view of the “SRA Design-1” accelerometer.

Figure 1.9 depicts the simplified structure of the second design, namely “SRA Design-2”, consisting of a large proof mass, two DETF resonators and four microlevers. The second sensor structure utilizes microlevers to magnify the inertial force acting on the DETF resonators in addition to the sensor frame of the first sensor structure.

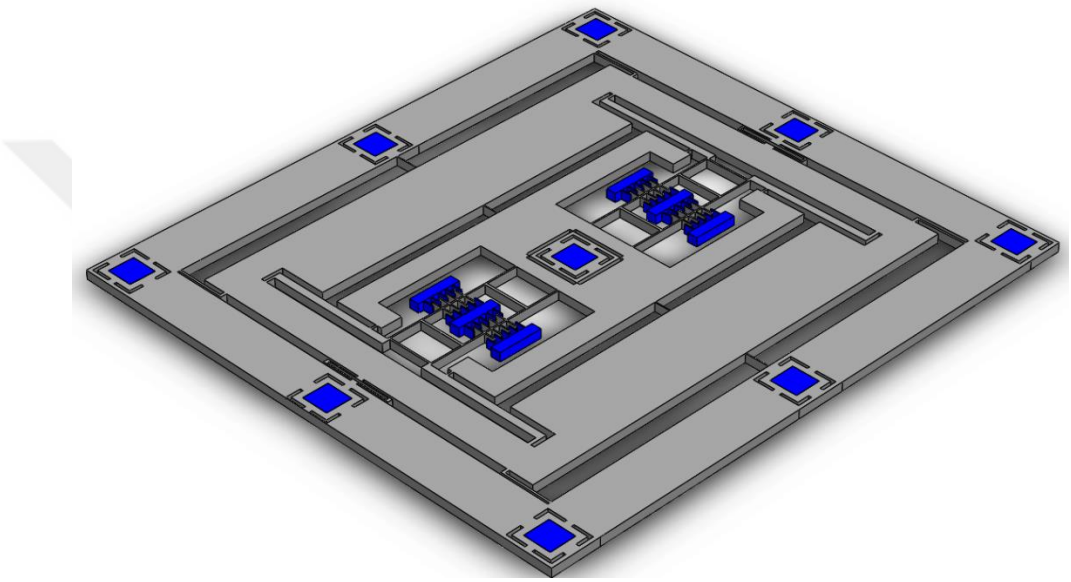


Figure 1.9. Simplified structural view of the “SRA Design-2” accelerometer.

The stress-related problems of the first and second sensor designs after fabrication leads to a silicon resonant accelerometer structure mounted on a single anchor, namely the third silicon resonant accelerometer design (SRA Design-3). Figure 1.10 demonstrates the simplified structure of the third design consisting of a large proof mass, two DETF resonators and four microlevers. As opposed to “SRA-Design-2”, the proof mass is connected to a single anchor located in the center of the sensor structure to minimize the thermal stress on the DETF resonators.

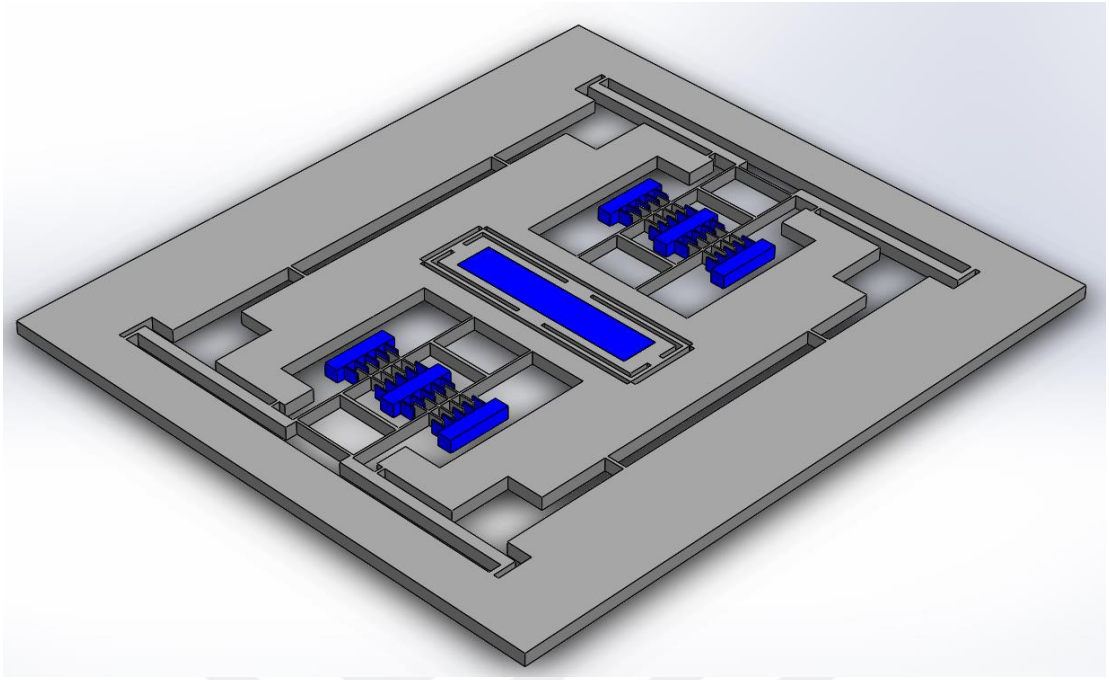


Figure 1.10. Simplified structural view of the “SRA Design-3” accelerometer.

1.6 Research Objectives and Thesis Outline

The capacitive MEMS accelerometers developed at METU have reached performance values below 20 μg/Hz of velocity random walk [49,50]. However, these sensors have suffered from the long-term drift of bias, which restrains their utilization in long-term flight control and navigation. The temperature drift characterization and day-to-day repeatability of an accelerometer are very important for the short-term and long-term accuracy of many military systems requiring high performance. The main goal of this study is to develop a silicon resonant accelerometer with low bias drift and a comparable noise level to its capacitive counterparts to replace them in tactical and navigation-grade applications. The following are the particular goals of this research:

1. Design and analysis of the silicon resonant accelerometer structures. The mechanical model of the silicon resonant accelerometer should be analyzed.

The resonant accelerometer design should have a high acceleration sensitivity and a low temperature sensitivity. The thermal stress on the sensor structure should be minimized. Integration of microlevers into the mechanical structure is needed to increase force sensitivity. The secondary effects such as stiffness nonlinearity should be considered.

2. Fabrication of the designed silicon resonant accelerometer with a vacuum packaging process based on silicon-on-glass process (SOG). The silicon resonant accelerometers should be operated in vacuum to minimize the phase noise, so the sensors should be wafer-level hermetically encapsulated in the vacuum environment. The problems related to sensor fabrication process should be analyzed and solved.
3. Design and implementation of the frequency read-out circuit for the silicon resonant accelerometers. The DETF resonators of the silicon resonant accelerometers should be oscillated at a constant amplitude by a control circuit. The front-end electronics and gain stage of the systems should be carefully designed to maximize the signal-to-noise ratio of the sensor output. The controller values for the PLL and PID system of the frequency read-out circuit should be optimized.
4. Characterization and tests of the silicon resonant accelerometers integrated to the frequency read-out electronics. The resonance characteristics of the fabricated sensor chips integrated with the front-end electronics should be obtained. The acceleration sensitivity, bias stability, noise level, and temperature sensitivity of the silicon resonant accelerometer should be tested. It should be verified that the sensor has a low bias drift and low temperature sensitivity.

The structure of thesis and the contests of the subsequent chapters are given below:

Chapter 2 discusses the theory of the silicon resonant accelerometer and provides the analytical model of the accelerometer developed in this work. Firstly, the basic operating principle of the silicon resonant accelerometer is described, followed by the derivation of analytical solutions for the force sensitivity of the DETF resonator.

The microlever mechanism is then described, and the microlever amplification factor and system amplification factor are determined. Next, the sensor structures studied in this work are demonstrated. Finally, the finite element simulations performed during the design, including modal analysis, force simulations, and temperature simulations for predicting the performance of the silicon resonant accelerometer prior to fabrication, are presented.

Chapter 3 provides information on the fabrication process for the silicon resonant accelerometers. The SOG process and wafer-level vacuum packing process for sensor fabrication are explained. Then, the results of the fabrication are given.

Chapter 4 explains the details of the control electronics for the silicon resonant accelerometers. The analog front-end electronics is introduced. Then, the operation and design of the phase-locked loop are mentioned. Next, the automatic gain control loop is explained.

Chapter 5 presents the test results of the silicon resonant accelerometers. Firstly, the resonance characterization results of the studied sensors are given. Then, the 4-point tumble test results for scale factor measurements of the resonant accelerometers are demonstrated. Next, the temperature test results of the corresponding accelerometers are provided. Finally, the Allan variance test results of the accelerometers are presented.

Chapter 6 concludes with a summary and presentation of the findings of the study. In addition, it proposes a potential future study direction for related topic.

CHAPTER 2

MECHANICAL DESIGN OF SILICON RESONANT ACCELEROMETER

This chapter discusses the theory of the silicon resonant accelerometer and provides the analytical model of the accelerometer developed in this work. Section 2.1 gives information about the mechanical model of the silicon resonant accelerometer. In this section, firstly, the basic operating principle of the silicon resonant accelerometer is described, followed by the derivation of analytical solutions for the force sensitivity of the DETF resonator. The microlever mechanism is then described, and the microlever amplification factor and system amplification factor are determined. Next, the temperature sensitivity and stiffness nonlinearity of the DETF resonator are examined. After that, the mechanisms of capacitive sensing and actuation are explained. Section 2.2 describes the sensor structures studied in this work. Section 2.3 presents the finite element simulations performed during the design, including modal analysis, force simulations, and temperature simulations for predicting the performance of the silicon resonant accelerometer before sensor fabrication. Section 2.4 summarizes this chapter.

2.1 Mechanical Model of Silicon Resonant Accelerometer

The working principle of silicon resonant accelerometer is based on the force sensing. The sensor output is a frequency proportional to the input acceleration. Figure 2.1 shows the structure of silicon resonant accelerometer including microlevers. Silicon resonant accelerometer is comprised of three major parts: a proof mass, two DETF resonators and four microlevers. Two identical DETF resonators are coupled to a large proof mass via microlevers such that the proof mass

axially loads to the resonator pairs. The inertial force is amplified using a single-stage microlever mechanism. Under the applied load, the accelerating proof mass loads one resonator in tension while loading the other one in compression. As a result, the tension loading increases the natural frequency of one resonator, and the compression loading decreased the natural frequency of the other resonator. The frequency difference of two resonators is a measure of the acceleration along the input axis of SRA. A differential configuration doubles the mechanical sensitivity to the acceleration and suppresses common-mode error such as temperature, nonlinearity and off-axis acceleration.

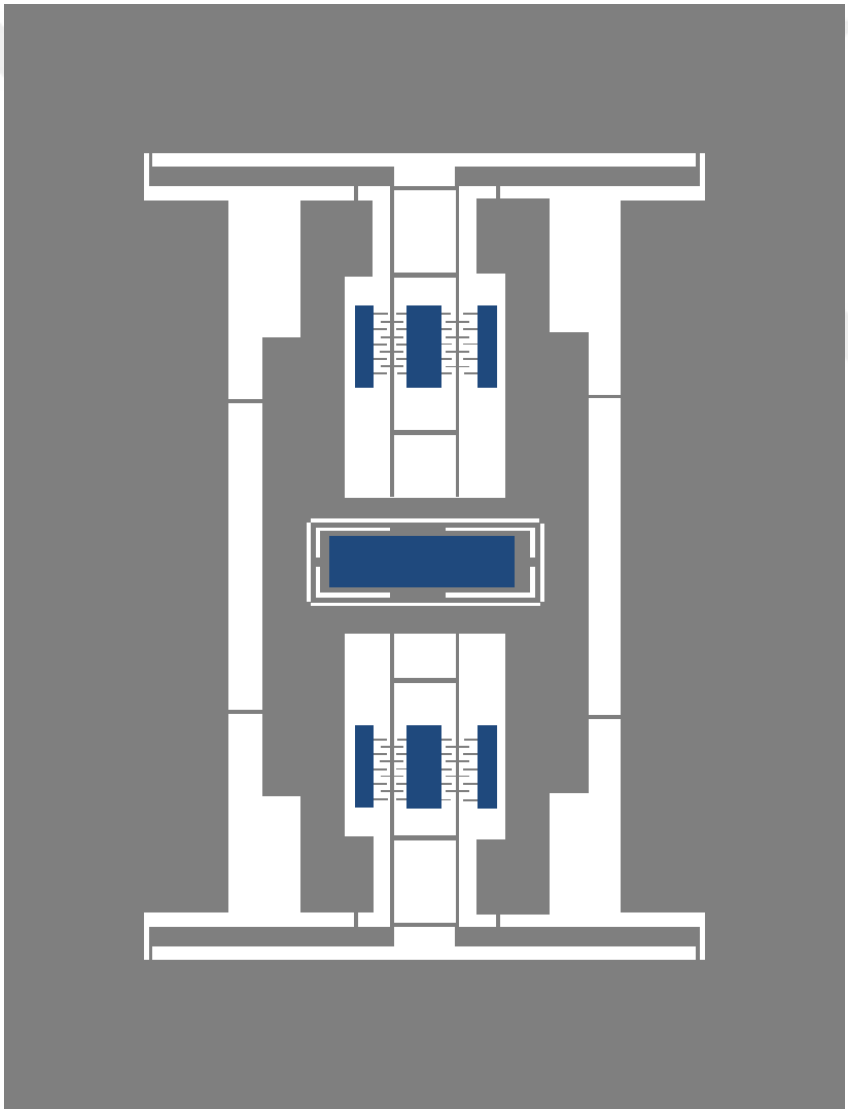


Figure 2.1. The structure of the silicon resonant accelerometer utilizing micro levers.

The movable proof mass is suspended to the stationary anchors with beams. The beams are flexible in the direction of the input axis, but they are rigid along the other axes so that the proof mass is free to move only along the input axis.

The DETF resonators are the core component of the silicon resonant accelerometer. Each DETF resonator is kept vibrating at its out-of-phase mode natural frequency by electrostatic actuation and capacitive sensing mechanism in a self-oscillation loop. The out of phase oscillations of the DETF flexures cancels away the reaction forces created by the motion of each individual mass.

The acceleration sensitivity of the silicon resonant accelerometer is determined by the force sensitivity of DETF resonator, the amplification factor of microlever structure, and the proof mass.

2.1.1 Force Sensitivity of DETF Resonator

This section presents the analytical analysis and critical design parameters of the DETF resonator for a regular operation of the silicon resonant accelerometer. Figure 2.2 shows the simplified model of the double-ended tuning-fork resonator consisting of two flexure beams. Referring to Figure 2.2, the stiffness of the axially loaded with a fixed-end one flexure beam can be approximated as [51]

$$k_{flexure} = \frac{16EHW^3}{L^3} \pm \frac{2.4F_{flexure}}{L} \tag{2.1}$$

where E is the young's modulus of silicon<111>, L is the length of the flexure, W is the width of the flexure, H is the height of the flexure, $F_{flexure}$ is the axial force acting on the nonfixed end of single flexure. A DETF resonator is consisting of two flexure beams connected parallel so the resonance frequency of one DETF resonator can be written as

$$w_{DETF} = \sqrt{\frac{2k_{flexure}}{2m}} \tag{2.2}$$

where m is the mass of one flexure. Substituting Equation 2.1 into Equation 2.2, the resonance frequency of the DETF resonator can written in terms of the device parameters as

$$w_{DETF} = \sqrt{\frac{16EHW^3}{mL^3} \pm \frac{4.8}{mL}} \tag{2.3}$$

In Equation 2.3, the first term represents the natural frequency of the DETF resonator, and the second term corresponds to the frequency shift caused by the applied force. The loaded resonance frequency of the DETF resonator may be expressed using the unloaded natural frequency and device parameters by rearranging the terms in Equation 2.3 as follows:

$$w_{DETF} = w_{0,DETF} \sqrt{1 \pm F_{flexure} \frac{0.3L^2}{EHW^3}} \tag{2.4}$$

where $w_{0,\mathrm{DETF}}$ is the unloaded resonance frequency of the DETF resonator. It should be noted that $F_{flexure}$ is the axial force acting on one flexure beam, which is the half of the force acting on one DETF resonator and the quarter of the total force acting on the inertial mass multiplied by the effective amplification factor of microlevers. Equation 2.4 implies that the frequency shift of the DETF resonator is proportional to the axial force acting on the beams and the length of the flexure, but it is inversely proportional to the width of the flexure. The height of the flexure does not change the ratio of the scale factor to the nominal resonance frequency of the resonator. The axial force acting on the flexure is dependent on the inertial mass and the effective amplification factor of the microlevers.

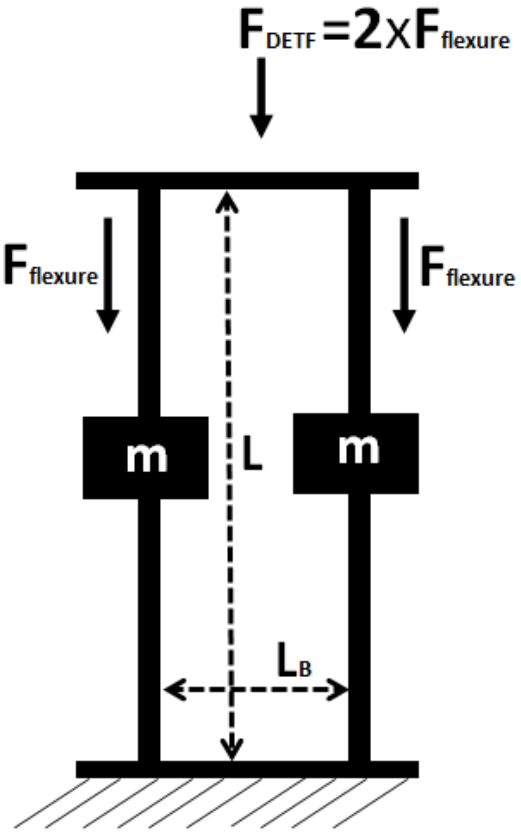


Figure 2.2. Simple model of DETF resonator consisting of two flexure beams.

The DETF resonator is operated in the out-of-phase mode to improve the quality factor and drive efficiency [52]. A separation of at least 10% between the drive mode (out-of-phase mode) and the parasitic hula mode (in-phase mode) is required to guarantee that the hula mode doesn't interact with the oscillator drive loop. The separation between the drive mode and hula mode of the DETF resonator is determined by the dimension of the base beam connecting two flexures. The detailed mathematical analysis for the separation of the in-phase and out-of-phase modes of the DETF resonator can be found in [51]. The frequencies of these modes are optimized by the modal analysis in FEM simulations for this study.

2.1.2 Microlever Mechanism and System Amplification Factor

A single-stage lever system is employed to increase mechanical sensitivity by enhancing the axial force applied to the two DETF resonators in the silicon resonant accelerometer structure. In general, a microlever structure includes four major parts: a lever arm, a pivot, an input system, and an output system. Figure 2.3 depicts the schematic of the single-stage microlever structure. The pivot and connections are flexible whereas the lever arm is rigid. In Figure 2.3, the input system refers to the axial force acting on the inertial mass and the output system is connected to the nonstationary end of the DETF resonator.

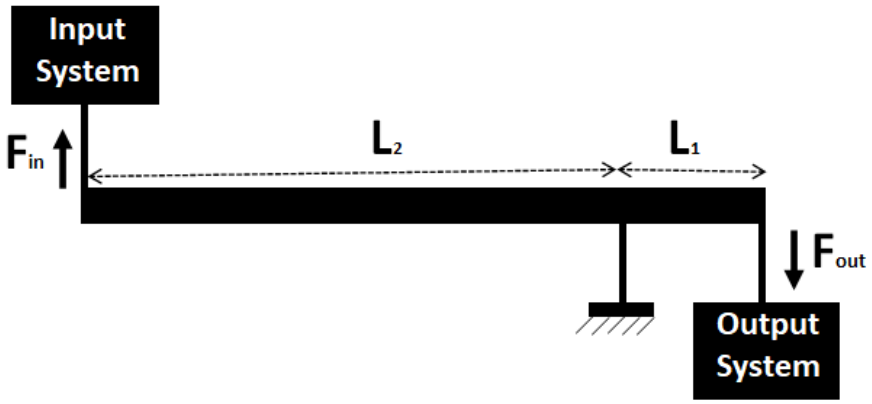


Figure 2.3. Simple model of microlever structure.

The amplification factor of the microlever is the ratio of the output to input force, and it is expressed as [53],

$$A = \frac{\frac{1}{k_o}\left(f_o k_{ro} + f_o k_{rp}\right) + L_1 L_2}{\left(\frac{1}{k_o} + k_p\right)\left(f_o k_{ro} + f_p k_{rp}\right) + L_1^2} \qquad 2.5$$

where L_1 is the length between pivot beam and output beam, L_2 is the length between pivot beam and input beam, k_o is the axial spring constant of the output system, k_{ro} the rotational spring constant of the output beam, k_p is the axial spring constants of

pivot beam, k_{rp} is the rotational spring constant of the pivot beam, f_o and f_p are the functions of the output and pivot beam parameters. The spring constants and other parameters except the axial spring constant of the output system in Equation 2.5 can be calculated using the flowing equations:

$$f_o = 1 + \frac{3(l_o - l_p)l_0^2 w_p^3}{l_0^3 w_p^3 + l_p^3 w_0^3} \quad 2.6$$

$$f_p = 1 + \frac{3(l_p - l_o)l_p^2 w_o^3}{l_0^3 w_p^3 + l_p^3 w_0^3} \quad 2.7$$

$$k_p = \frac{E w_p t_p}{l_p} \quad 2.8$$

$$k_{rp} = \frac{E t_p w_p^3}{12 l_p} \quad 2.9$$

$$k_{ro} = \frac{E t_o w_o^3}{12 l_o} \quad 2.10$$

where E is the Young's modulus of the microlever material, t_p is the thickness of the pivot beam, w_p is the width of the pivot beam, l_p is the length of the pivot beam, t_o is the thickness of the output beam, w_o is the width of the output beam, l_o is the length of the output beam. For maximizing the amplification factor of a single-stage microlever, the axial spring constants (k_p and k_{po}) should be as large as possible, and the rotational spring constants (k_{ro} and k_{rp}) should be as small as possible. For an ideal lever, the axial spring constant of pivot beam is infinite ($k_p \approx \infty$), and the rotational spring constants of pivot and output beams are zero

($k_{ro} \approx 0, k_{rp} \approx 0$). Thus, the amplification factor given in Equation 2.5 is reduced to the following form for an ideal lever:

$$A_{ideal} = \frac{L_2}{L_1} \tag{2.11}$$

The axial spring constant of the output system is calculated by modelling the axial spring constants of the DETF resonator. Figure 2.4 depicts the axial spring model of the DETF with the lever structures to visualize the spring model of the output system. Since the symmetrical design of DETF resonators in the upper and lower parts of the sensor structure, the axial spring constant of the output system, k_o, is the half of the axial spring constant of the overall system, $k_{o,all}$, so it can be expressed as follows:

$$k_{o,all} = 2k_o = \frac{k_1 k_2 k_3}{k_1 k_2 + k_2 k_3 + k_1 k_3} \tag{2.12}$$

where k_1 is the axial spring constant of the connection beam between the lever arm and tuning fork, k_2 is the axial spring constant of one flexure in DETF resonator, k_3 is the axial spring constant of the connection beam between the tuning fork and stationary anchor.

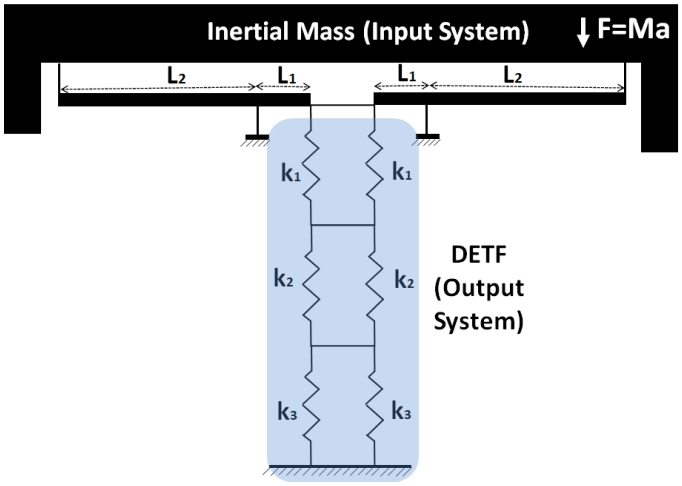


Figure 2.4. The axial spring model of the DETF resonator integrated to the lever structure.

When an acceleration is applied to the silicon resonant accelerometer along the input axis, the force from the proof mass is amplified by the microlever and then transferred to the DETF resonators. The effective amplification factor is the ratio between the axial force of the DETF beam and the input inertial force of the proof mass [54]. Thus, the effective amplification factor of overall system can be written as follows:

$$A_{eff} = A\frac{K_{in}}{K_{in} + K_m} \tag{2.13}$$

where K_m is the bending stiffness of the input axis and K_{in} is the equal axial stiffness seen by the input system, i.e., the equal axial stiffness from the input beam of the microlever to the stationary end of the DETF resonator. The equal axial stiffness seen by the input system can be approximated as:

$$K_{in} = \frac{k_{o,all}k_pL_1^2}{k_{o,all}(L_2 - L_1)^2 + k_pL_2^2} \tag{2.14}$$

2.1.3 Scale Factor of Overall System

When an input acceleration is applied to the proof mass of silicon resonant accelerometer, one DETF resonator is loaded in tension and the other is loaded in compression. The axial force acting on one flexure beam, $F_{flexure}$ is the quarter of the multiplication of the total force acting on the inertial mass by the effective amplification factor of microlevers:

$$F_{flexure} = \frac{A_{eff}Ma}{4} \tag{2.15}$$

where M is the mass of the poof mass of the silicon resonant accelerometer and a is the input acceleration acting along the sensitive axis of the sensor. Substituting Equation 2.15 into Equation 2.4 and taking the frequency difference of the two DETF resonators, the acceleration sensitivity of the overall system can be expressed as:

$$\Delta w = w_{0,DETF}\left(\sqrt{1+\frac{A_{eff}Ma}{4}\frac{0.3L^2}{EHW^3}}-\sqrt{1-\frac{A_{eff}Ma}{4}\frac{0.3L^2}{EHW^3}}\right) \quad 2.16$$

$$\Delta f = f_{0,DETF}\left(\sqrt{1+\frac{A_{eff}Ma}{4}\frac{0.3L^2}{EHW^3}}-\sqrt{1-\frac{A_{eff}Ma}{4}\frac{0.3L^2}{EHW^3}}\right) \quad 2.17$$

Using the Taylor series and neglecting the higher order terms, Equation 2.17 can be rearranged as:

$$\Delta f = f_{0,DETF}\left(\frac{A_{eff}Ma}{4}\frac{0.3L^2}{EHW^3}\right)+\frac{1}{8}f_{0,DETF}\left(\frac{A_{eff}Ma}{4}\frac{0.3L^2}{EHW^3}\right)^3 \quad 2.18$$

In Equations 2.17 and 2.18, the effective amplification factor, A_{eff}, is calculated using the Equations 2.13 and 2.14.

It should be noted that there is a nonlinear relation between the single resonator frequency and input acceleration. Figure 2.5 shows the nonlinear relation between the frequency output and input acceleration. Although the differential configuration suppresses this nonlinearity, it does not completely eliminate. Thus, the measurement or operation range of the silicon resonant accelerometer is limited by the acceptable linear region of the frequency output and input acceleration relation.

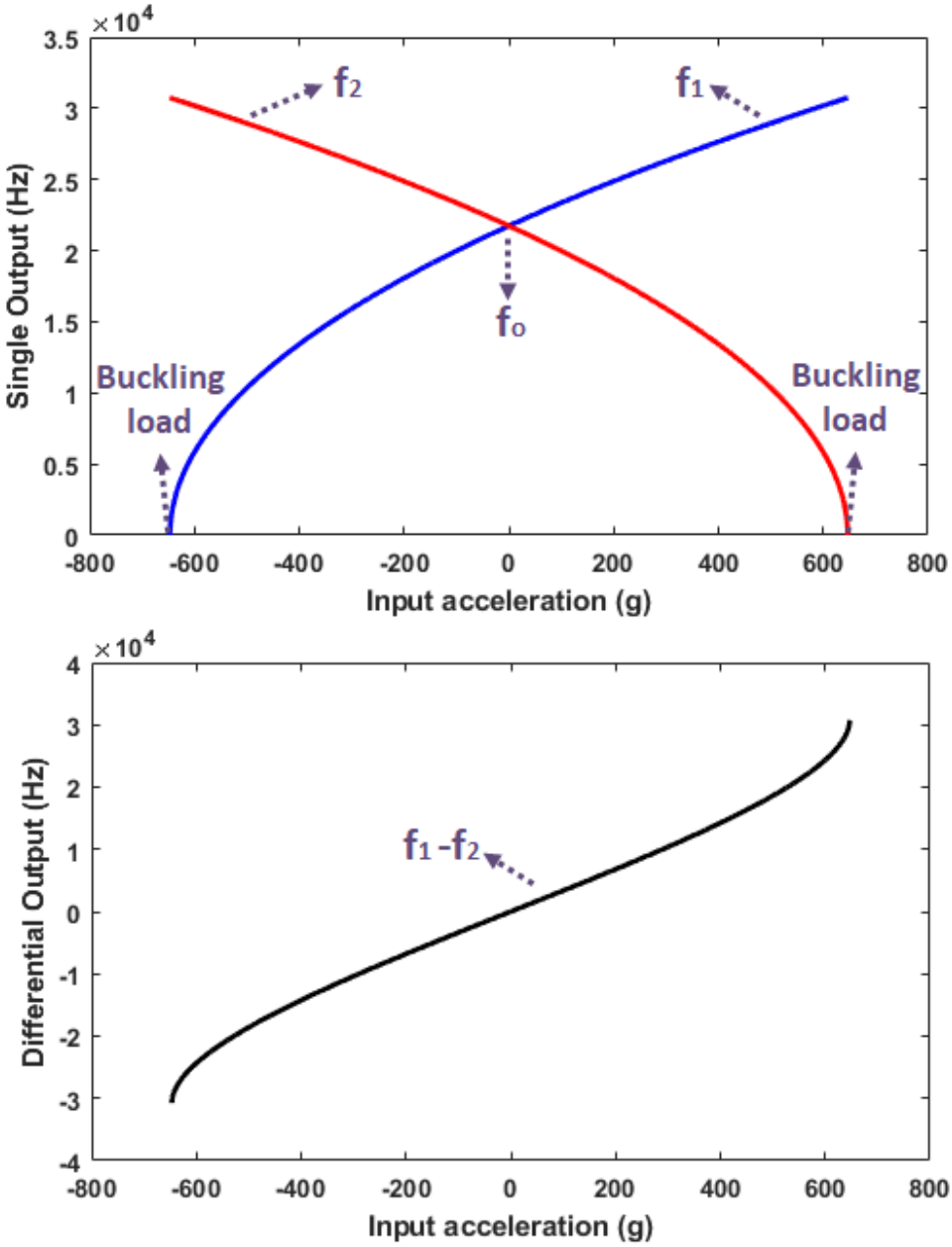


Figure 2.5. The relation between the resonator frequency and input acceleration.

2.1.4 Stiffness Nonlinearity

Stiffness nonlinearity is one of the important properties of the DETF flexures affecting the resonators' frequencies. This situation can be described as a spring stiffening with the displacement amplitude because of the nonlinear restoring force

in the flexures. As the oscillation amplitude rises in the flexure, the stiffness of the beam increases so the resonator frequency increases. The spring forces resulting from the transverse motion of a flexure can be represented by

$$F = k_1 y + k_2 y^2 + k_3 y^3 \tag{2.19}$$

where y represents the transverse motion of the flexure. Then, the undamped motion for the DETF resonator is given as:

$$m\ddot{x} = k_1 y + k_2 y^2 + k_3 y^3 \tag{2.20}$$

where m is the mass of the flexure. For a sinusoidal motion of the flexure, the transverse motion of flexure can be written as

$$y(t) = Ysin(wt) \tag{2.21}$$

By substituting Equation 2.21 into Equation 2.20 and rearranging the terms, the following equation can be obtained:

$$\left(\frac{k_1}{m} - w^2\right) Ysin(wt) + \frac{k_2}{2m} Y^2 (1 - cos(2wt)) + \frac{k_3}{m} Y^3 \left(\frac{3}{4} sin(wt) - \frac{3}{4} sin(3wt)\right) = 0 \tag{2.22}$$

In the resonance condition, the DETF resonator behaves like a sharp bandpass filter in the vacuum environment; therefore, the higher frequency terms and DC term can be omitted in Equation 2.22,

$$\left(\frac{k_1}{m} - w^2 + \frac{3}{4}\frac{k_3}{m} Y^2\right) Ysin(wt) = 0 \tag{2.23}$$

Solving Equation 2.23 for w, the resonance frequency can be approximated as the function of the displacement amplitude as follows [55]:

$$w = w_0\left(1 + \frac{3}{8}\frac{k_3}{k}Y^2\right) \tag{2.24}$$

where w is the frequency at the oscillation amplitude Y, k is the linear stiffness of resonator, k_3 is the cubic stiffness coefficient of resonator, and w_0 is the unloaded resonant frequency.

In order to improve the frequency stability of the silicon resonant accelerometer, the nonlinear stiffness of the flexures should be minimized. There is a trade-off between the signal-to-noise ratio of the sensor output signal and nonlinear stiffness of the flexure. As the oscillation amplitude becomes smaller, the spring stiffness also becomes smaller, so the bias stability would be lower; however, this would decrease the mechanical gain of the sensor. In this study, the oscillation amplitude of the DETF resonators have been determined by considering these concerns. The cubic stiffness coefficient of resonator also should be minimized to mitigate the nonlinear stiffness of the flexure. Calculation of the cubic stiffness coefficient, k_3 term is not straightforward but, the analysis and simulations in [54] can give an insight about the dominant device parameters affecting it. To sum up, the ratio of the cubic stiffness coefficient to the effective stiffness of the DETF resonator is proportional to the beam length and inversely proportional to the beam width.

2.1.5 Temperature Sensitivity and Thermal Stress

Bias drift caused by thermal stress is the most important error source for silicon resonant accelerometers. Temperature changes affect the frequency output of the silicon resonant accelerometer in two ways. First, the Young's modulus of silicon changes with temperature, which directly leads to a drift in the resonator's natural

frequency. Second, thermal stresses inevitably arise because of difference in the thermal expansion coefficients (CTE) of the silicon structure and the glass substrate.

The resonant frequency of the DETF resonator is a function of the Young's modulus of silicon, as expressed in Equation 2.3. Silicon's Young's modulus goes down as the temperature goes up, so the resonator's frequency decreases. Since a silicon resonant accelerometer is made up of two DETF resonators that respond the same way to a change in Young's modulus caused by a change in temperature, this effect is greatly reduced by a differential reading scheme. Although a small manufacturing differences between the two resonators causes a small temperature sensitivity at the sensor output because of the Young's modulus change, this sensitivity is measurable and repeatable so it can be calibrated in the worst case. However, the same solution is not applicable for the thermal stress.

Thermal stress is caused by the thermal expansion coefficient difference of the silicon structure and the borofloat glass substrate. The silicon device wafer is anodically bonded to the glass substrate at the temperature above 360°C, then, the bonded wafer stack cools down to the room temperature. The linear thermal expansion coefficient of the borofloat glass is about 3.25×10^{-6} C^{-1} while the linear thermal expansion coefficient of the silicon is temperature dependent, and it changes from 4.5×10^{-6} C^{-1} to 2.57×10^{-6} C^{-1} between 380°C and 20°C [10]. Therefore, there would be an initial stress on the device structure even at the constant temperature after the fabrication unless a precaution is not taken in the mechanical design of the sensor structure. Moreover, temperature changes would add an extra thermal stress on the DETF resonators. It is not possible to measure or calibrate this stress without adding an extra stress sensor on the device. The thermal stress on the DETF resonators results in a drift in the resonator's natural frequency deteriorating the bias stability of the silicon resonant accelerometer.

The most effective way to eliminate thermal stress effects on sensor output is to design the sensor to be insensitive to stress. Mathematical derivations for thermal stress calculations could be done for the DETF design; however, this analysis would

be complicated and it would not give an exact solution. In this study, the device structure has been optimized performing the finite element simulations for the thermal analysis. A special stress release structure has been utilized in the connection the stationary substrate to the device structure to minimize the stress effect. The details of the finite element simulations have been presented in Section 2.3.

2.1.6 Capacitive Actuation and Sensing Mechanism

The flexures of the DETF resonators are excited at the resonance using the varying-overlap area type capacitors. There are two different electrodes for each resonator: One is used to drive the oscillation of the DETF resonator, while the other detects the displacement. Although the varying-gap type capacitor provides higher capacitive sensitivity than the varying-overlap type capacitor, the electrostatic spring effect in the varying-gap type capacitor would pose a problem for the frequency stability of the resonator output. This is why the varying-overlap type capacitors have been chosen for the actuation and sensing of the DETF resonators in this study.

The displacement in a variable-overlap type capacitor occurs in the lateral direction due to a change in the overlap area of the parallel plates. If there is a potential difference between the parallel plates, energy will be stored in the capacitor owing to the accumulation of charge. The stored energy causes an electrostatic attraction between the moving and stationary conductors. The acting force on the parallel plates in this structure may be represented as

$$F = \frac{1}{2} N \varepsilon_0 \frac{H_0}{D_0} V^2 \qquad 2.25$$

where ε_0 represents the permittivity of the free air, N represents the number of the capacitor pairs, V represents the voltage difference between the parallel plates, H_0 and D_0 represent the overlap height and gap spacing of the plates, respectively.

Capacitive sensing mechanism is utilized to transform the sensor's physical displacement into an electrical signal. In the capacitive sensing mechanism, first the mechanical displacement is converted to current by the capacitors, and then the current is delivered to the interface circuit to acquire the displacement's voltage equivalent. The current that flows through a capacitor is described as

$$I_{out} = \frac{dQ}{dt} = \frac{d(C(t)V(t))}{dt} = C\frac{dV(t)}{dt} + V\frac{dC(t)}{dt} \quad 2.26$$

For the actual operation of the resonator, $V(t)$ is a fixed proof mass voltage, V_{PM}, which is the potential difference between the sensing electrodes and the moveable element. On the other hand, the movement of the sensing capacitors causes a time-varying voltage. Since the time-varying voltage is much less than the constant proof mass voltage throughout operation of the device, the formula for the output current may be expressed as

$$I_{out}(t) \cong V_{PM}\frac{dC}{dt} = V_{PM}\frac{\partial C}{\partial X}\frac{\partial X}{\partial t} \quad 2.27$$

The comprehensive analysis for the electrostatic actuation and sensing mechanism for parallel plate capacitors are provided in [56,57].

2.2 Designs of Silicon Resonant Accelerometers for This Thesis Work

This section presents the mechanical structures of the silicon resonant accelerometers studied in this work and briefly explains the differences between these structures. The mathematical equations derived in previous section are the governing equations of the silicon resonant accelerometer, and they are applicable for all designs used in this study. Three different sensor structures have been studied in this work. The same DETF resonator design has been used as the sensing element in all sensor designs. Moreover, the stationary parts of the DETF resonators are connected to the stationary

anchors using specially designed stress released structures to mitigate the thermal stress effect.

The first sensor design, called “SRA Design-1”, consists of a large proof mass and two DETF resonators, and there is no micro lever structure in this design. Figure 2.6 depicts the mechanical structure of the “SRA Design-1”. In this structure, the proof mass is connected to the stationary outer frame. “SRA Design-1” was designed to be less sensitive to acceleration but mechanically more robust. Table 2.1 summarizes the sensor design parameters for “SRA Design-1”.

The second sensor design, called “SRA Design-2”, consists of a large proof mass, two DETF resonators and four microlevers. Figure 2.7 shows the mechanical structure of the “SRA Design-2”. In this structure, the proof mass is connected to the stationary outer frame as in the “SRA Design-1”. In contrast to the "SRA Design-1," the microlever structure increases the mechanical sensitivity to acceleration. Table 2.2 summarizes the sensor design parameters for “SRA Design-2”.

The stress related problems have been observed on the fabricated device structures of the “SRA Design-1” and “SRA Design-2”. The details of these problems are given in Chapter 3. The third sensor design, called “SRA Design-3”, has been proposed to overcome the stress related problems encountered in the “SRA Design-1” and “SRA Design-2”. Figure 2.8 shows the mechanical structure of the “SRA Design-3”. “SRA Desing-3” consists of a large proof mass, two DETF resonators and four microlevers as in the “SRA Design-2”. As opposed to the “SRA Design-2”, the poof mass is connected to a single anchor located in the center of the sensor structure to minimize the effect of the thermal stress on the DETF resonators. Moreover, the layout of “SRA Design-3” has been improved by filling the empty area near the DETF flexures to prevent the unbalanced etching in the fabrication process. Table 2.3 summarizes the sensor design parameters for “SRA Design-3”.

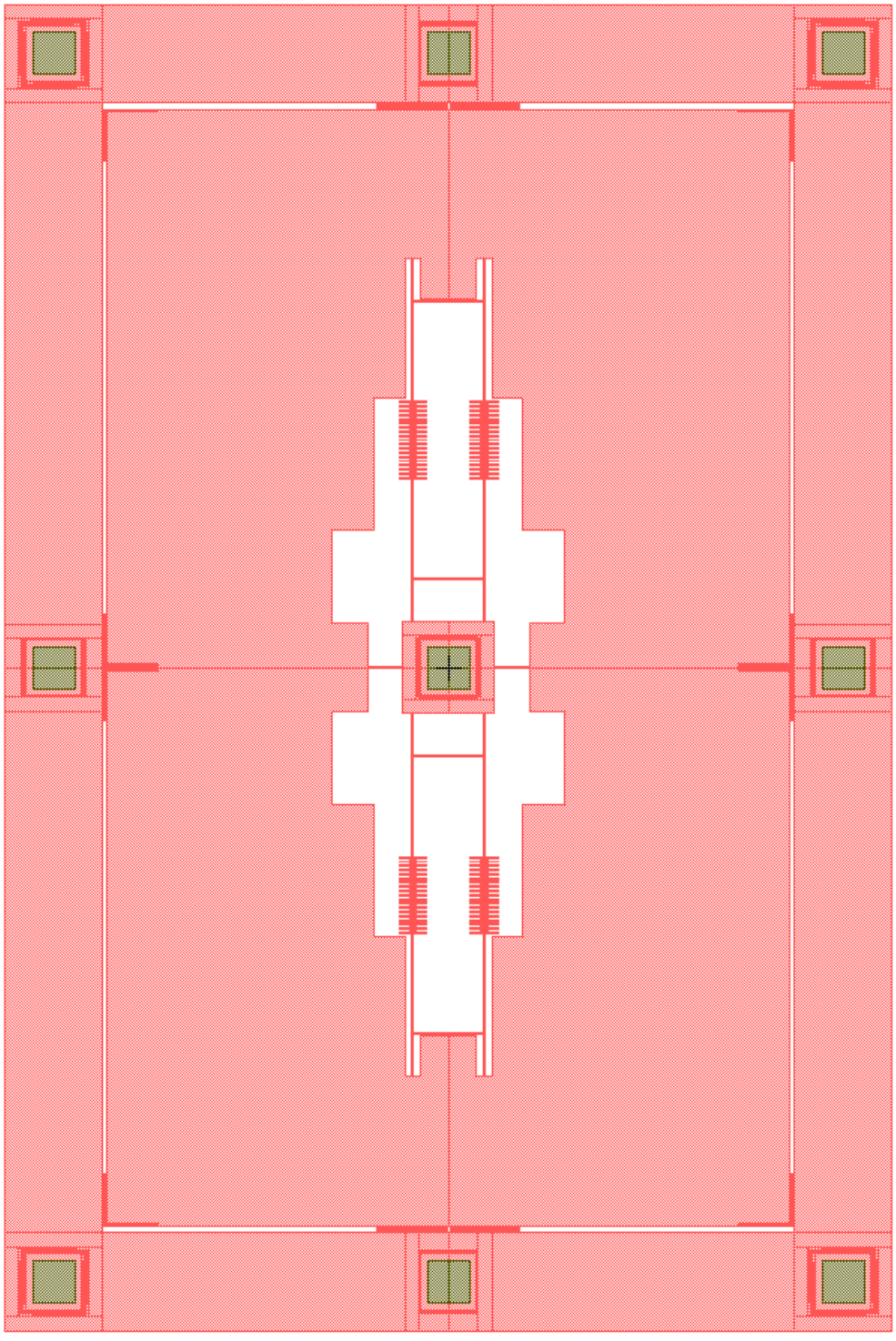


Figure 2.6. The mechanical structure of the “SRA Design-1”.

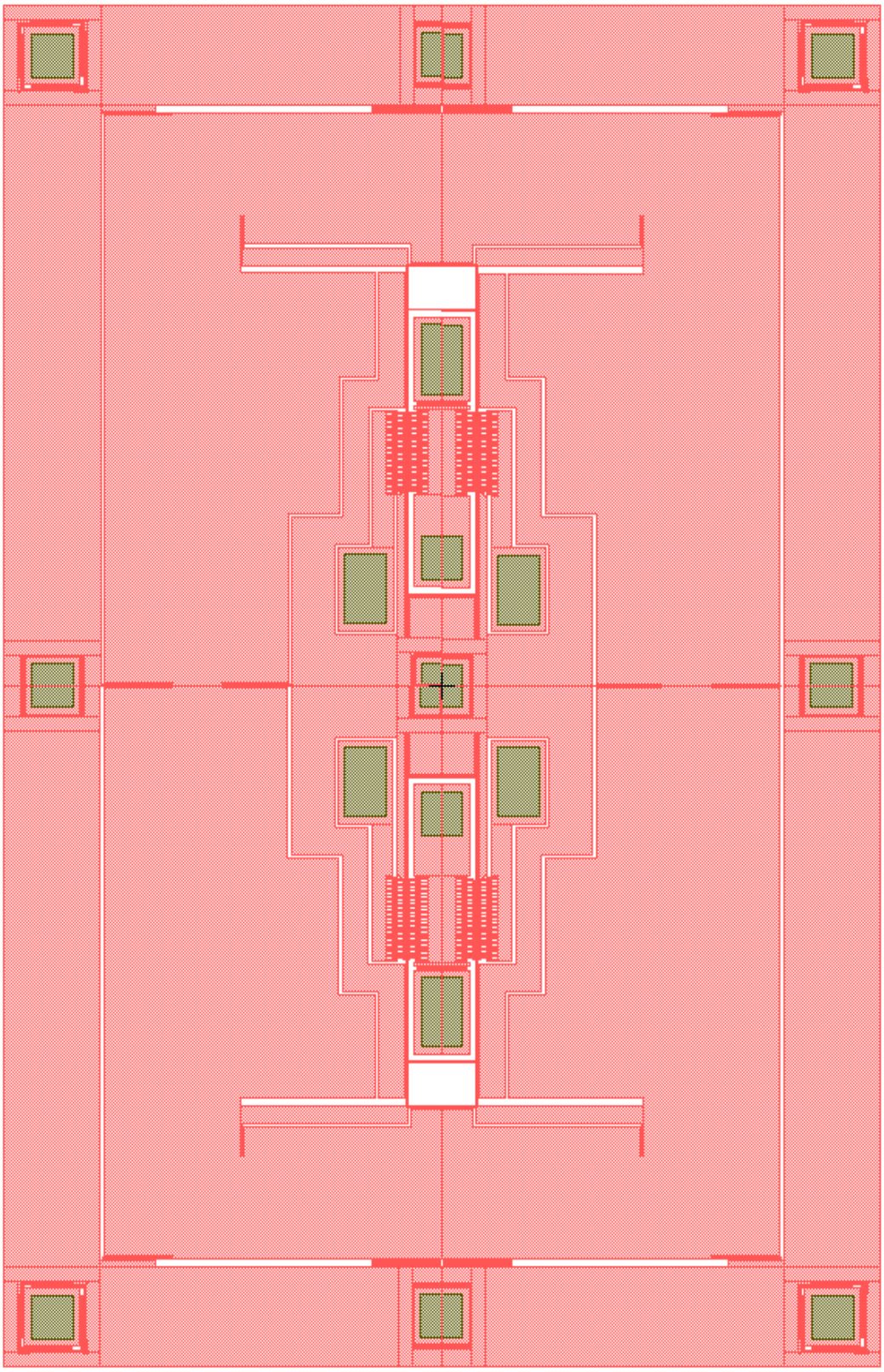


Figure 2.7. The mechanical structure of the “SRA Design-2”.

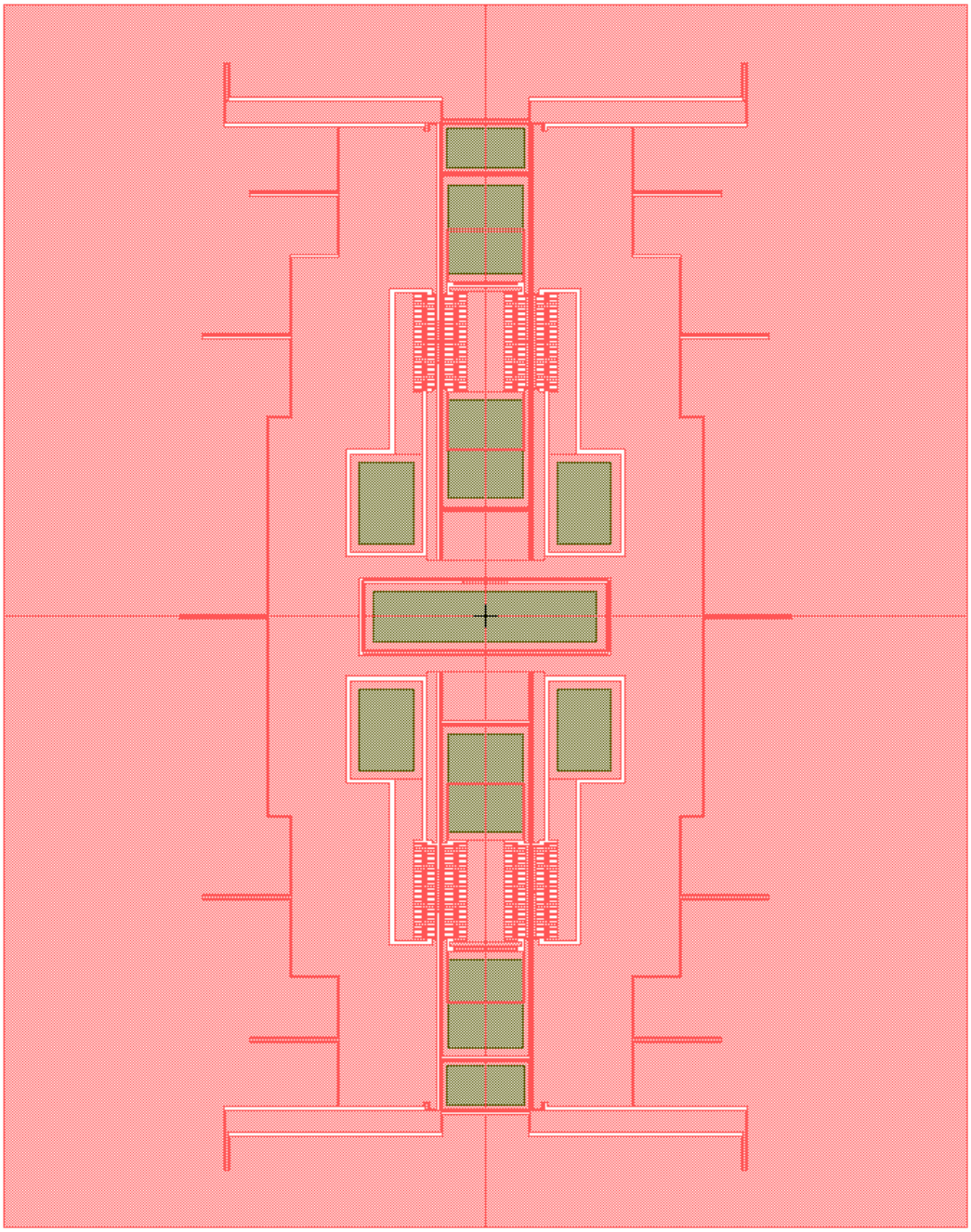


Figure 2.8. The mechanical structure of the “SRA Design-3”.

Table 2.1 Sensor design parameters for SRA Design-1.

Parameter	**Symbol**	**Value**
Mass of proof mass	M	4.4×10^{-7} kg
Bending stiffness of input axis	K_m	953 N/m
Equal axial stiffness	K_{in}	22882 N/m
Effective Amplification Factor	A_{eff}	0.96
In-phase resonance frequency	$f_{o,in}$	21787 Hz
Out-of-phase resonance frequency	$f_{o,out}$	23185 Hz
Calculated diff. scale factor	SF	11.2 Hz/g
Proof mass connection	to the outer frame	

Table 2.2 Sensor design parameters for SRA Design-2.

Parameter	**Symbol**	**Value**
Mass of proof mass	M	3.69×10^{-7} kg
Bending stiffness of input axis	K_m	402 N/m
Equal axial stiffness	K_{in}	197 N/m
Effective Amplification Factor	A_{eff}	4.93
In-phase resonance frequency	$f_{o,in}$	21787 Hz
Out-of-phase resonance frequency	$f_{o,out}$	23185 Hz
Calculated diff. scale factor	SF	48.3 Hz/g
Proof mass connection	to the outer frame	

Table 2.3 Sensor design parameters for SRA Design-3.

Parameter	**Symbol**	**Value**
Mass of proof mass	M	3.33×10^{-7} kg
Bending stiffness of input axis	K_m	578 N/m
Equal axial stiffness	K_{in}	197 N/m
Effective Amplification Factor	A_{eff}	3.81
In-phase resonance frequency	$f_{o,in}$	21787 Hz
Out-of-phase resonance frequency	$f_{o,out}$	23185 Hz
Calculated diff. scale factor	SF	33.6 Hz/g
Proof mass connection	to the single anchor	

2.3 Finite-Element Simulations

The design of the silicon resonant accelerometer is based on the mathematical equations given above. In most cases, however, the approximations and assumptions used to simplify the preliminary analysis usually introduce errors. A series of simulations is a good way to predict these errors and validate the theoretical analysis.

The finite-element method (FEM) is a computational method for evaluating the behavior of sophisticated systems. In this technique, the real problem is replaced by a simpler one to find an approximate solution for the problem. The DETF resonator is the core sensing element in the silicon resonant accelerometer, and the same DETF structure is used in all sensor designs. Thus, as a first step, the modal frequencies and mode shapes of the DETF resonator are verified by the modal analysis. Then, three different FEM analyses have been performed on each device structure: modal analysis, force simulations, and temperature simulations. Firstly, the modal analysis is done to simulate the modal frequencies and mode shapes corresponding to the SRA structure with a large proof mass. Force simulations are then performed to determine the acceleration sensitivity and nonlinearity of the corresponding sensor

structure. Finally, temperature simulations are carried out to optimize the stress release beams and measure the acceleration sensitivity of the corresponding sensor structure. The FEM simulations are done with COMSOL, which is a simulation platform that works well with MEMS devices.

2.3.1 Modal Analysis of DETF Resonator

The mode frequencies and mode shapes of the analyzed device are identified using modal analysis. Although the resonance frequencies of the DETF resonator can be approximated by hand calculation, modal analysis makes it easier to determine the exact difference between the in-phase and out-of-phase mode frequencies. The DETF resonator is operated in an out-of-phase mode to increase the quality factor and drive efficiency. A minimum 10% difference is preferred between the mode frequencies of the out-of-phase mode (the drive mode) and the in-phase mode (the parasitic hula mode) to guarantee that the hula mode will not interact with the oscillator drive loop. Figure 2.9 and Figure 2.10 show the in-phase mode and out-of-phase mode of the DETF resonator, respectively. The undercut in the flexure beams due to the fabrication is not taken into consideration in this FEM analysis. The simulated value of the out-of-phase mode resonance frequency is 24316 Hz, whereas the in-phase mode resonance frequency is about 22849 Hz.

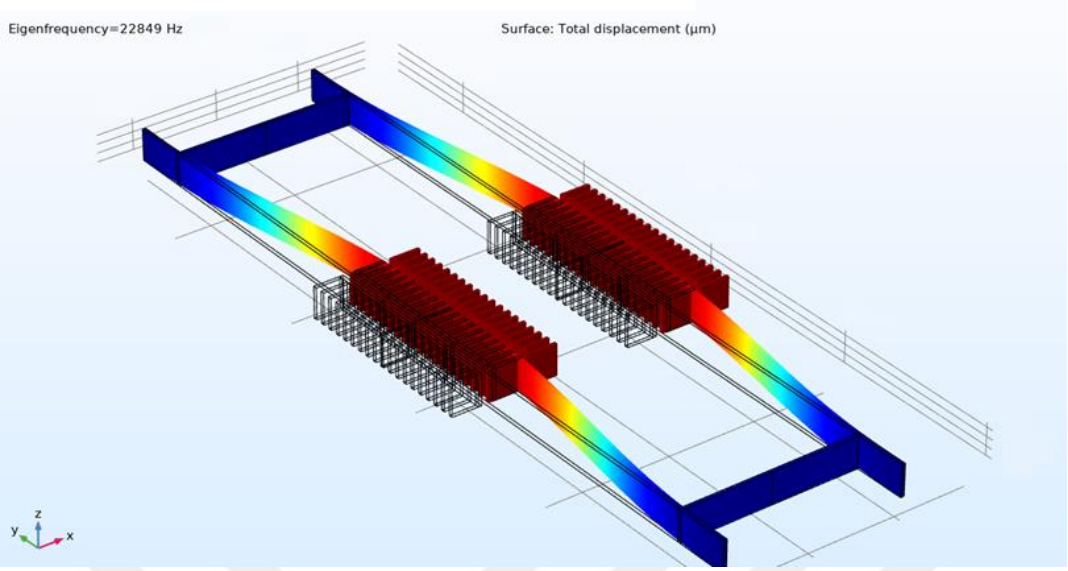


Figure 2.9. The in-phase mode of DETF in COMSOL: 22849Hz.

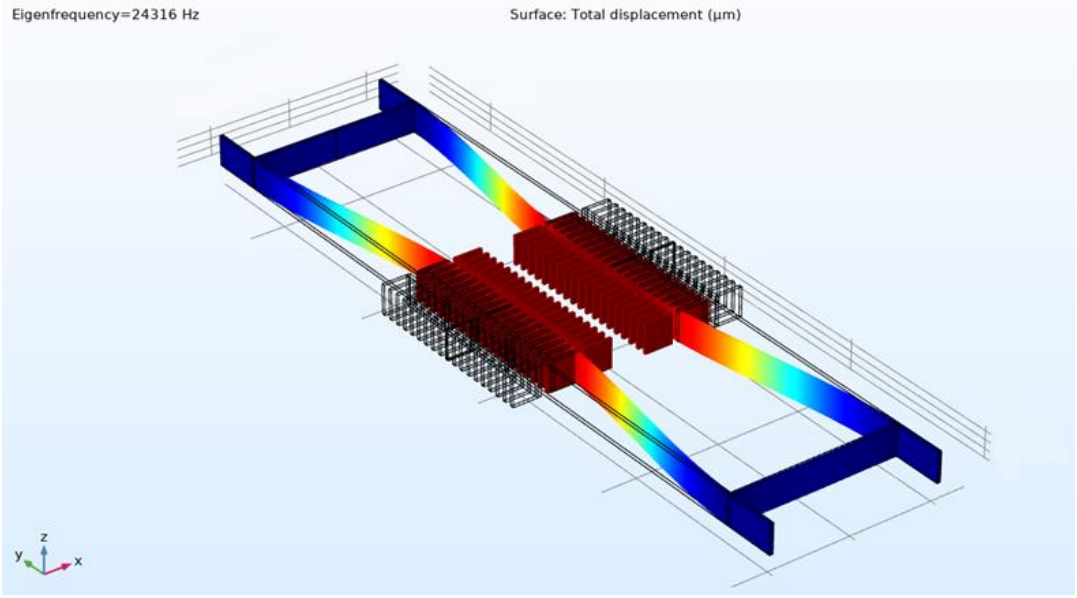


Figure 2.10. The out-of-phase mode of DETF in COMSOL: 24316Hz.

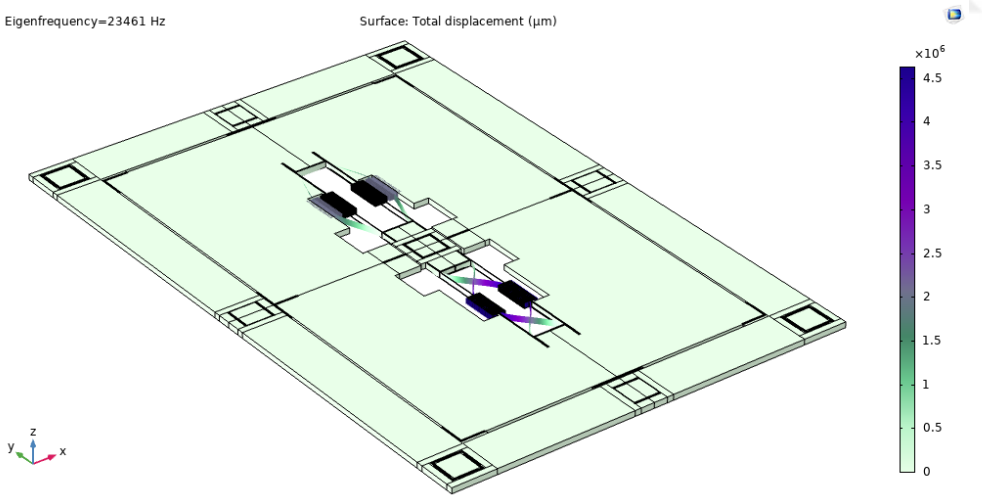
2.3.2 Modal Analysis of Silicon Resonant Accelerometer Designs

The modal analysis is repeated for all silicon resonant accelerometers one by one to observe the mode frequencies and shapes of the corresponding sensor structure. Enlarging the proof mass decreases the natural frequencies of the in-plane and out-of-plane modes of the sensor structure, so these modes are expected to appear due to the large proof mass. Although identical DETF resonators are employed between the upper and lower parts of the sensor structure, a small frequency split might exist between their resonance frequencies because of the coupling between them through the proof mass. Moreover, integrating the microlevers with the proof mass decreases the axial spring constant of the sensor structure, as shown in Figure 2.4. As a result, the resonance frequency of the axial mode is expected to be lower in the SRA Design-2 and SRA Design-3 compared to the SRA Design-1.

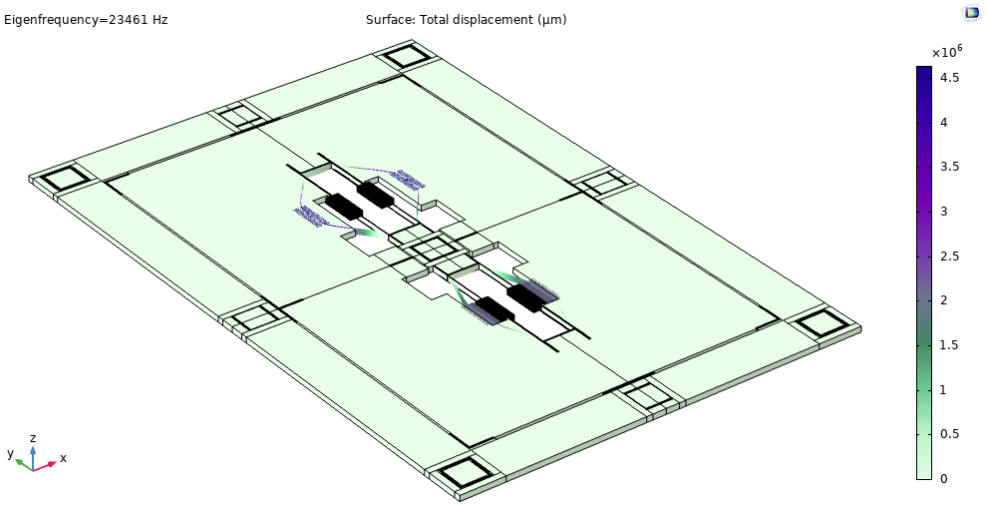
The same modal analysis has been applied to all three sensor designs described in Section 2.2 using COMSOL, respectively. Table 2.4 demonstrates the resonance frequency list of the simulated first 10 modes for the first sensor design, i.e., the SRA Design-1. The main operational modes of the sensor are the third and fourth modes, which are the out-of-phase modes of the two DETF resonators. The higher-order modes are related to the out-of-plane modes of the proof mass. Figure 2.11 shows the mode shapes of the out-of-phase modes of the two DETF resonators and the rotational mode along the vertical axis for the SRA Design-1.

Table 2.4 Modal analysis results of the SRA Design-1.

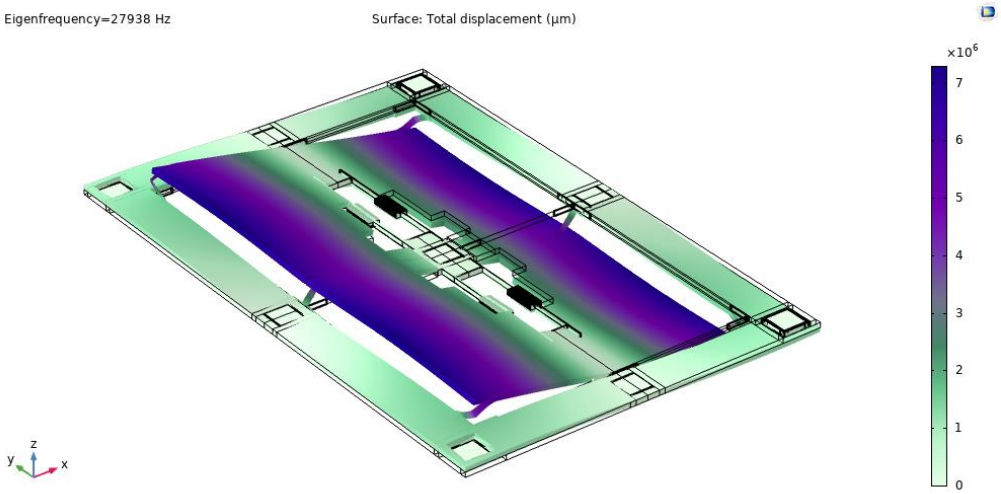
Mode#	Resonance Frequency (Hz)	Name of Mode
1	21281.7	In-phase
2	21286.4	In-phase
3	23460.7	Out-of-Phase
4	23460.8	Out-of-Phase
5	27937.6	Rotational along vertical axis
6	29478.9	Out-of-plane
7	30822.3	Rotational along horizontal axis
8	36141.9	Rotational along transverse axis
9	46979.8	-
10	48392.3	-



(a) Mode shape for the out-phase mode of the first DETF resonator



(b) Mode shape for the out-phase mode of the second DETF resonator



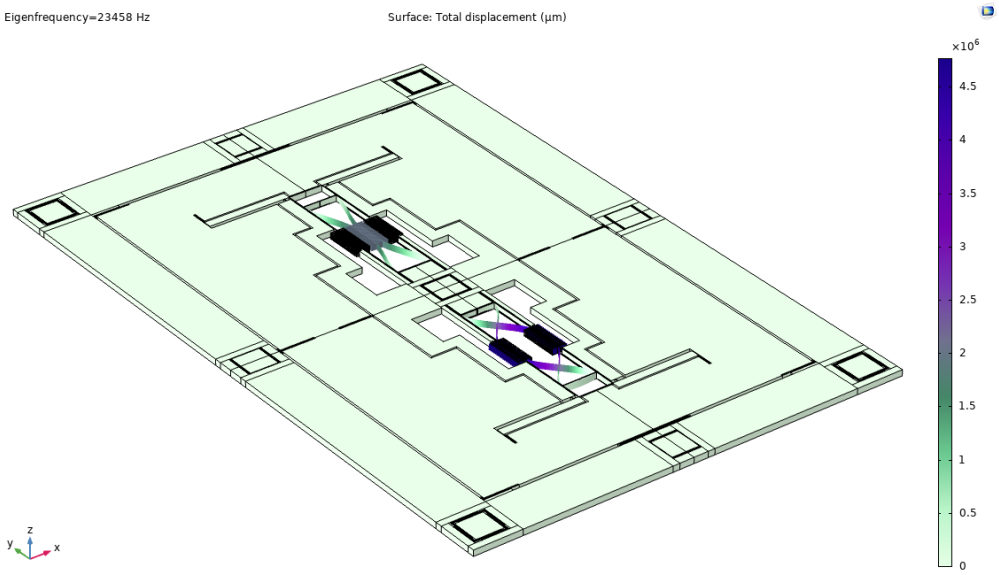
(c) Mode shape for the rotational mode along the vertical axis

Figure 2.11. The mode shapes for SRA Design-1.

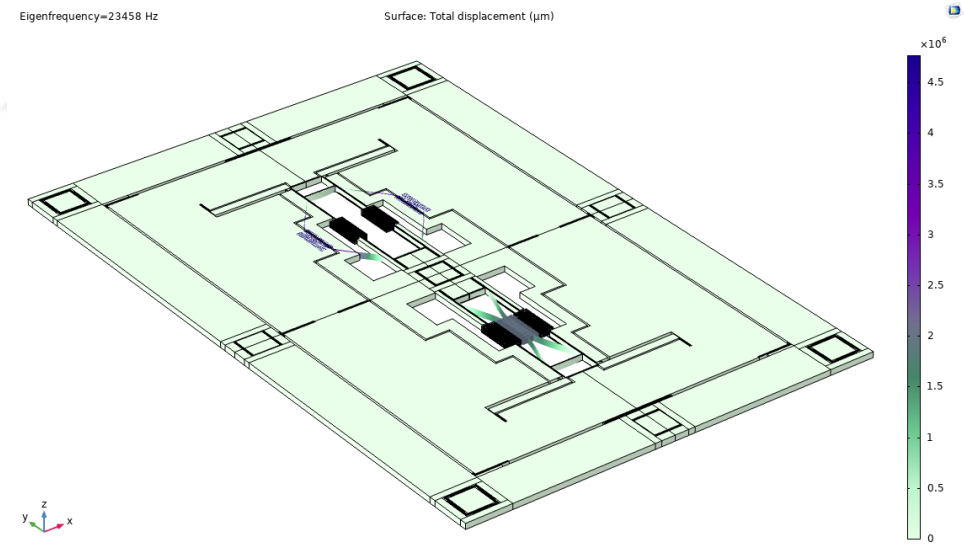
Table 2.5 demonstrates the resonance frequency list of the simulated first 10 modes for the second sensor design, i.e., the SRA Design-2. The main operational modes of the sensor are the fourth and fifth modes, which are the out-of-phase modes of the two DETF resonators. The integration of the microlevers into the proof reduces the axial spring constant of the structure, resulting in a decrease in the resonance frequency of the axial mode of the proof mass. The other higher-order modes are related to the out-of-plane modes of the proof mass. Figure 2.12 shows the mode shapes of the out-of-phase modes of the two DETF resonators and the axial mode of the proof mass for the SRA Design-2.

Table 2.5 Modal analysis results of the SRA Design-2.

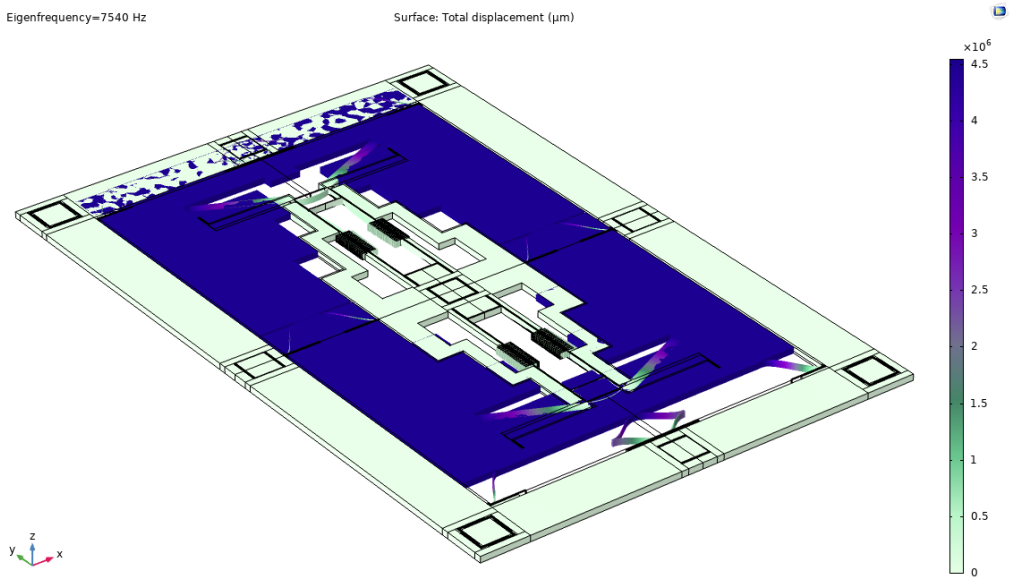
Mode#	Resonance Frequency (Hz)	Name of Mode
1	7540.0	Axial
2	21221.1	In-phase
3	21255.5	In-phase
4	23457.6	Out-of-Phase
5	23458.1	Out-of-Phase
6	25478.3	Out-of-plane
7	26797.7	Rotational along vertical axis
8	27799.6	Rotational along horizontal axis
9	32232.9	Rotational along transverse axis
10	38147.5	-



(a) Mode shape for the out-phase mode of the first DETF resonator



(b) Mode shape for the out-phase mode of the second DETF resonator



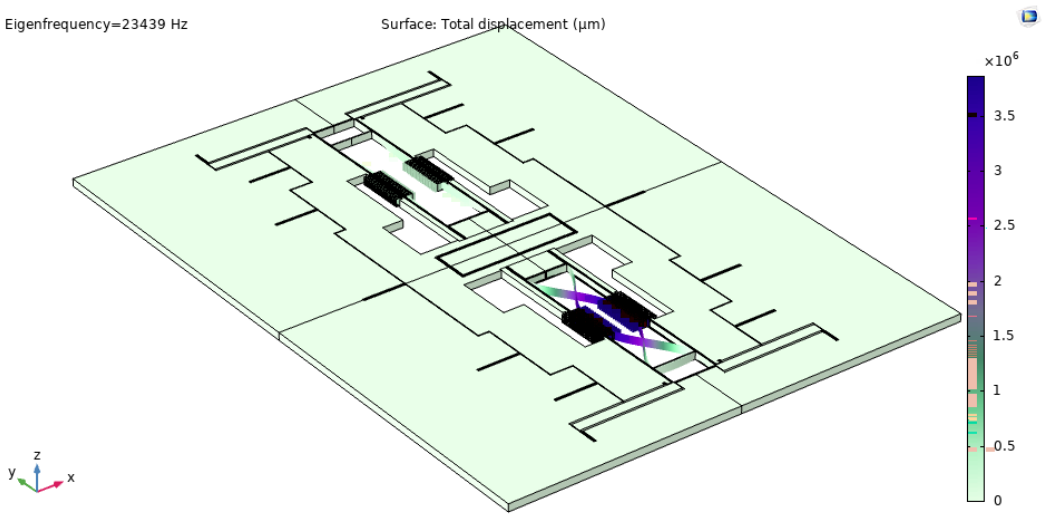
(c) Mode shape for the axial mode of the proof mass

Figure 2.12. The mode shapes for SRA Design-2.

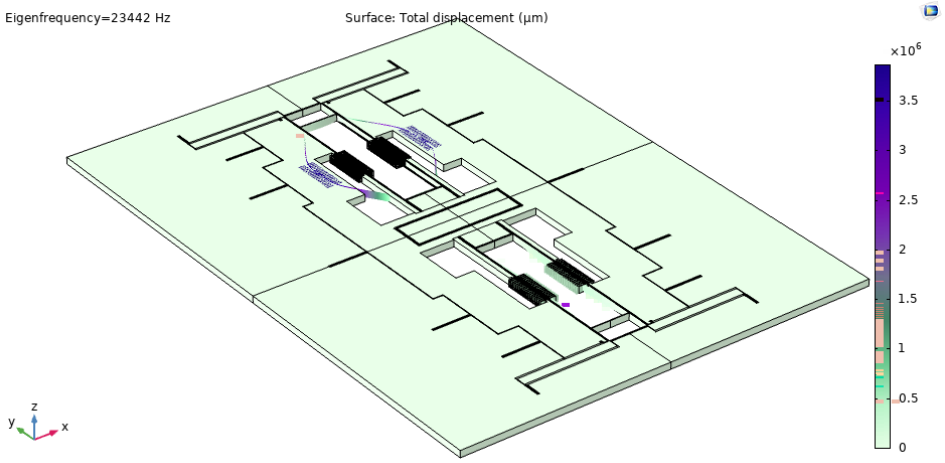
Table 2.6 demonstrates the resonance frequency list of the simulated first 10 modes for the third sensor design, i.e., the SRA Design-3. The main operational modes of the sensor are the ninth and tenth modes, which are the out-of-phase modes of the two DETF resonators. The proof mass moves more easily in the out-plane when it is connected to a single point anchor rather than an outer frame. As a result, the resonance frequencies of the out-of-plane modes of the structure are at lower frequencies compared to the SRA Design-1 and SRA Design-2. Figure 2.13 shows the mode shapes of the out-of-phase modes of the two DETF resonators and the rotational mode of the proof mass along the horizontal axis for the SRA Design-3.

Table 2.6 Modal analysis results of the SRA Design-3.

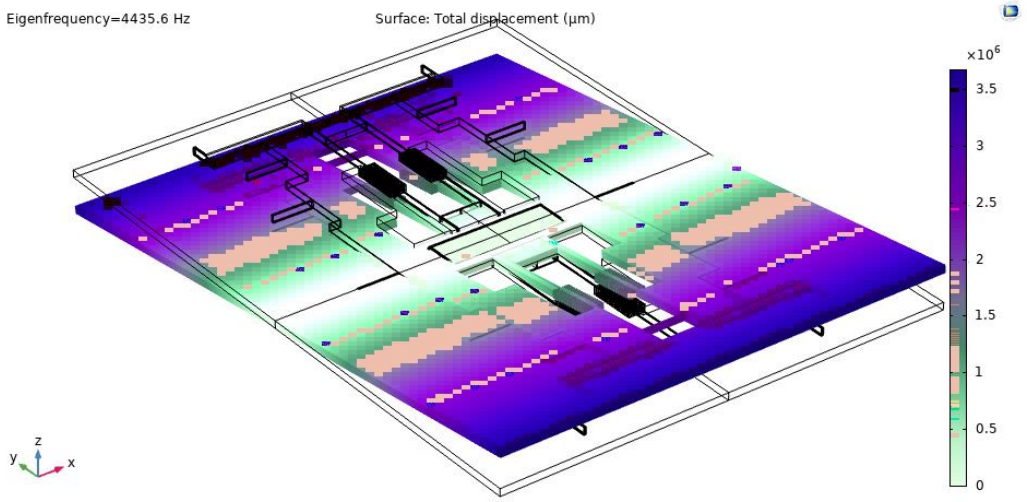
Mode#	Resonance Frequency (Hz)	Name of Mode
1	4435.5	Rotational along horizontal axis
2	8125.1	Axial
3	10772.9	Rotational along vertical axis
4	13123.2	Out-of-Plane
5	17570.1	In-plane rotary
6	20098.5	Rotational along transverse axis
7	21338.5	In-phase
8	21256.4	In-phase
9	23439.1	Out-of-phase
10	23441.53	Out-of-phase



(a) Mode shape for the out-phase mode of the first DETF resonator



(b) Mode shape for the out-phase mode of the second DETF resonator



(c) Mode shape for the rotational mode along the horizontal axis

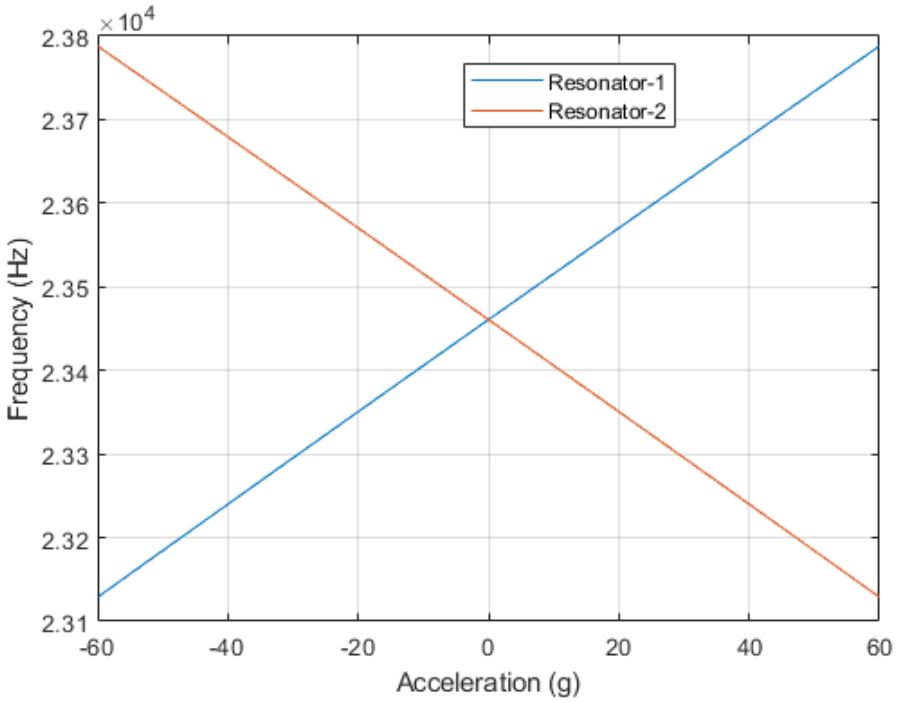
Figure 2.13. The mode shapes for SRA Design-3.

2.3.3 Force Simulations

The force simulations are performed to obtain the frequency changes of the DETF resonators in response to the force applied along the measurement axis of the corresponding sensor structure for all designs in COMSOL. Equation 2.17 can be used to get an approximation of the scale factor of the silicon resonant accelerometer, but FEM simulations give more accurate results. Table 2.7 provides the frequency list of the DETF resonators in response to the different acceleration force along the sense axis for the first sensor design, i.e., SRA Design-1. Figure 2.14 visualizes the force simulation results for the corresponding sensor design.

Table 2.7 Force simulation results for SRA Design-1 in COMSOL.

Applied Acceleration (g)	Resonator-1 Frequency (Hz)	Resonator-2 Frequency (Hz)	SF (Hz/g)
-60	23128.8	23788.0	
-50	23184.5	23733.8	
-40	23240.0	23679.4	
-30	23295.4	23625.0	
-20	23350.7	23570.4	
-10	23405.8	23515.6	
-5	23433.4	23488.2	
-2	23449.9	23471.7	
-1	23455.3	23466.3	
0	23460.9	23460.7	10.99
1	23466.3	23455.3	
2	23471.7	23449.9	
5	23488.2	23433.4	
10	23515.6	23405.8	
20	23570.4	23350.7	
30	23625.0	23295.4	
40	23679.4	23240.0	
50	23733.8	23184.5	
60	23788.0	23128.8	



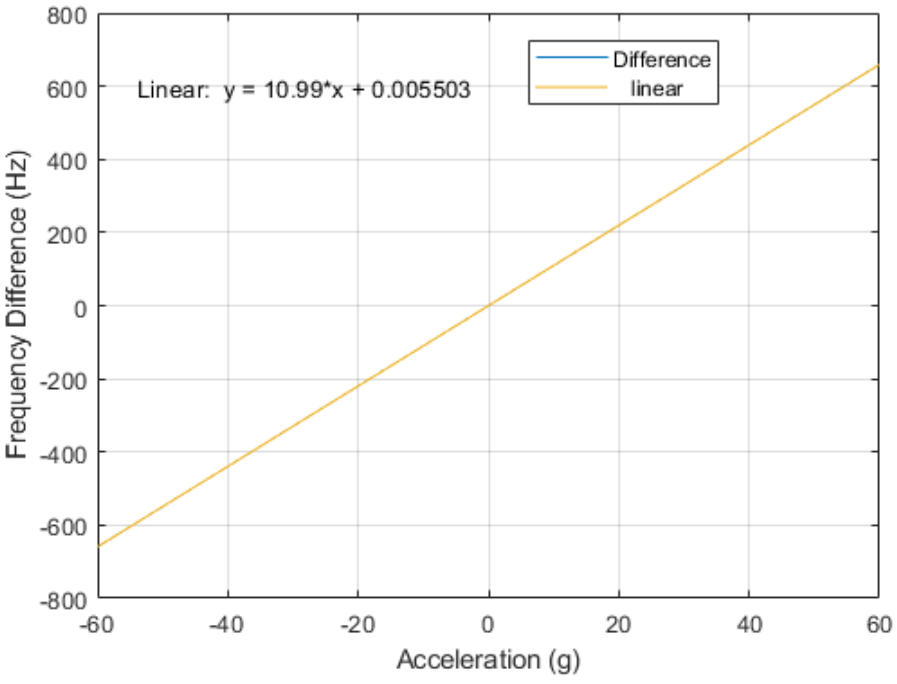


Figure 2.14. Responses of the SRA Design-1 to the accelerations applied along the measurement axis in FEM simulations.

Table 2.8 provides the frequency list of the DETF resonators in response to the different acceleration force along the sense axis for the second sensor design, i.e., SRA Design-2. Figure 2.15 visualizes the force simulation results for the corresponding sensor design. It should be noted that the scale factor has a negative sign because the microlever inverts the sign of the input force transferring it to the output.

Table 2.8 Force simulation results for SRA Design-2 in COMSOL.

Applied Acceleration (g)	Resonator-1 Frequency (Hz)	Resonator-2 Frequency (Hz)	SF (Hz/g)
-60	24806.3	22026.1	
-50	24586.8	22271.2	
-40	24365.3	22513.6	
-30	24141.7	22753.3	
-20	23916.0	22990.5	
-10	23688.2	23225.3	
-5	23573.4	23341.8	
-2	23504.3	23411.4	
-1	23481.2	23434.6	
0	23458.1	23457.6	-46.31
1	23434.9	23480.8	
2	23411.8	23503.9	
5	23342.1	23573.0	
10	23225.6	23687.8	
20	22990.8	23915.6	
30	22753.6	24141.3	
40	22513.8	24364.8	
50	22271.4	24586.3	
60	22026.3	24805.8	

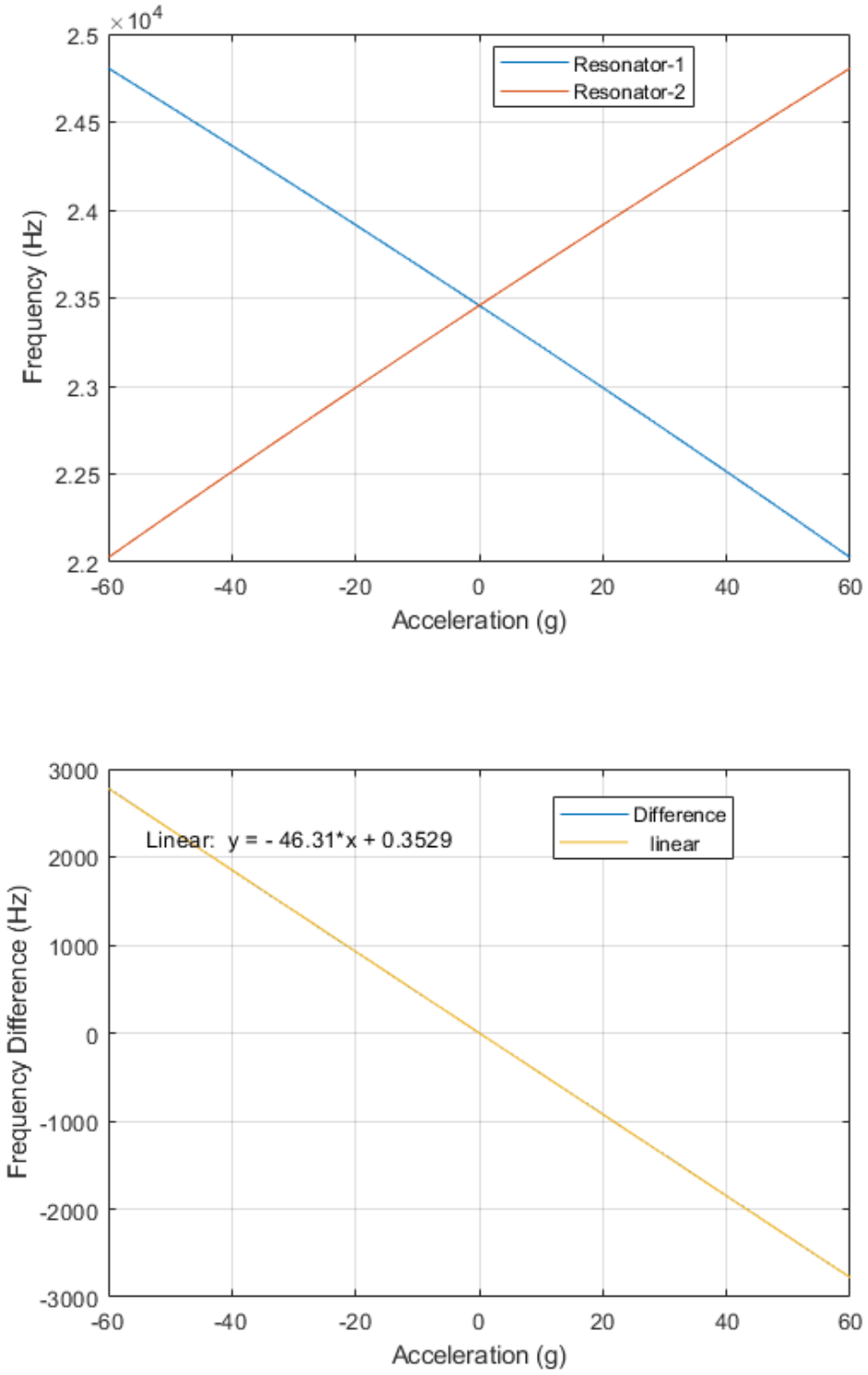


Figure 2.15. Responses of the SRA Design-2 to the accelerations applied along the measurement axis in FEM simulations.

Table 2.9 provides the frequency list of the DETF resonators in response to the different acceleration force along the sense axis for the third sensor design, i.e., SRA Design-3. Figure 2.16 visualizes the force simulation results for the corresponding sensor design.

Table 2.9 Force simulation results for SRA Design-3 in COMSOL.

Applied Acceleration (g)	Resonator-1 Frequency (Hz)	Resonator-2 Frequency (Hz)	SF (Hz/g)
-60	24396.3	22443.4	
-50	24239.8	22612.4	
-40	24082.3	22780.2	
-30	23923.7	22946.7	
-20	23764.1	23112.0	
-10	23603.3	23276.1	
-5	23522.6	23357.8	
-2	23474.0	23406.6	
-1	23457.8	23422.9	
0	23441.5	23439.1	-32.50
1	23425.3	23455.3	
2	23409.0	23471.6	
5	23360.2	23520.2	
10	23278.6	23600.9	
20	23114.5	23761.7	
30	22949.2	23921.3	
40	22782.7	24079.9	
50	22615.0	24237.5	
60	22446.0	24394.0	

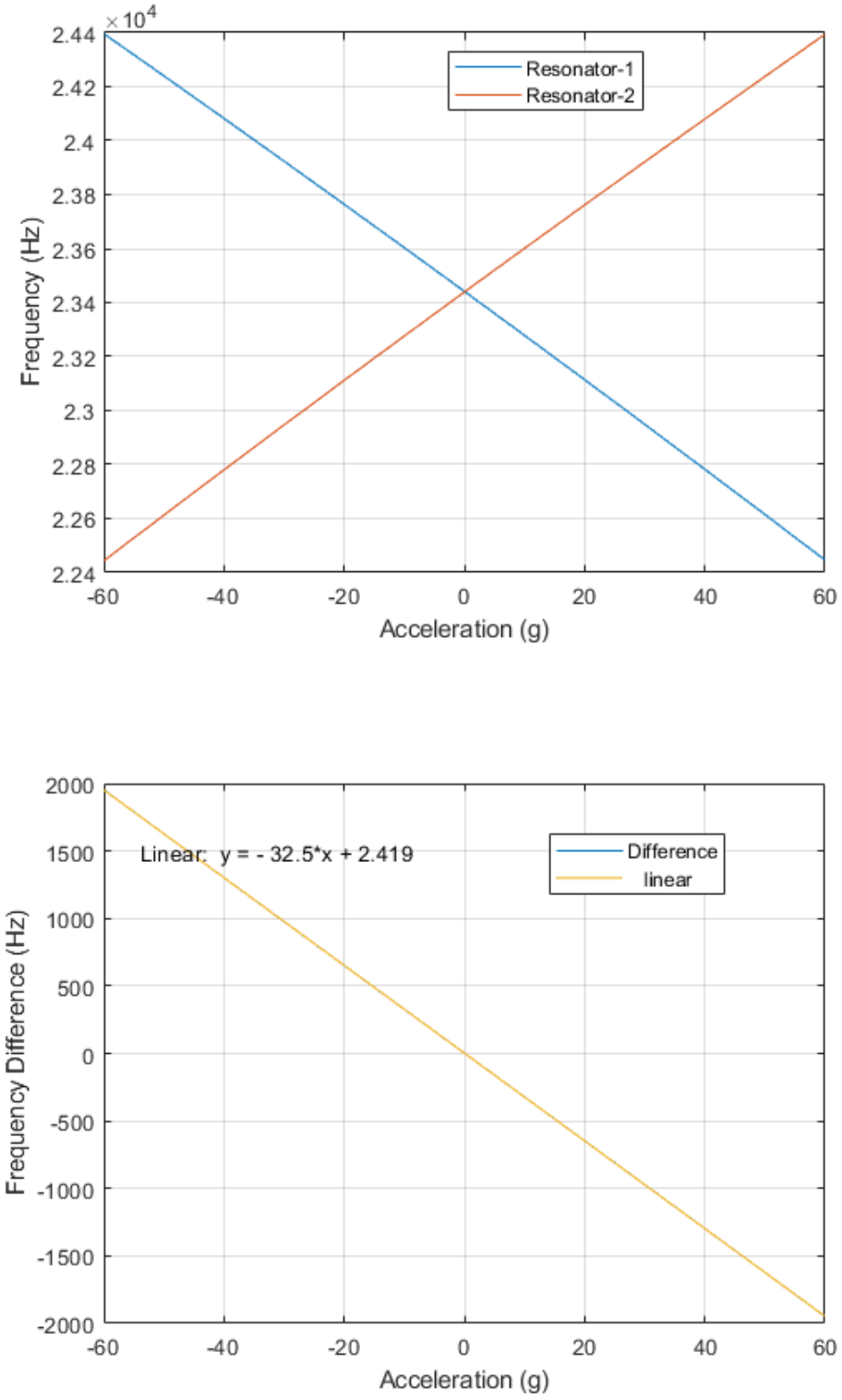


Figure 2.16. Responses of the SRA Design-3 to the accelerations applied along the measurement axis in FEM simulations.

2.3.4 Temperature Simulations

The quick temperature simulations gave an idea of how to optimize the structure of the device to mitigate the thermal stress on the structure at the design stage for all three sensor designs. However, the systematic temperature simulations are done for only the third design, i.e., SRA Design-3, to figure out the temperature sensitivity of the sensor. In the sensor fabrication process, the silicon device structure is bonded to the glass anchors; therefore, the thermal expansion coefficient difference between the silicon structure and glass anchor might cause a thermal stress on the DETF resonators. The Young's modulus and thermal expansion coefficient of silicon are temperature dependent; thus, the material properties of the silicon and glass should be chosen correctly to construct a realistic temperature simulation model for SRA Design-3. The details about material properties of silicon (111) can be found in [10]. The undercut in the device structure is included in the simulation model to obtain results that are compatible with the experimental ones.

The temperature simulations are repeated three times for three different conditions, ranging from -40 °C to +80 °C with a temperature step of 20 °C. In all conditions, the single anchor device structure is used, but with small differences. In the first condition, the real case is simulated, i.e., the anchor material is chosen as glass and the structure material is chosen as silicon. The resonance frequency of the DETF resonator at 20 °C is adjusted to be almost equal to the resonance frequency of the fabricated sensor at room temperature by simulating a device structure with an undercut. In the second condition, the same sensor structure is simulated, but the anchor material is chosen to be silicon, eliminating the thermal stress effect on the DETF resonators. This condition is called an "ideal case". In the third condition, the stress release beams are not used in the connection of the stationary silicon part to the anchor. In this condition, the anchor material is chosen as glass, and the structure material is chosen as silicon. In these simulations, the frequency output of one DETF resonator is monitored to compare the results under three conditions since both DETF resonators have the exactly same temperature characteristics in the simulation.

Table 2.10 provides the temperature simulation results under three different conditions for the SRA Design-3. The simulation results indicate that the single-anchor design with stress release beams, i.e., SRA-Design-3, drastically improves the temperature sensitivity of the resonator's frequency while suppressing thermal stress effects on the sensing flexures. While in the ideal case, the temperature dependence of silicon's Young's modulus is the only factor changing the resonator's frequency with varying temperature, the residual thermal stress also has an effect on the resonator's frequency in the real case. Figure 2.17 shows the change of the DETF resonator frequency with temperature for SRA Design-3 under three different conditions in FEM simulations.

Table 2.10 Temperature simulation results for three different conditions of SRA Design-3 in COMSOL.

Temp. (°C)	**Case-1: Real Case Anchor: glass, Structure: silicon With stress release**		**Case-2: Ideal Case Anchor: silicon Structure: silicon With stress release**		**Case-3: Anchor: glass, Structure: silicon Without stress release**	
	Resonator Frequency (Hz)	Total Freq. Change (Hz)	Resonator Frequency (Hz)	Total Freq. Change (Hz)	Resonator Frequency (Hz)	Total Freq. Change (Hz)
80	17001,6	-12,8	16999,2	-20,1	16938,1	-215,0
60	17004,1		17002,2		16956,2	
40	17006,5		17005,2		16979,4	
20	17008,7		17008,7		17009,0	
0	17010,8		17012,5		17048,2	
-20	17012,7		17015,8		17096,3	
-40	17014,4		17019,3		17153,1	

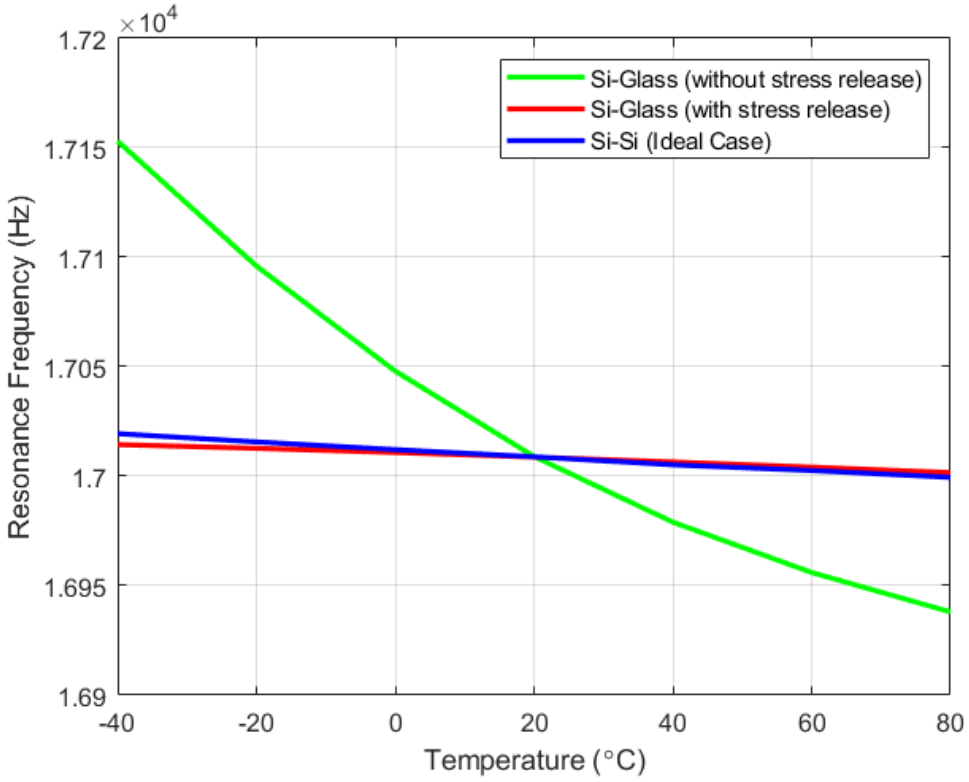


Figure 2.17. Change of the DETF resonator frequency with temperature for SRA Design-3 under three different conditions in FEM simulations.

2.4 Summary

This chapter presented the theory of the silicon resonant accelerometer and provided the analytical model of the accelerometers developed in this work. Firstly, it described the basic operating principle of the silicon resonant accelerometer. Then, the analytical solutions for the force sensitivity of the DETF resonator and the amplification factor of microlever were given. Next, the temperature sensitivity and stiffness nonlinearity of the DETF resonator were examined. Finally, the finite element simulations performed during the design were presented, including modal analysis, force simulations, and temperature simulations for predicting the performance of the silicon resonant accelerometer before the fabrication.

CHAPTER 3

FABRICATION OF MEMS RESONANT ACCELEROMETERS

This chapter presents the fabrication process for the silicon resonant accelerometers in this study. In the fabrication process, vertical feedthroughs on an SOI cap wafer are used, which is then anodically bonded to a corresponding MEMS device wafer fabricated with a Silicon-on-Glass (SOG) process [58]. This is referred to as the "Advanced MEMS1" (aMEMS1) process [59]. Section 4.1 gives information about the aMEMS1 process steps in detail. Section 4.2 presents the fabrication results and describes the problems related to the specific sensor design. Section 4.3 summarizes the chapter.

3.1 Advanced MEMS1 (aMEMS1) Process with Anodic Bonding

This section demonstrates the process steps of the "Advanced MEMS1" (aMEMS1) method for fabricating the silicon resonant accelerometers designed in this study. The first step of the aMEMS1 process is the fabrication of the sensor wafer using the silicon-on-Glass (SOG) process. The second step is the formation of the vertical feedthroughs and getter deposition on the SOI cap wafer. The final step is the wafer-level hermetic encapsulation of the sensor wafer with the SOI cap wafer with help of anodic bonding.

3.1.1 Sensor Wafer Fabrication Based on the SOG Process

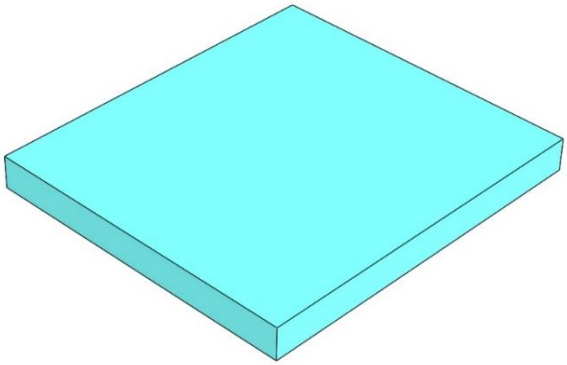
The SOG process involves the fabrication of a glass wafer and an SOI wafer, followed by the anodic bonding of these two wafers to form the sensor wafer. This process includes the construction of the anchors and electrical metal connections on

the glass wafer. The process starts with the anchor construction. Anchors function as the bonding areas on the glass wafer to which the SOI wafer will be joined by anodic bonding. Firstly, a thin film metal is coated on the glass wafer using the thermal evaporation process. Next, the thin film metal layer is formed using wet etchants. Then, the anchor structures are constructed by etching glass in a pure HF solution. Following the completion of the anchor construction, the thin film metal layers are removed by the wet etchant process.

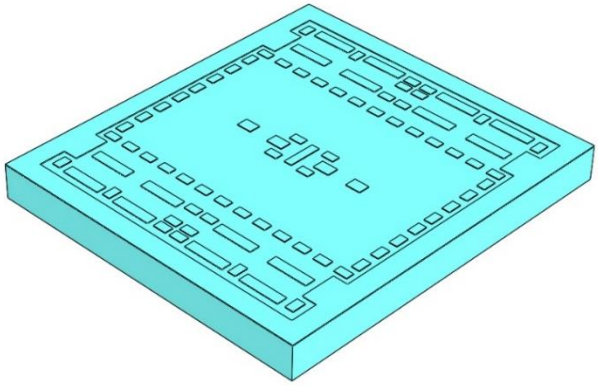
The next step in the fabrication of glass wafers is the patterning of electrical wires. Thin film metal layer first coated by thermal evaporation. Then, thin film metal is patterned using wet chemical etchants to construct the pad metallization. This is the final step in the process of glass wafers.

The SOI wafer process includes the construction of the device structure on the device layer with the DRIE. This process step is the most critical step of the sensor fabrication because any error coming from the lithography or silicon etching process directly affects sensor parameters. DRIE enables anisotropic etching in silicon, making it the best method for forming device structures with critical dimensions.

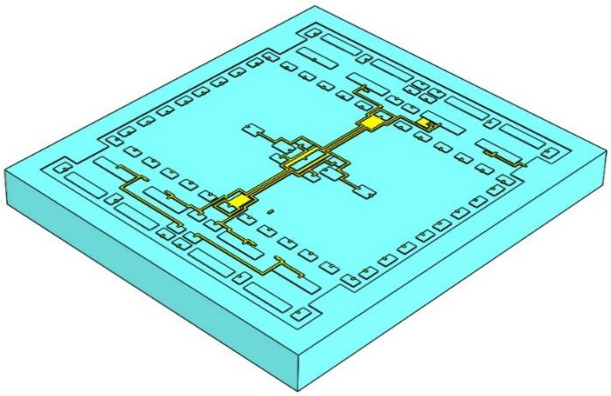
The following process step is the anodic bonding of the glass and SOI wafers using the approach described in [60]. The handle layer of the SOI wafer can be etched either by dry or wet etch methods after anodic bonding. In the final step, the suspended accelerometer structures on the SOI wafer are released after etching the buried oxide layer. Figure 3.1 shows the fabrication steps of the sensor wafer based on the SOG process.



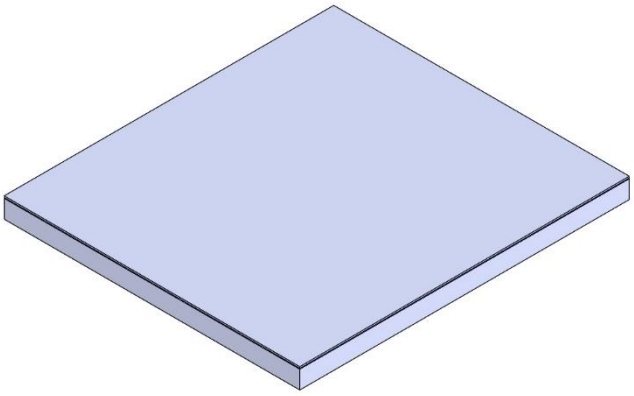
(a) Blank glass wafer



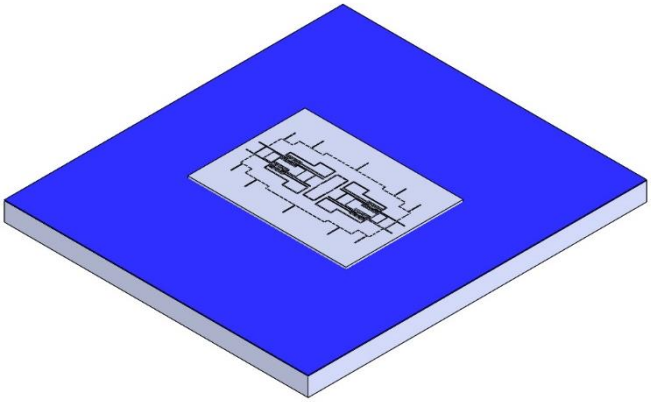
(b) Anchor construction



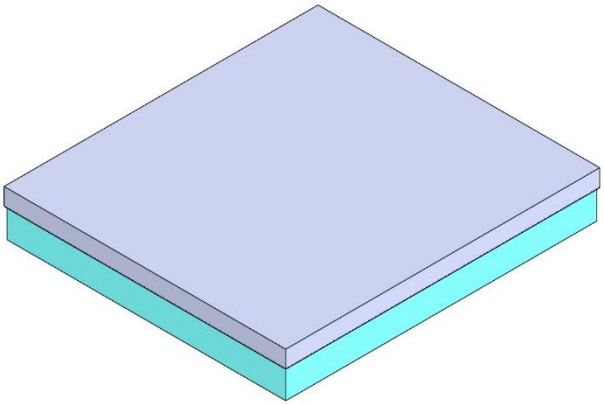
(c) Construction of the electrical wires



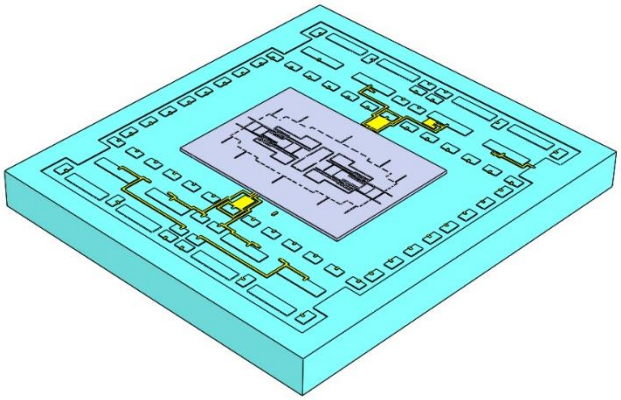
(d) Blank SOI wafer



(e) Sensor structure formation



(f) Anodic bonding of glass and SOI wafers



(g) Release of the sensor structure

Figure 3.1: Fabrication process of the silicon resonant accelerometer wafer.

3.1.2 Wafer-Level Hermetic Packaging of Silicon MEMS Resonant Accelerometers

The sensor wafer of the silicon resonant accelerometer is hermetically packaged with an SOI cap wafer at the wafer lever. In this process, the vertical feedthroughs are utilized to bring the electrical contact points of the sensor structures to the outside of the encapsulated volume. The fabrication of the SOI cap wafer includes four major steps: via openings, formation of the wire bonding pads, formation of the vertical feedthroughs, and getter deposition.

SOI cap wafer process starts with the formation of via openings on the handle layer. Firstly, the thermal oxide layer on the handle layer is patterned by wet etch. Then, the via openings are also shaped by wet anisotropic etching of the handle layer.

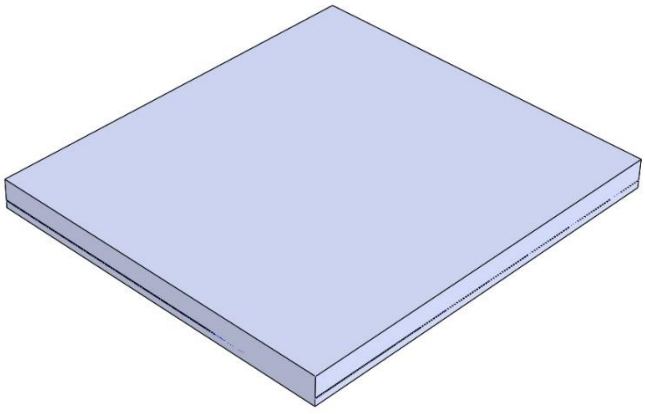
The next step of the SOI cap wafer process is the formation of the wire bonding pads inside the wells. First, a portion of the buried oxide layer between the device and handle layers is patterned by wet etch in order to access the device layer of the SOI from the side of the handle layer. The wafer's handle layer is then coated with thin film metal. Finally, thin film metal is patterned using a lift-off process, and wire

bonding pads contacting the device layer inside the wells on the handle layer are created.

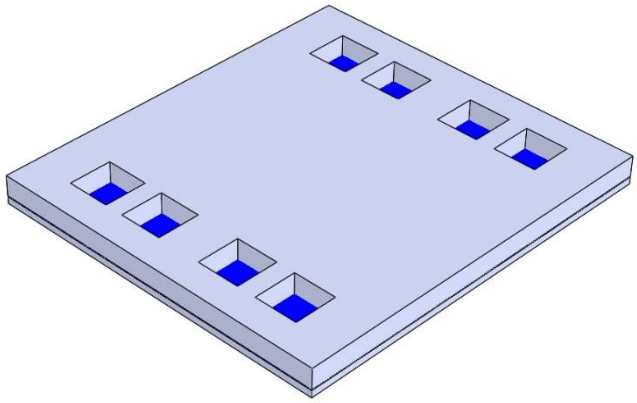
The fabrication of sealing walls and vertical feedthroughs on the device layer is the next step for the SOI cap wafer process. The vertical feedthroughs enable the signal transmission between the sensor pads and the wire bonding pads. The device layer is etched using the DRIE process at this phase.

The next step for the fabrication of the SOI cap wafer is the deposition of the getter inside the sealing wall to absorb the certain kind of gases. A metal is used as the getter material, which is deposited using sputtering. This is the final step in the SOI cap wafer manufacturing process.

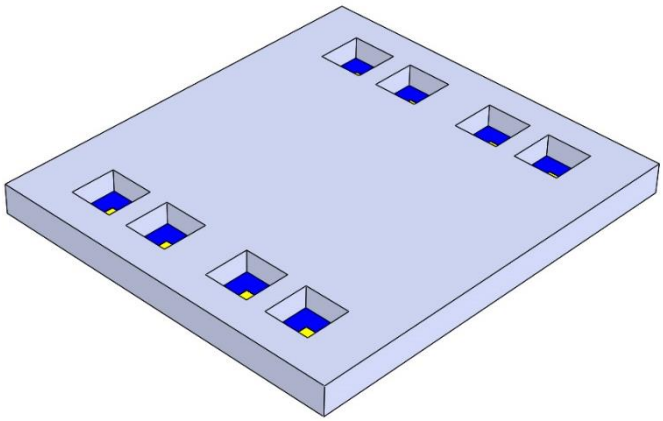
The final step of the aMEMS1 process is the anodic bonding of the sensor wafer and SOI cap wafer for the wafer-level vacuum packing. Using the anodic bonding process, the sensor wafer is hermetically sealed. In this bonding method, the silicon device layer of the SOI cap wafer and the glass side of the sensor wafer are bonded at elevated temperature exceeding 360°C. The detailed information about the anodic bonding technique can be found in [60]. Figure 3.2 shows the fabrication process for the wafer-level hermetic packaging of the accelerometer sensor wafer with the SOI cap wafer.



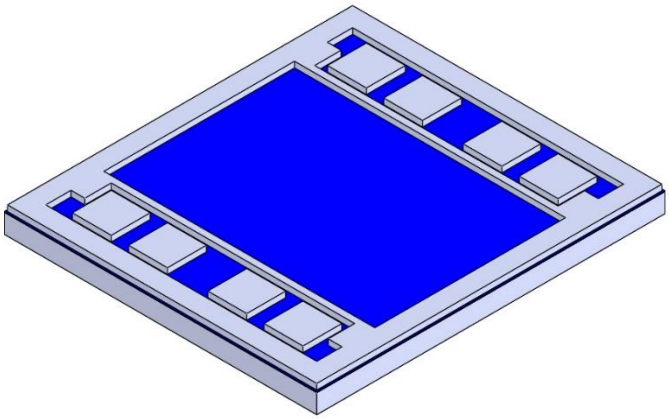
(a) Blank SOI wafer



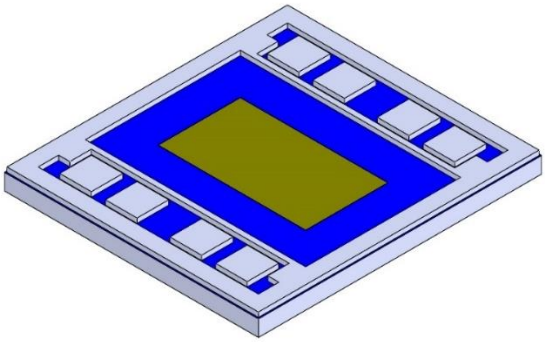
(b) Via openings on the handle layer



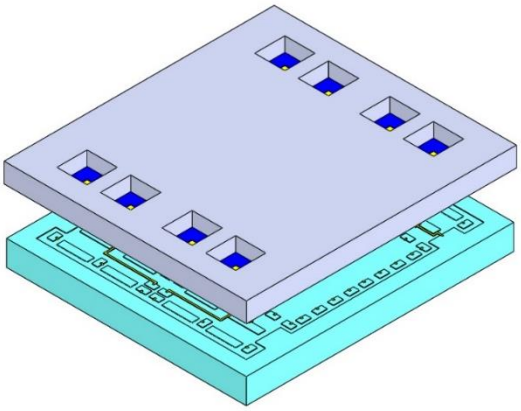
(c) Wire bonding pads



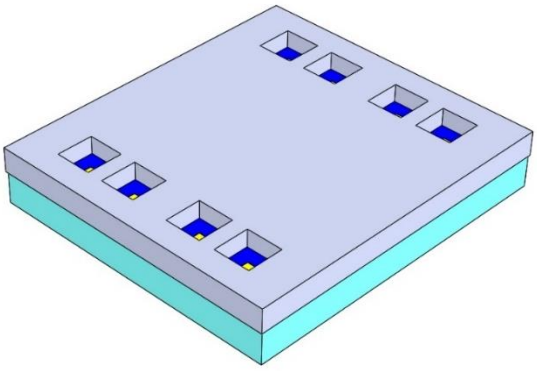
(d) Vertical feedthroughs and sealing walls on the device layer



(e) Deposition of getter



(f) Anodic bonding of sensor wafer and SOI cap wafer



(g) Wafer-level vacuum-packaged sensor wafer

Figure 3.2: Fabrication process for wafer-level hermetic packaging of the sensor wafer with the SOI cap wafer.

3.2 Fabrication Results

This section presents the fabrication results of the silicon resonant accelerometers and mentions the problems encountered during the fabrication. This study has started with the fabrication of SRA Design-1 and SRA Design-2. These two different sensor structures were fabricated on the same wafer. However, after the fabrication of these types of accelerometers, the stress-related problems on the structure led to the development of a sensor design with a single anchor structure, i.e., SRA Design-3. Figure 3.3 depicts the SEM images of the SRA Design-1 after fabrication. In SRA Design-1, the microlevers are not employed, and the proof mass is connected to the stationary outer frame.

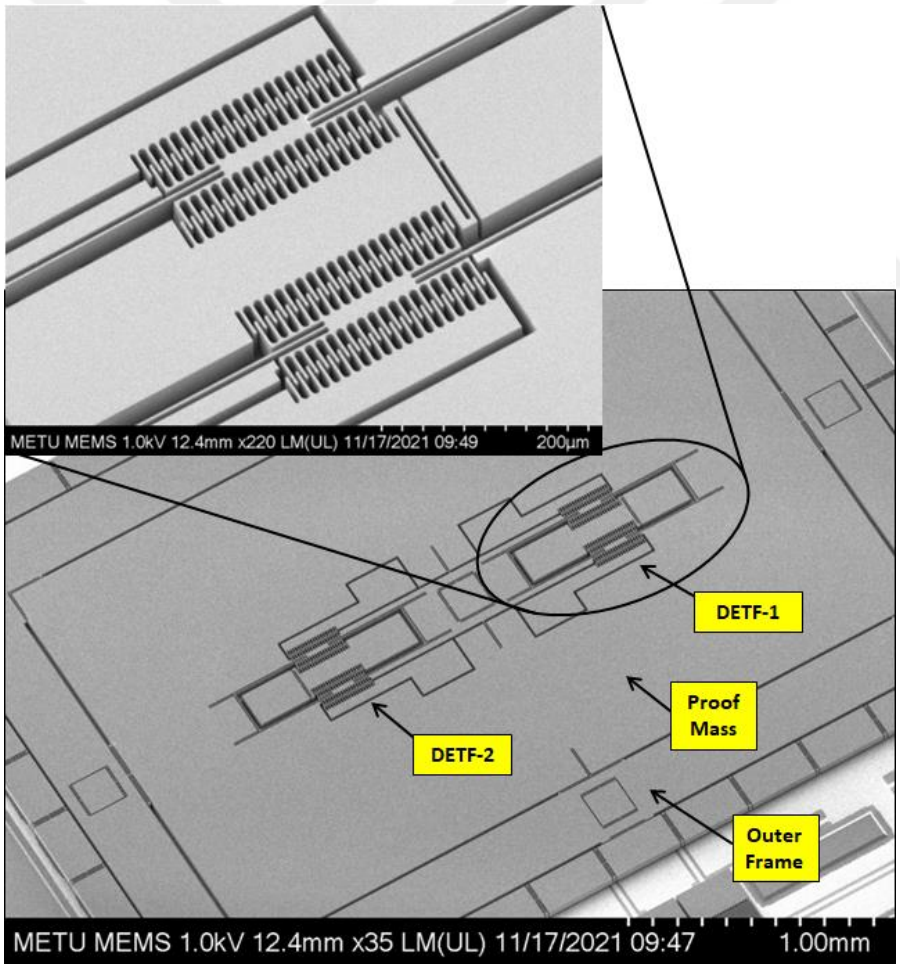


Figure 3.3: SEM pictures of the first silicon resonant accelerometer design, i.e., SRA-Design-1, fabricated using aMEMS1 process.

Figure 3.4 depicts the SEM images of the SRA Design-2 after fabrication. In the SRA Design-2, the microlevers are connected between the proof mass and the sensitive end of the DETF resonator. The proof mass is connected to the stationary outer frame.

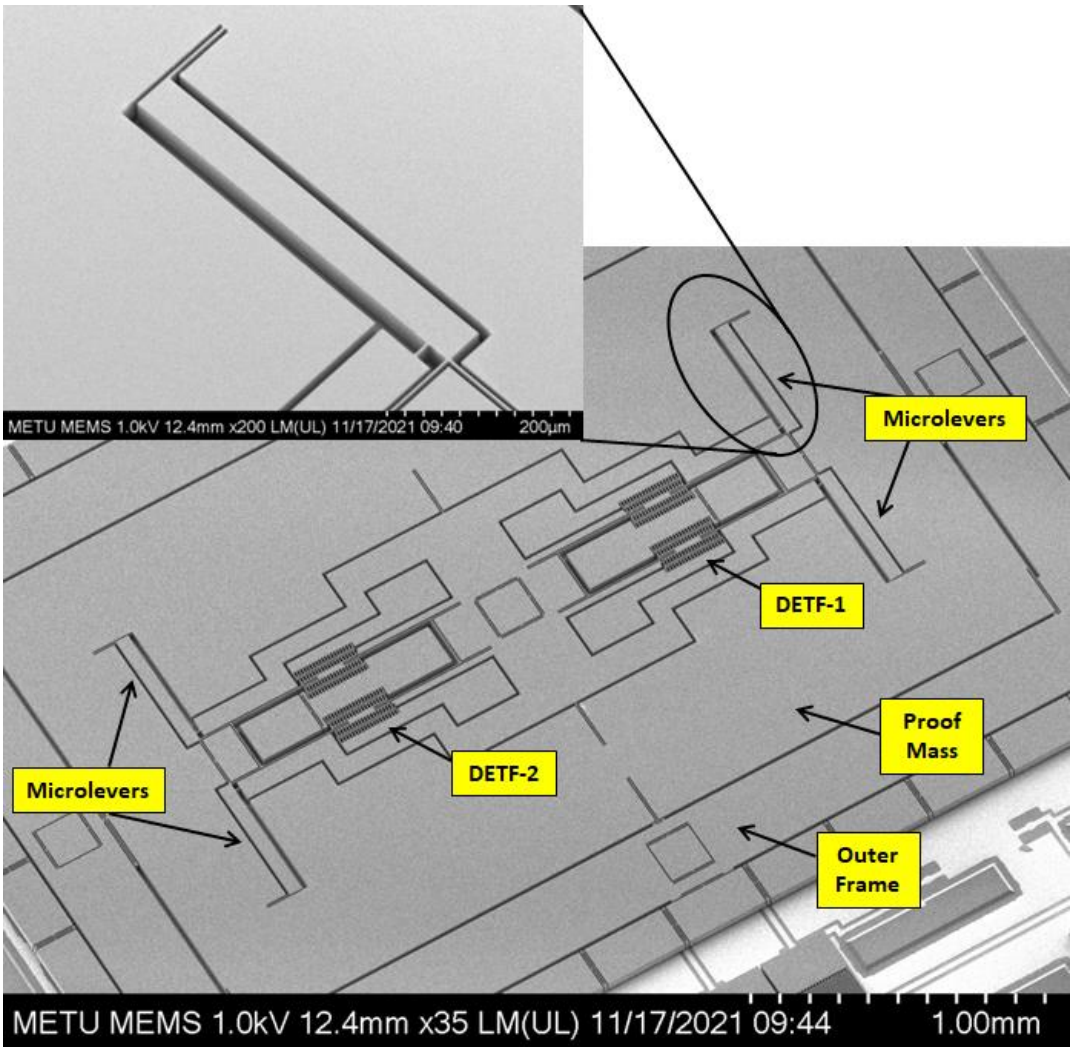


Figure 3.4: SEM pictures of the second silicon resonant accelerometer design, i.e., SRA-Design-2, fabricated using aMEMS1 process.

After the fabrication of the sensor wafer for SRA Design-1 and SRA Design-2, a deflection or crack on the springs connecting the proof mass to the stationary outer frame was observed in the microscope view. Figure 3.5 shows a close view of the broken and deflected springs on the sensor structure. The reason for this problem is that the stationary outer frame causes a stress on the proof mass after anodic bonding, which affects the mechanical stability of DETF flexures.

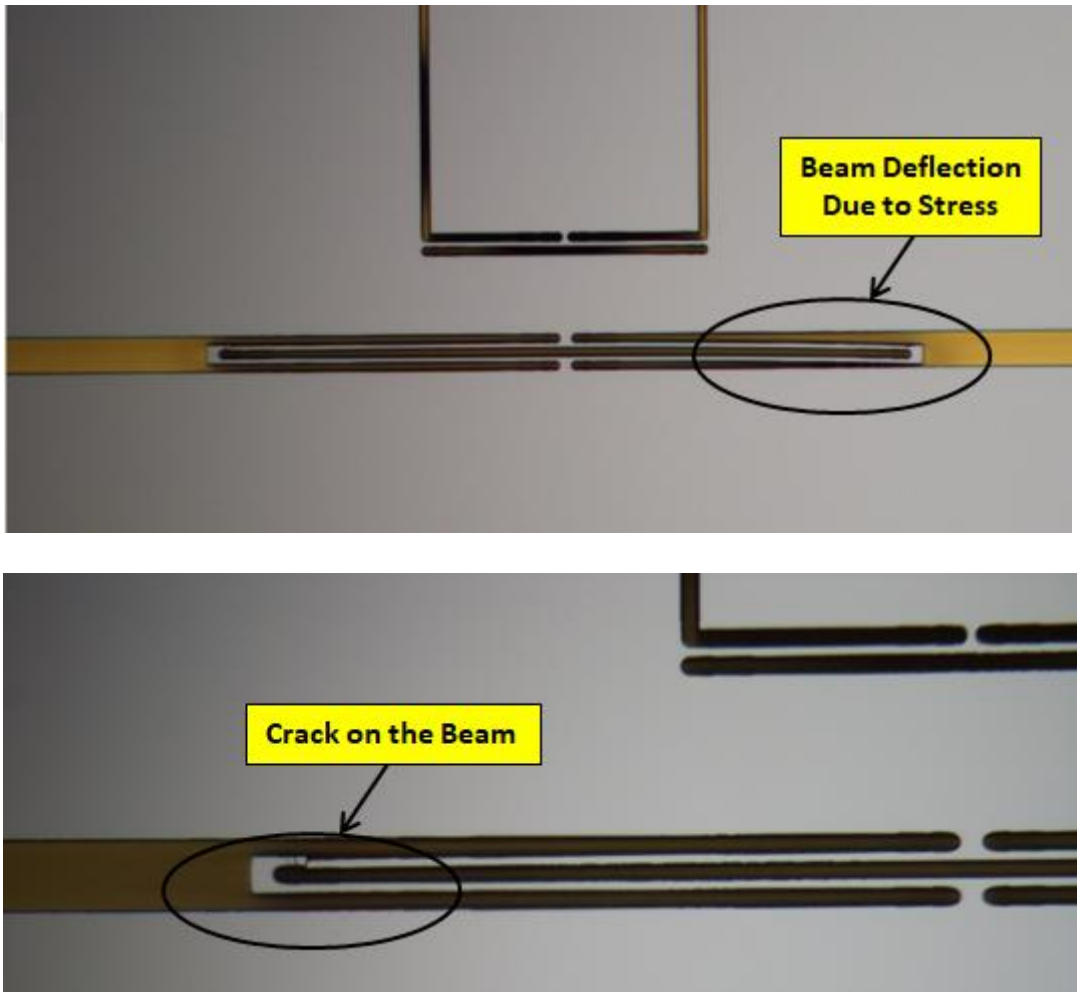


Figure 3.5: Deflection and crack on the springs connecting the proof mass to the outer frame.

To overcome the problems in SRA Design-1 and SRA Design-2, a single anchor sensor structure was designed, in which the proof mass is connected to only one anchor located in the middle of the structure. Figure 3.6 shows the SEM images of the SRA Design-3, which the proof mass is connected to a single anchor.

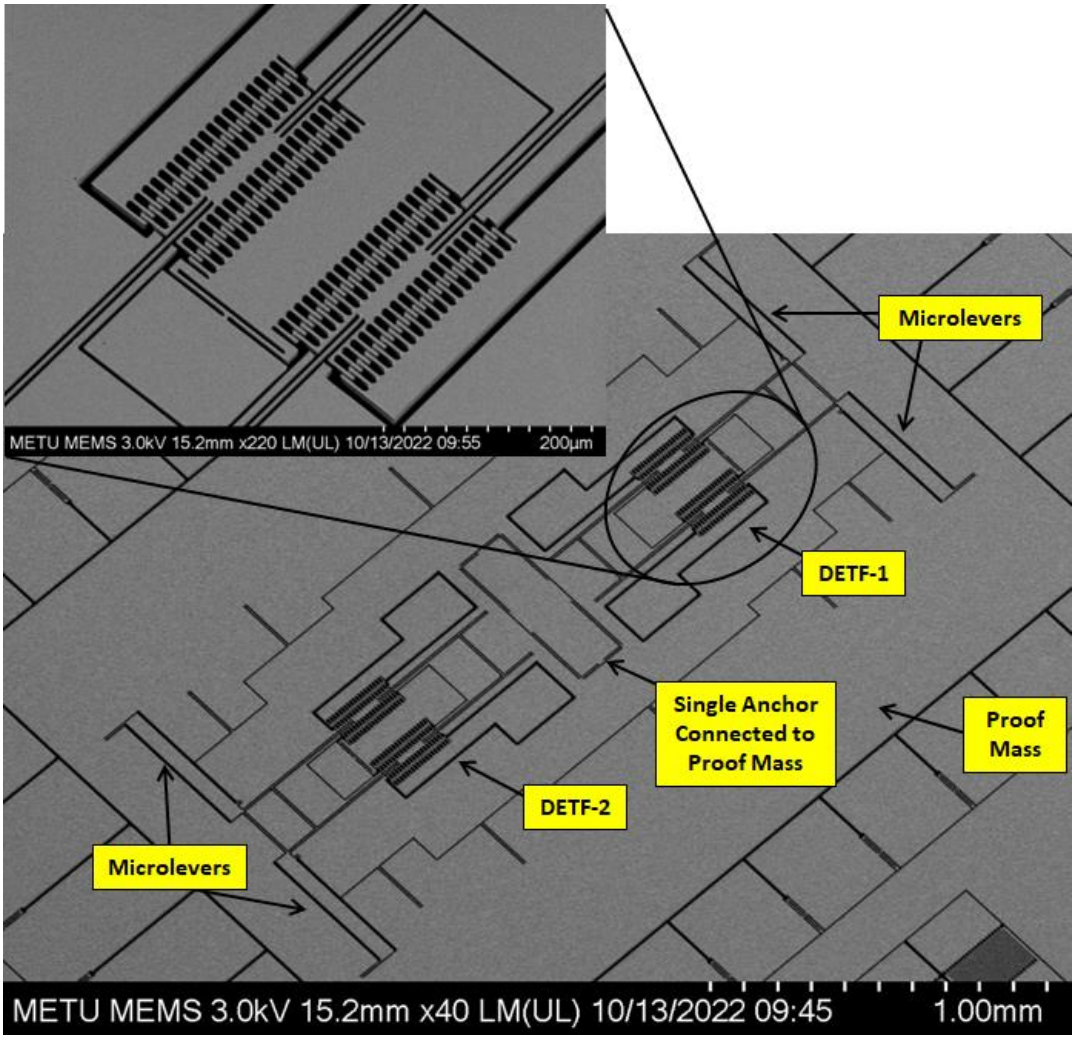


Figure 3.6: SEM pictures of the third silicon resonant accelerometer design, i.e., SRA-Design-3, fabricated using aMEMS1 process.

Fabrication errors are inevitable during the manufacturing of the silicon resonant accelerometers. The most critical fabrication flaw is the reduction in the critical structure size. The errors coming from the lithography process and undercut in the DRIE process of the structural mask create a reduction in the widths of the electrodes and flexures. The mechanical resonance frequencies of the DETF resonators are immediately affected by a change in the spring dimensions. Figure 3.7 displays SEM images of the comb fingers and DETF flexure after fabrication.

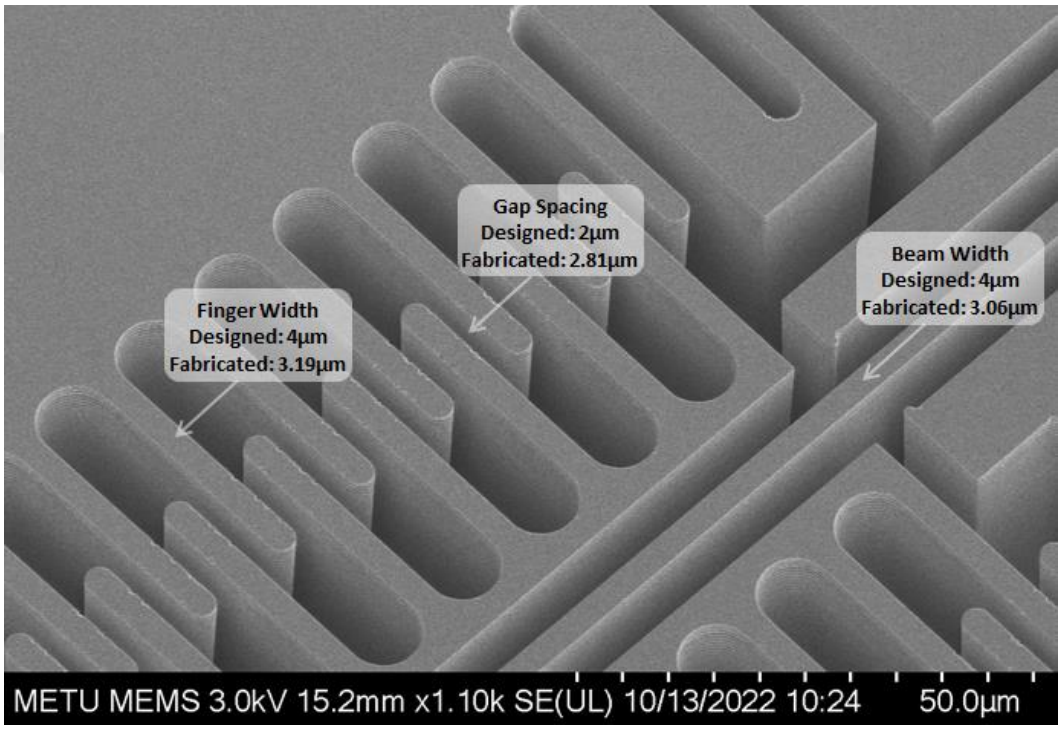


Figure 3.7: SEM picture of comb fingers and DETF flexure after the fabrication.

Figure 3.8 shows the top and bottom side pictures of the fabricated silicon resonant accelerometer using the aMEMS1 process. The die size of the fabricated MEMS chip is 4.9 mm x 5.5 mm.

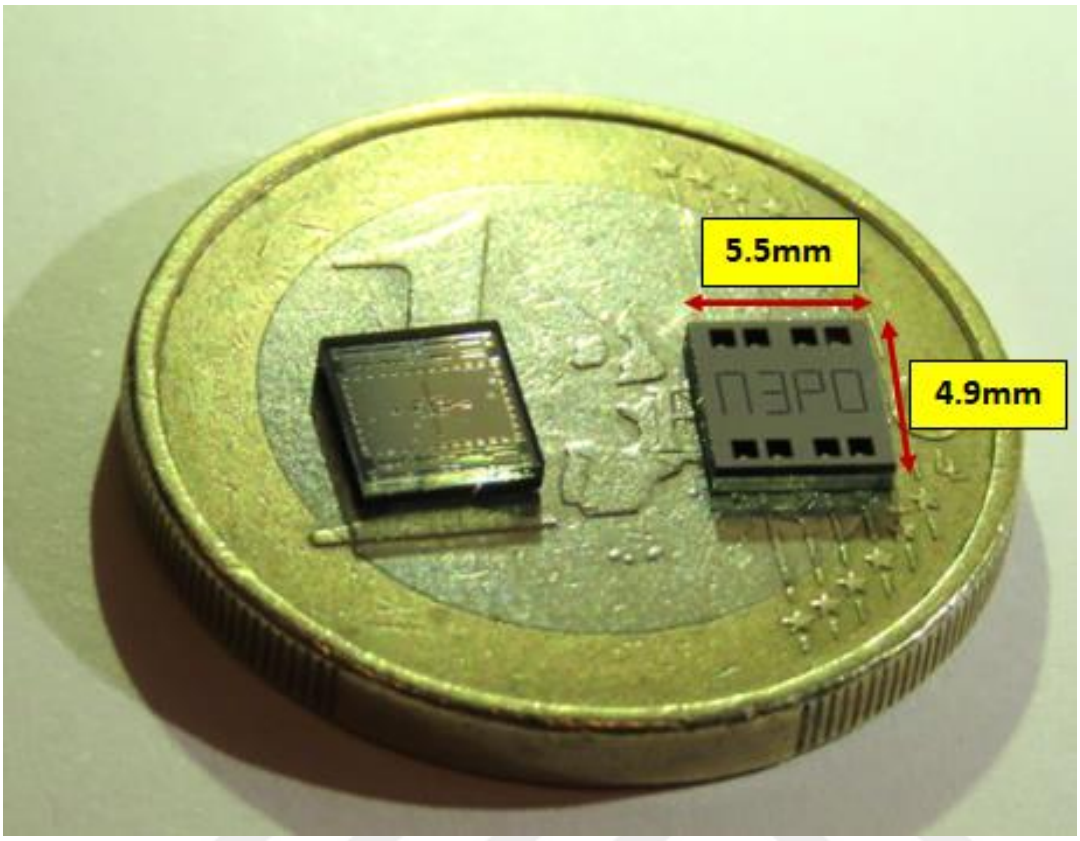


Figure 3.8: Top and bottom side pictures of the fabricated silicon resonant accelerometer using aMEMS1 process.

3.3 Summary

This chapter gives a brief overview of the steps for fabricating the silicon resonant accelerometers using the aMEMS1 process. Next, the fabrication results of the designed sensors are presented. The problems that happened while manufacturing the sensor were mentioned, and the imperfections on the critical sensor dimensions are shown.

CHAPTER 4

CONTROL ELECTRONICS FOR SILICON RESONANT ACCELEROMETERS

This chapter presents the details of the frequency read-out electronics for the silicon resonant accelerometers studied in this thesis. Section 4.1 introduces the general block diagram of the DSP-based frequency readout circuit implemented using the Zurich Instrument HF-2 lock-in amplifier. Section 4.2 explains the details of the analog front-end electronics. Section 4.3 gives information about the digital signal processor-based phase-locked-loop circuit. Section 4.4 explains the design of automatic gain control circuit. Section 4.5 briefly summarizes this chapter.

4.1 General Block Diagram of Control Electronics for Silicon Resonant Accelerometer

The silicon resonant accelerometer consists of two DETF resonators, and the output of the sensor is the frequency difference of these two oscillators. The control electronics of the silicon resonant accelerometer are built on a digital signal processor (DSP)-based phase-locked-loop (PLL) system implemented on a Zurich Instrument HF-2 lock-in amplifier [61]. Figure 4.1 depicts the general block diagram of the control electronics for the silicon resonant accelerometer in this study. The control electronics of the DETF resonator include three major blocks: front-end electronics, phase-locked-loop (PLL), and automatic gain control loop (AGC). The front-end electronics converts the output current of the DETF resonator to voltage, and amplifies with a preamplifier and gain stage. PLL is employed to maintain the oscillation of DETF resonator at resonance. Automatic gain control loop keep

constant the oscillation amplitudes of the resonators. Each DETF resonator has its own PLL and AGC blocks, which operate independently of one another.

The speed of PLL is characterized by the bandwidth of the closed-loop system. There is a trade-off between the PLL speed and phase noise. The amplitude gain control loop determines the oscillation displacement of the DETF resonators. The details of the system blocks of the control system for the silicon resonant accelerometer are given in the following sections.

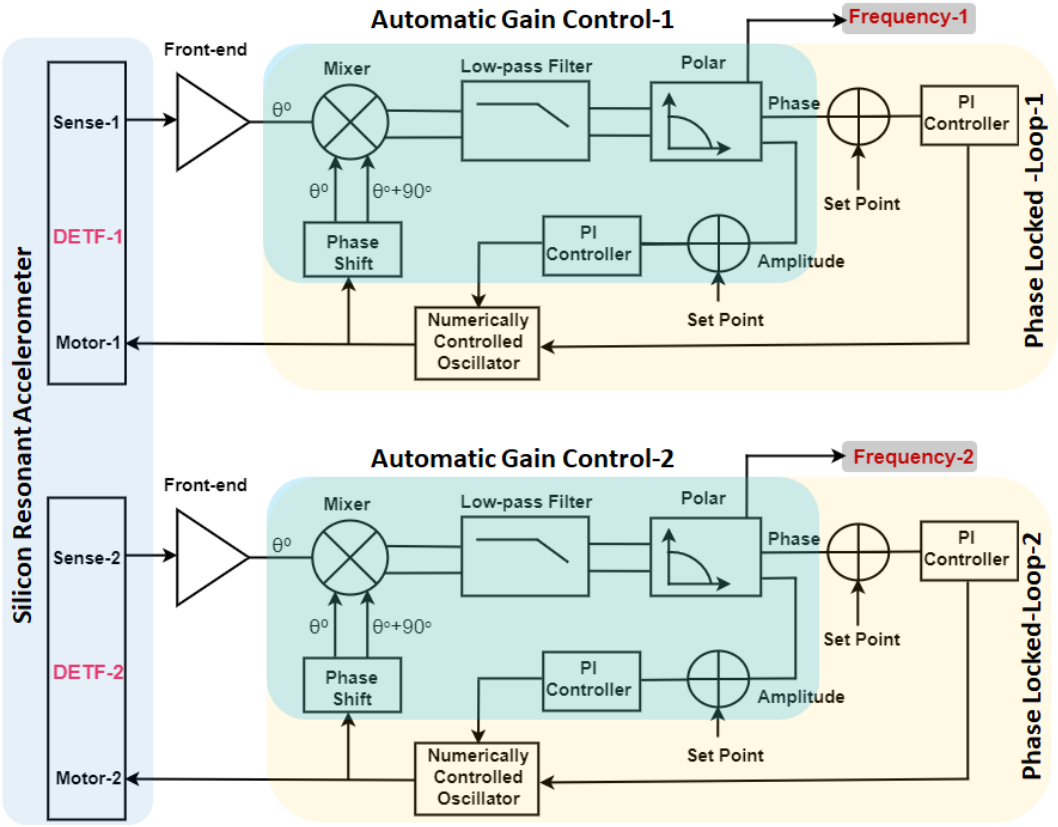


Figure 4.1: Block diagram of the control electronics for the silicon resonant accelerometer implemented on the lock-in amplifier.

4.2 Analog Front-End Electronics

The front-end electronics consist of a preamplifier and gain stage. This block transforms the output current of the DETF resonator to a voltage, then amplifies to the required signal level. The outputs of the front-end electronics are fed to the inputs of the lock-in amplifier. Figure 4.2 depicts the schematic of the front-end electronics for the silicon resonant accelerometer. A transimpedance amplifier is employed in the preamplifier stage due to its low input impedance, which reduces signal degradation during the transformation of current to voltage. In addition, it is immune to parasitic capacitances and contact resistance. Referring to Figure 4.2, the relation between the input-output voltage of this amplifier is represented in the following form:

$$\left|\frac{V_{out1}(s)}{I_{out}(s)}\right| = Z_{pre} = \frac{R_{preamp}}{1 + sC_{preamp}R_{preamp}} \qquad 4.1$$

Whether the transimpedance amplifier is resistive or capacitive depends on the multiplication of of $sC_{preamp}R_{preamp}$ in Equation 4.1. The type of the preamplifier is capacitive if the value of $sC_{preamp}R_{preamp}$ is much greater than 1. The capacitive preamplifier is selected in the preamplifier stage of the DETF resonators due to its low-noise interface with a high gain, compensating the poor capacitive sensitivity of drive and sense electrodes. In this condition, the output voltage of the preamplifier stage is the multiplication of the resonator output current with $1/sC_{preamp}$.

The preamplifier stage is followed by an active band-pass filter to increase signal-to-noise ratio (SNR) of the input signal entering the lock-in amplifier. The cut-off frequencies of the band-pass filter are one tenth and ten times of the natural frequency of DETF resonator. The gain of the filter is adjusted to a level considering the maximum input voltage range of the lock-in amplifier. The gain, low and high cut-off frequencies of the low-pass filter can be expressed in terms of the circuit components as follows:

$$A_{BPF} = \left|\frac{V_{out2}}{V_{out1}}\right| = -\frac{R_2}{R_1} \quad 4.2$$

$$f_{high} = \frac{1}{2\pi R_1 C_1} \quad 4.3$$

$$f_{low} = \frac{1}{2\pi R_2 C_2} \quad 4.4$$

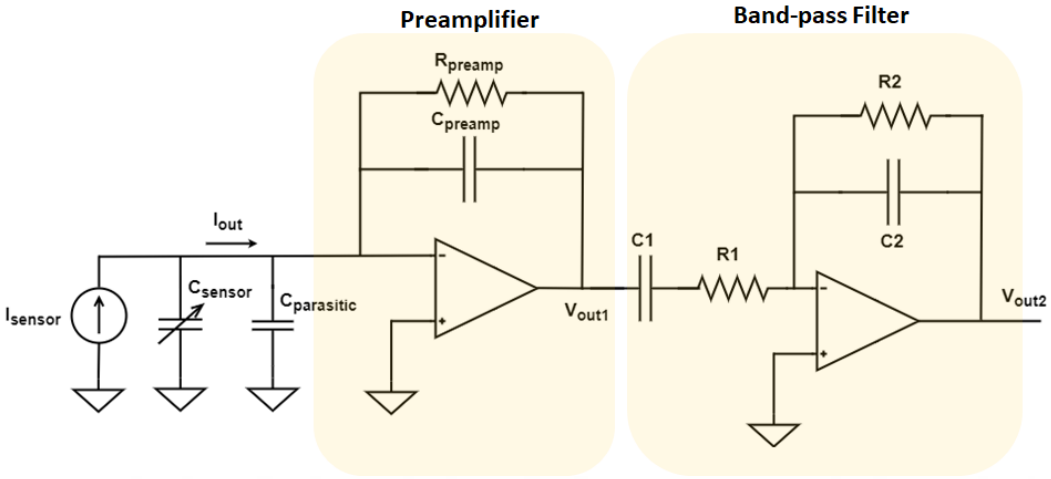


Figure 4.2: Schematic of the front-end circuit.

4.3 Phase-Locked Loop

A phase-locked loop, or PLL, is a closed control system with negative feedback that generates an output signal having a well-defined phase relationship with the input signal. The input and output signal are synchronized as a result of phase-locking. The PLL is the key element of the frequency readout circuit of the silicon resonant accelerometer. The oscillations of the DETF resonators are maintained by the PLL system. A basic PLL system includes three major blocks: a phase detector, a PI controller, and a numerically controlled oscillator (NCO). Figure 4.3 depicts the

block diagram of the PLL implemented on the Zurich Instrument HF-2 lock-in amplifier in this study.

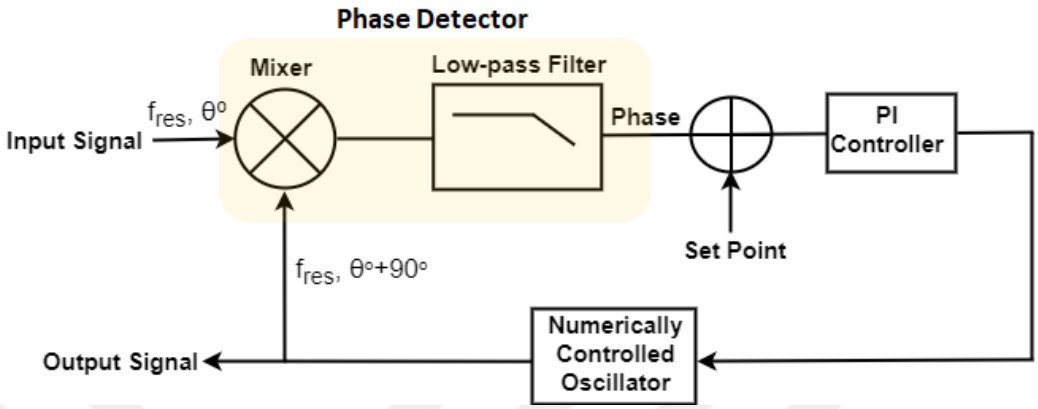


Figure 4.3: Block diagram of a PLL.

The PLL takes an input signal coming from the DETF resonators and transfer its phase information to a NCO to create an output signal following the phase of the input signal. Firstly, the amplified signal coming from the front-end stage is fed to the phase detector stage of the PLL. The phase detector detects the phase difference between the input and output. A demodulator block functions as a phase detector, consisting of a multiplier and low-pass filter. In lock-in amplifier, dual-phase detectors are employed so they can get both phase and amplitude information of the input signal, as shown in Figure 4.1. The low-pass filter suppresses the unwanted frequency components of the input signals after the demodulation improving the noise performance of the PLL system. A 4^{th} order low-pass filter with a 100Hz of cut-off frequency is implemented on the lock-in amplifier. The output of the phase detector is compared to a phase setpoint to create an error signal for the proportional-integral (PI) controller. The PI controller generates a feedback signal based on the error signal to modify the frequency of the NCO. In this manner, the controlled oscillator follows the phase of the input signal and produces a signal with the same frequency as the input reference.

The bandwidth of the closed-loop system is determined by the PLL speed. The PLL speed can be adjusted by the PI controller. The bandwidth of the PLL is also the bandwidth of the silicon resonant accelerometer system, namely how fast the frequency readout system follows the sudden frequency change. There is a trade-off between the bandwidth of the PLL and phase noise. As the bandwidth of the PLL increases, the minimum frequency resolution of the system deteriorates.

For a stable operation, the phase margin should be greater than 60° for the PLL system. The PI parameter are optimized after few iterations using the advisory section of the Zurich Instrument HF-2 lock-in amplifier. Figure 4.4 depicts the step response of the PLL controller. The rise time and settling time of the system are about 11msec and 21 msec, respectively. The bandwidth of the silicon resonant accelerometer is adjusted to be about 33 Hz in this study. The phase margin is about 85°.

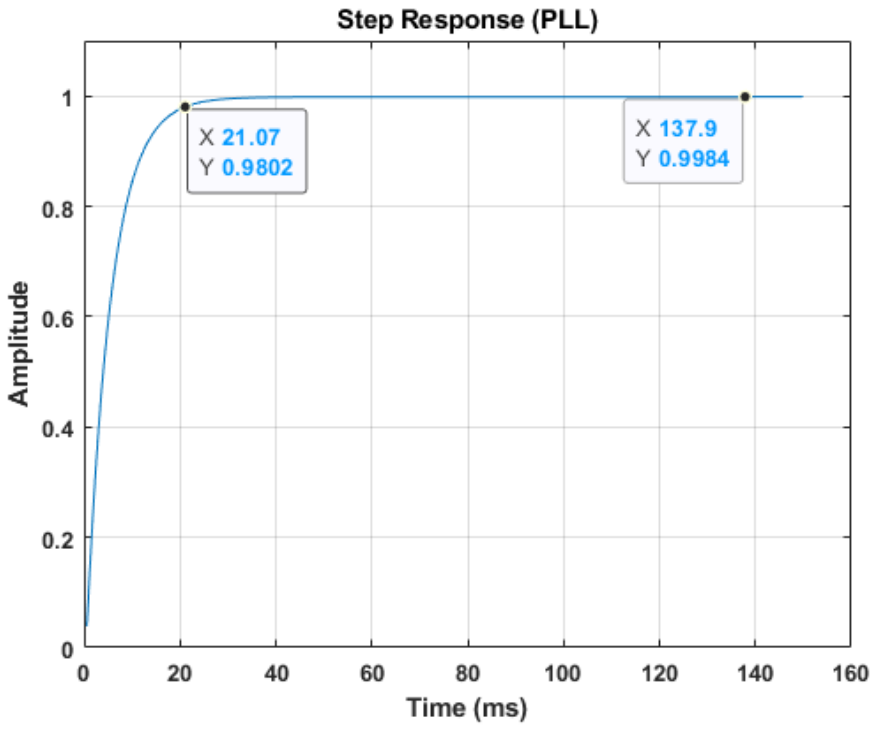


Figure 4.4: Step response of the closed-loop PLL controller.

4.4 Automatic Amplitude Control Circuit

The drive signals applied to the motor electrodes of the DETF resonators are generated by a numerically controlled oscillator in the PLL loop. However, the amplitudes of these signals should be well controlled for proper resonant accelerometer operation because they determine the oscillation displacement of the DETF resonators. The stability of resonator oscillation is critical for the short- and long-term stability of the silicon resonant accelerometer due to the stiffness nonlinearity of the DETF flexures.

The automatic gain control loop works with the PLL to make sure that the DETF resonator's excitation voltage stays the same. Figure 4.5 depicts the block diagram of the automatic gain control system implemented on the lock-in amplifier. In this system, the amplified signal coming from the front-end electronics is demodulated with the in-phase component of the oscillator signal generated by the PLL. The demodulator output is fed to a low-pass filter. The automatic gain control unit utilizes a proportional-integral (PI) controller to compare and adjust the low-pass filter output to a given setpoint. The PI controller output is multiplied by the in-phase component of the oscillator signal generated by the PLL, and it is applied to the motor electrode of the corresponding DETF resonators. Since the silicon resonant accelerometers consist of two DETF resonators, there are two AGC loops in the overall system working independently. In the remaining part of this section, the mathematical analysis and simulations are done for one DETF resonator for sake of simplicity, but the same equations are valid for the other resonator.

Some design parameters should be carefully adjusted for a stable closed-loop operation of the automatic gain control system. Settling time, phase margin, and overshoot are some of these parameters. The settling time can be defined as the response time of the closed-loop system. The amplitude of the oscillation remains constant throughout the sensor's operation time, indicating that there is no known disturbance to the control system. Thus, the settling time, or the closed loop bandwidth, of the automatic gain control system just affects the start-up time of the

accelerometer. The phase margin of the closed-loop control system should be greater than 60°. Moreover, the overshoot at the controller output should be avoided in order not to damage the thin and long flexures of the DETF resonators.

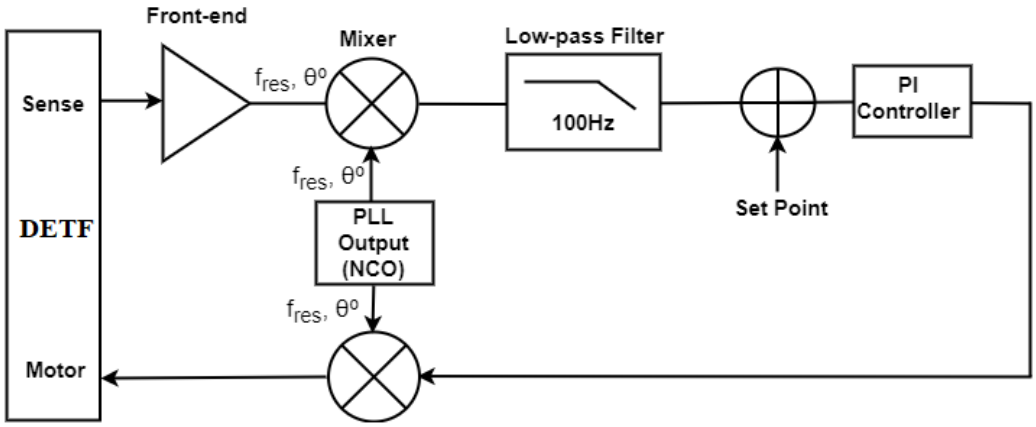


Figure 4.5: Block diagram of the closed-loop automatic gain control unit.

The open loop behavior of the system should be examined by resonance experiments before building the closed-loop automated gain controller to get sensor characteristics such as the natural frequency, gain, and quality factor. The resonance test determines the transfer function of the MEMS resonator with the front-end electronics. Figure 4.6 depicts the block diagram of the signal conversions occurring throughout the resonance test. Firstly, the actuation voltage applied to the motor electrode causes an actuation force. The actuation force leads to the displacement of the proof mass. The displacement of the proof mass results in the generation of current in the sense electrodes. The preamplifier converts the sensor output current to voltage.

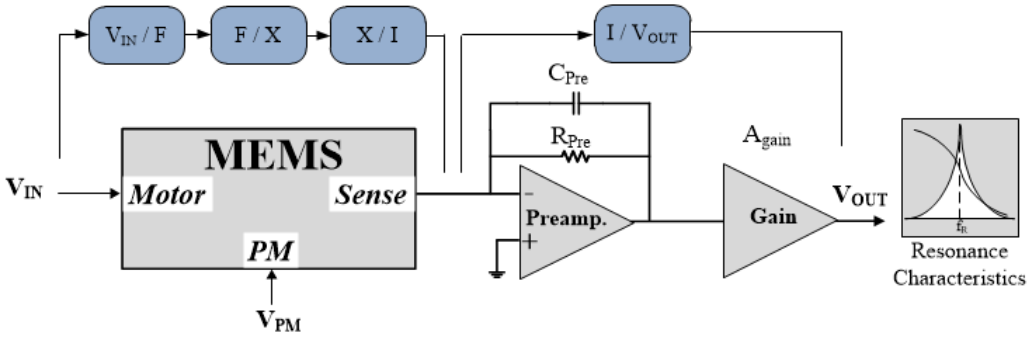


Figure 4.6: Schematic of signal conversions during the resonance test of DETF resonator of the silicon resonant accelerometer.

The open loop transfer function of the DETF resonator can be written in terms of the sensor parameters as follows:

$$\frac{V_{out}(s)}{V_{in}(s)} = V_{PM}\frac{\partial C_M}{\partial x}\frac{1/m_r}{\left(s^2 + \frac{w_r}{Q_r}s + w_r^2\right)}V_{PM}\frac{\partial C_s}{\partial x}sZ_{pre}A_{gain} \qquad 4.5$$

where $\frac{\partial C_M}{\partial x}$ is the capacitive sensitivity of the resonator motor electrodes, $\frac{\partial C_M}{\partial x}$ is the capacitive sensitivity of the resonator sense electrodes, V_{PM} is the proof mass, m_r is the mass of the resonator, w_r is the resonance frequency, Q_r is the quality factor, Z_{pre} is the preamplifier gain, and the A_{gain} is the amplification factor of the gain stage. In Equation 4.5, the gain of the preamplifier stage, the proof mass voltage, and the resonator mass can be found from the design. The resonance frequency and quality factor of the sensor are determined by the resonance test. Since the motor and sense electrodes are identical, their capacitive sensitivities can be calculated using Equation 4.5 and the gain value obtained by the resonance test.

In the closed-loop system, there is a direct relation between the amplitude of the front-end output signal and resonator displacement as follows:

$$V_{OUT}(s) = V_{PM}\frac{\partial C_s}{\partial x} sXZ_{pre}A_{gain} \qquad 4.6$$

The signal amplitude of the front-end output is adjusted according to the fixed voltage applied to the low-pass filter output. The amplitude of this signal defines the oscillation displacement of the DETF resonator. The open loop behavior of the automatic gain control loop should be analyzed to examine the settling time, phase margin, and overshoot using the actual sensor and controller values. Table 4.1 shows the sensor parameters for one of the DETF resonators of the accelerometer Acce#4 (details in Chapter 5), which were found through resonance tests and sensor design. The oscillation displacements of the DETF resonators are adjusted to be 0.25μm, at which the resonators give a linear response without stiffness nonlinearity in the resonance tests.

Table 4.1: Sensor and circuit parameters used for the design of automatic gain control loop of the accelerometer Acce#4 for 10V proof mass voltage (for one resonator).

Parameter	**Value**
Resonance Frequency (f_r)	16480Hz
Resonance Gain (A_r)	60.3dB
Quality Factor (Q)	45370
Target Oscillation Displacement (X)	0.25μm
Voltage Amplitude (V_{out}) for Target Oscillation	800mV

For a stable operation, the phase margin should be greater than 60° for the automatic gain control system. The PI parameter are optimized after few iterations using the

advisory section of the Zurich Instrument HF-2 lock-in amplifier for the sensor parameters shown in Table 4.1. Figure 4.7 shows the step response of the system. The settling time for this the system is calculated to be 22 milliseconds by the simulation. The phase margin of the system is about 75°, and the bandwidth of closed loop system is about 30 Hz.

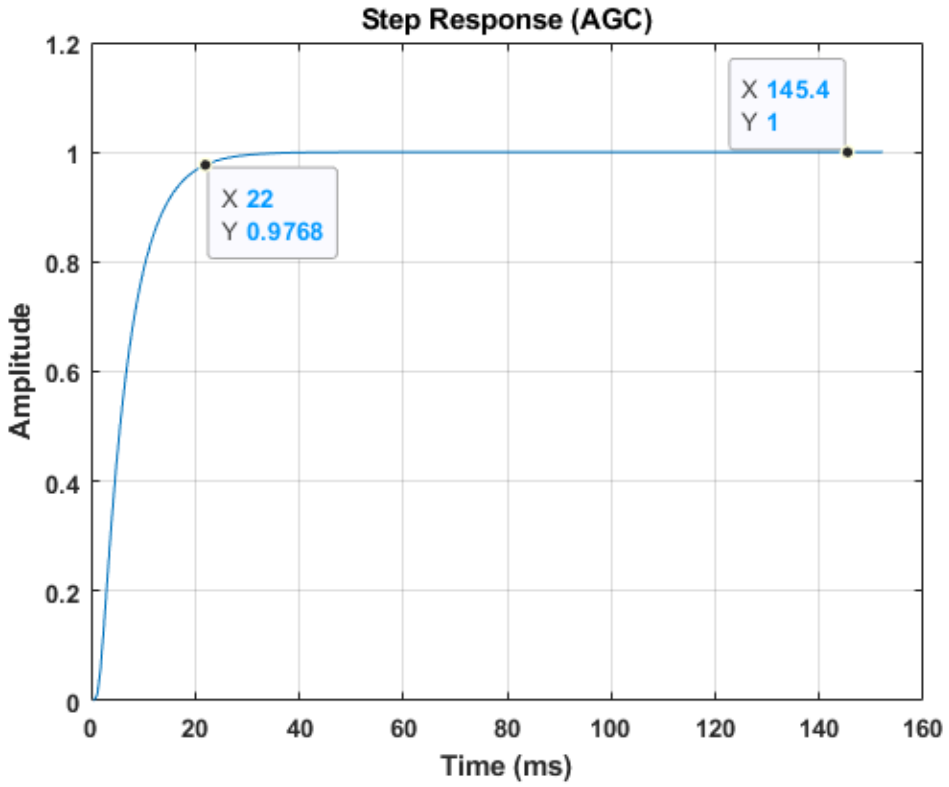


Figure 4.7: Step response of the closed-loop automatic controller.

The transient response of the closed-loop automatic gain control system is analyzed constructing a MATLAB SIMULINK model with measured sensor parameters. Figure 4.7Figure 4.8 depicts the SIMULINK model of the automatic gain control system of the DETF resonator. Figure 4.9 shows the transient behavior of the front-end output and displacement signals of the DETF resonator in SIMULINK model.

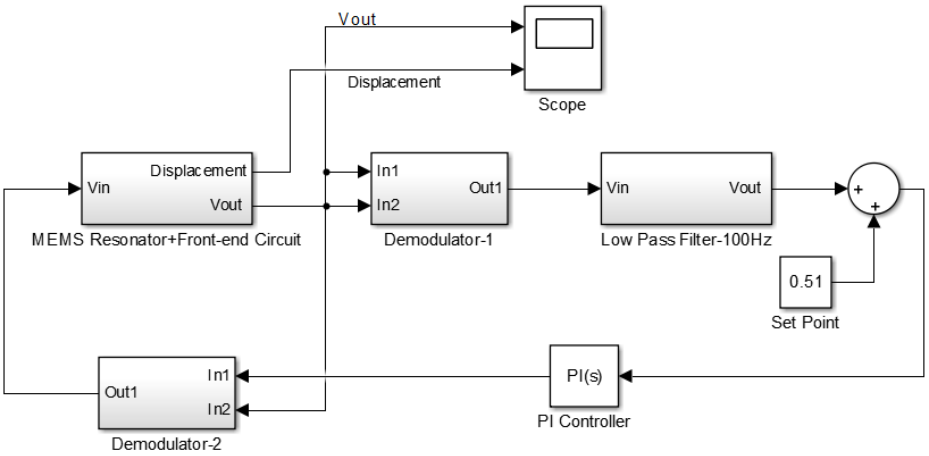


Figure 4.8: SIMULINK model for the automatic gain control system of the DETF resonator.

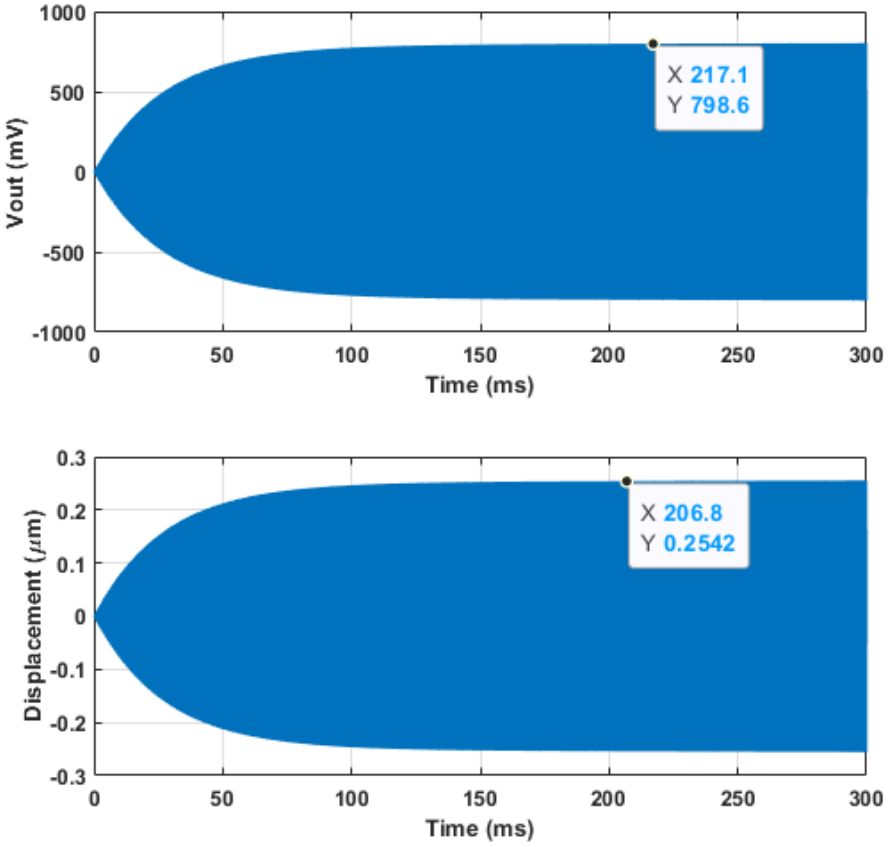


Figure 4.9: Front-end output and displacement signals of the simulated DETF resonator.

4.5 Summary

This chapter gave the details of the frequency readout electronics for the silicon resonant accelerometers studied in this thesis. The control electronics of the silicon resonant accelerometer consisted of three major blocks: analog front-end electronics, phase-locked loops, and automatic gain controllers. The analog front-end circuit converts the sensor current to voltage and amplifies it. The phase locked-loop maintains the oscillation of the DETF resonators. The automatic gain control loop adjusts the oscillation displacement to a desired level. A SIMULINK model for the automatic gain control system was designed using real sensor parameters to simulate the transient behavior of the sensor voltage and displacement signals with optimized controller parameters.

CHAPTER 5

TEST RESULTS

This section provides the test results of the silicon resonant accelerometers. The frequency outputs of the silicon resonant accelerometers were acquired by implementing the readout circuit on the Zurich Instrument HF2 lock-in amplifier throughout the characterization, performance, and temperature tests. Table 5.1 shows the list of the silicon resonant accelerometer sensors tested in this thesis work. The test results of the silicon resonant accelerometers are compared with one of the commercial capacitive MEMS accelerometers developed by Mikrosistemler. Section 5.1 gives the resonance characterization results of the studied sensors. Section 5.2 presents the 4-point tumble test results for scale factor measurements of the resonant accelerometers. Section 5.3 provides the temperature test results for the corresponding sensors. Section 5.4 demonstrates the Allan variance, bias stability and repeatability test results of the studied accelerometers. Section 5.5 gives the summary of the chapter.

Table 5.1 List of the silicon resonant accelerometer sensors tested in this study.

Sensor No	**Sensor Design**	**Microlever**	**Proof Mass Connection**
Acce#1	SRA Design-1	No	Stationary frame
Acce#2	SRA Design-2	Yes	Stationary frame
Acce#3	SRA Design-3	Yes	Single anchor
Acce#4	SRA Design-3	Yes	Single anchor

5.1 Resonance Characterization of the Silicon Resonant Accelerometers

After the fabrication of the silicon resonant accelerometer, the die-level chip tests were done using the probe station and lock-in amplifier before integrating the sensor chips to the sensor module, including the preamplifier op-amp. Figure 5.1 demonstrates the die-level resonance test setup of the accelerometer chips. The connection to the pads of the sensor chip is achieved by the special probes, as shown in Figure 5.1. Since the silicon resonant accelerometer consists of two DETF resonators, the functionality of these resonators was checked through the resonance test. In the resonance test, the motor electrode of each resonator is exposed to an AC voltage from the output of the lock-in amplifier. The resonator output is current in response to the applied AC voltage, and this current is transferred to voltage using a preamplifier circuit and fed back to the input of the lock-in amplifier. The oscillator frequency is swept, and the gain and phase characteristics of the corresponding resonator are obtained.

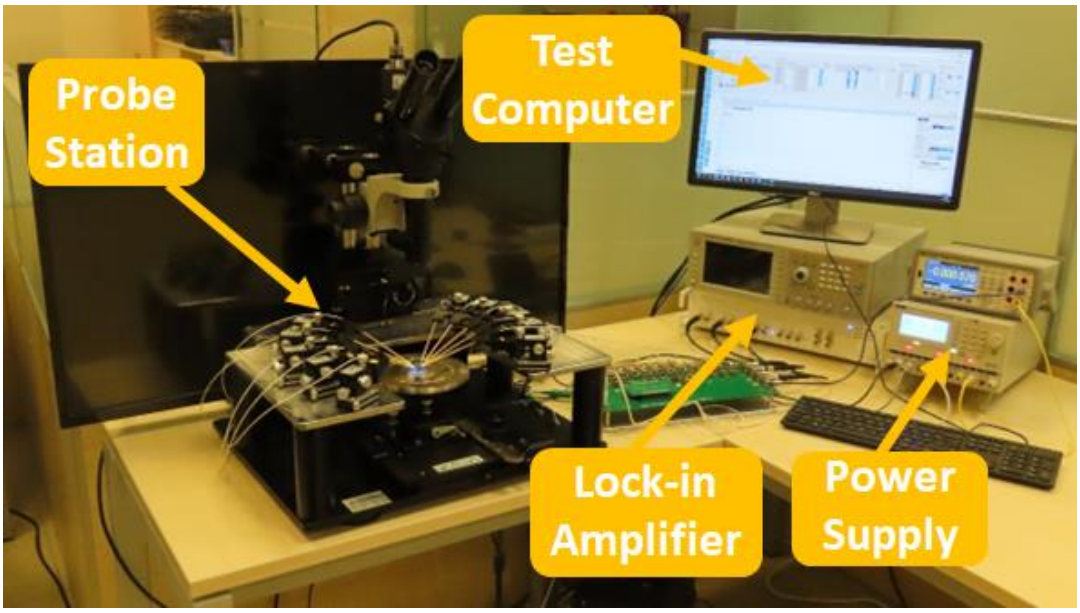
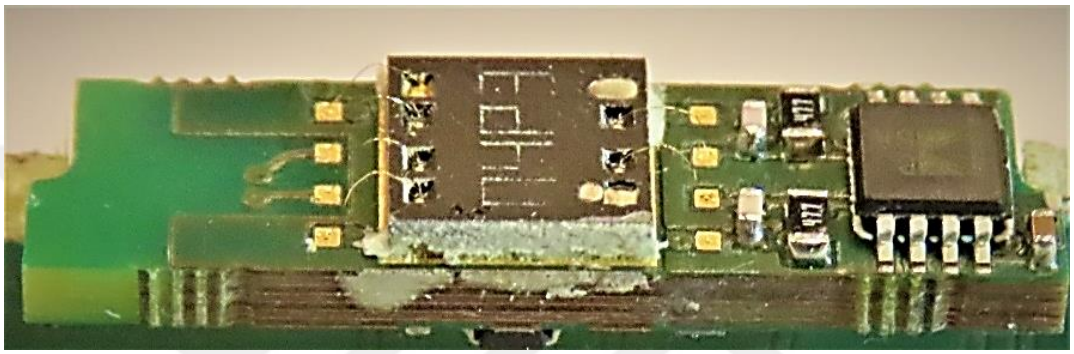
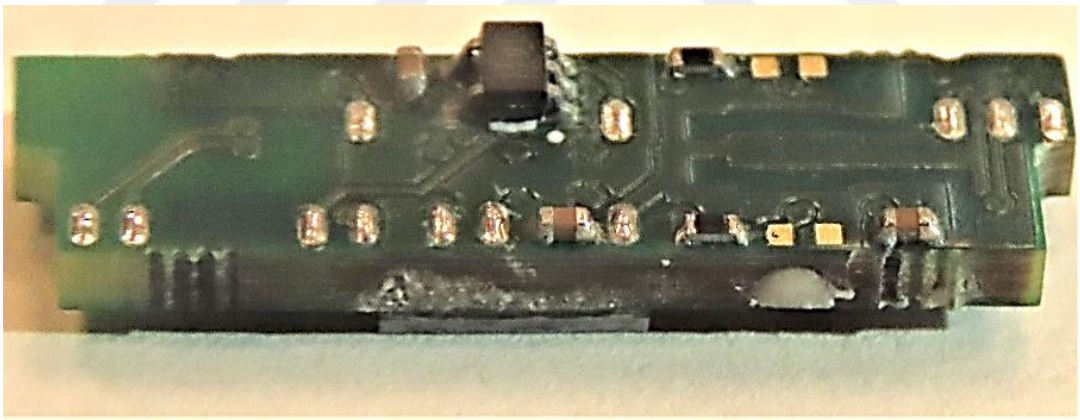


Figure 5.1: Die-level resonance test setup of the fabricated silicon resonant accelerometer.

After the chip-level resonance tests, the functional silicon resonant accelerometer chips are integrated into the sensor module, including the preamplifier circuit and temperature sensor. Figure 5.2 shows a silicon resonant accelerometer connected to the preamplifier circuit on the sensor module.



(a)



(b)

Figure 5.2: Silicon resonant accelerometer integrated to the front-end electronics: (a) top and (b) bottom view.

After integrating the sensor chips into the sensor module, the resonance tests were repeated to extract information about the resonance frequency, gain, and quality factors using the lock-in amplifier. These parameters are needed for optimizing the controller parameters of the self-oscillation circuit of the DETF resonators. Table 5.2 demonstrates the resonance test results of the DEFT resonators of the silicon resonant accelerometer with the front-end electronics.

Table 5.2 Resonance characteristics of the DETF resonators of the silicon resonant accelerometers.

Sensor No	Resonator	Proof Mass Voltage (V)	Frequency (Hz)	Gain (dB)	Quality Factor
Acce#1	R1	10V	20344.6	54.9	45664
(SRA Design-1)	R2	10V	20525.8	55.8	58930
Acce#2	R1	10V	20689.5	55.7	48126
(SRA Design-2)	R2	10V	20772.4	55.9	44256
Acce#3	R1	10V	16964.9	62.2	48346
(SRA Design-3)	R2	10V	16986.9	60.3	45373
Acce#4	R1	10V	16763.8	76.5	50366
(SRA Design-3)	R2	10V	16480.4	60.3	45373

In the next step, the resonators of the tested silicon resonant accelerometers were characterized at different proof mass voltages. Figure 5.3 and Figure 5.4 show the resonance characteristics of the DETF resonators of the accelerometer Acce#4 for different proof mass voltages. As the proof mass voltages rise, the gain of the sensor increases in a manner proportional to the square of the proof mass voltage, as expected.

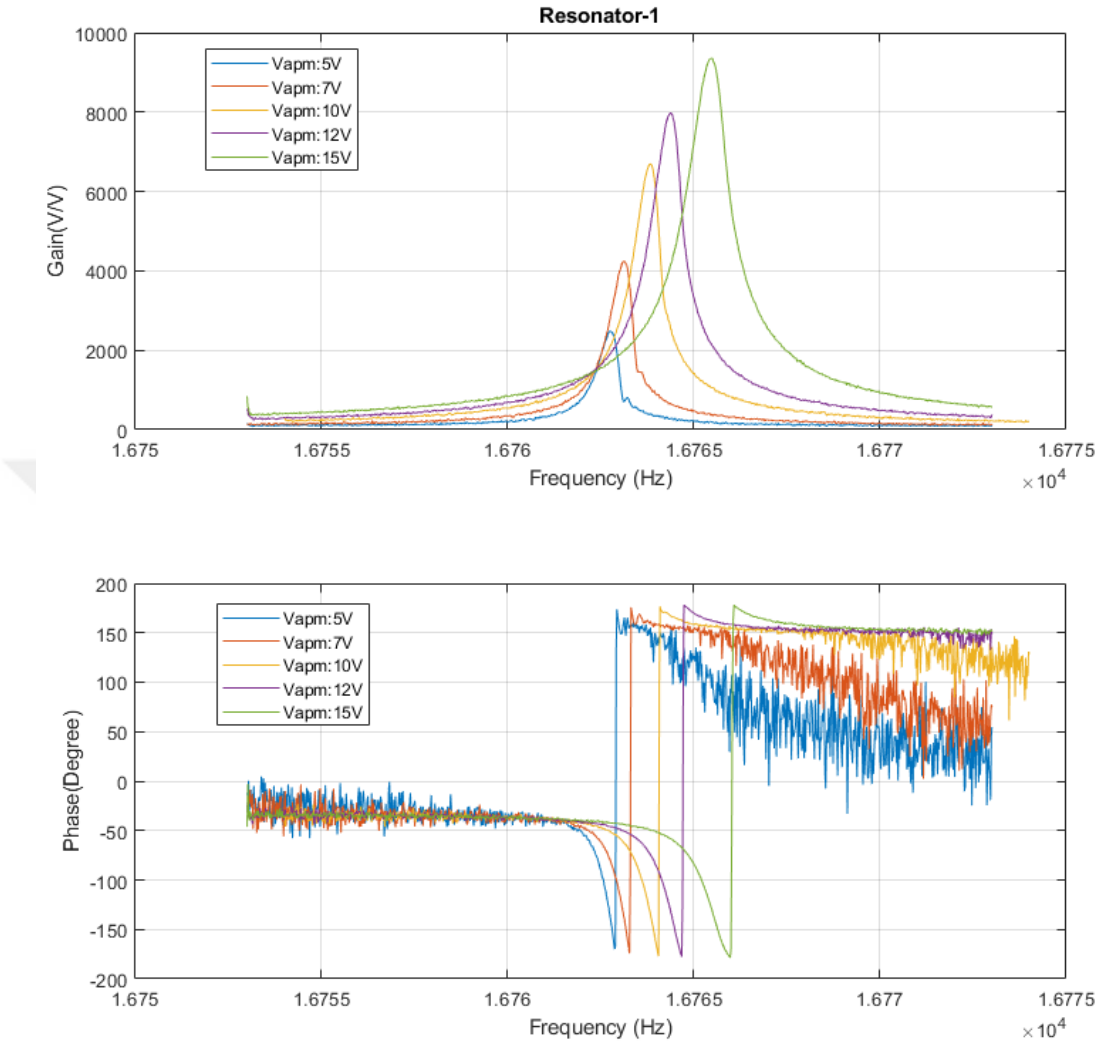


Figure 5.3: Resonance characteristics of the DETF Resonator-1 of the accelerometer Acce#4 for different proof mass voltages.

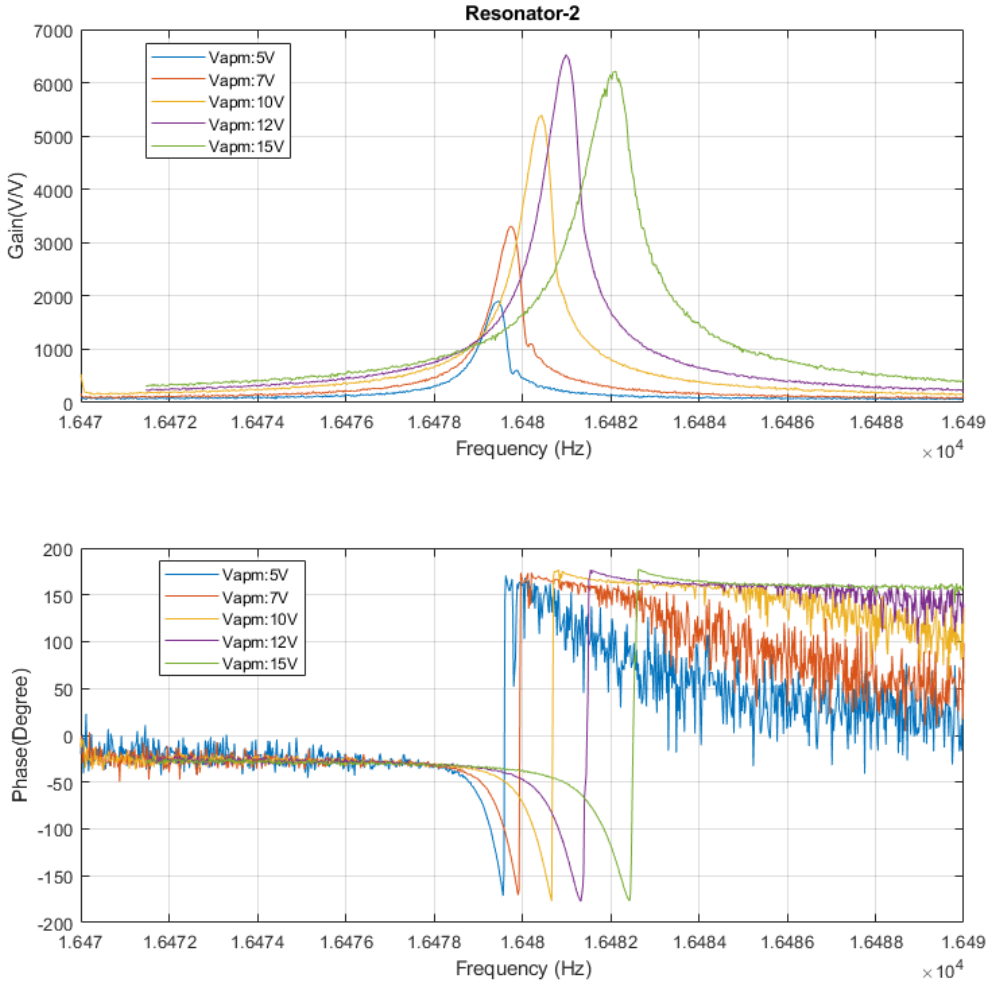


Figure 5.4: Resonance characteristics of the DETF Resonator-2 of the accelerometer Acce#4 for different proof mass voltages.

5.2 Test Set-up for the System Level Tests of the Silicon Resonant Accelerometers

After the resonance characterization of the silicon resonant accelerometers, they are operated in a self-oscillation loop using the Zurich Instrument HF-2 lock-in amplifier. In the lock-in amplifier, the resonators are oscillated at a certain level of displacement using the PLL and PID blocks, and the frequency outputs of the sensor

are recorded. Figure 5.5 depicts the test set-up for the system-level tests of the silicon resonant accelerometers. As shown in Figure 5.5, the sensor module, including the MEMS chip, front-end electronics, and temperature sensor, is integrated to the test card. The test card provides the connection to the power supply and the lock-in amplifier. The sensor is driven and sensed by the lock-in amplifier. The test computer provides the control interface for the lock-in amplifier. The data is plotted and recorded using the control interface of the lock-in amplifier. This test set-up is used for the scale factor measurement, temperature tests, and Allan variance tests at the system level of the silicon resonant accelerometers in this study.

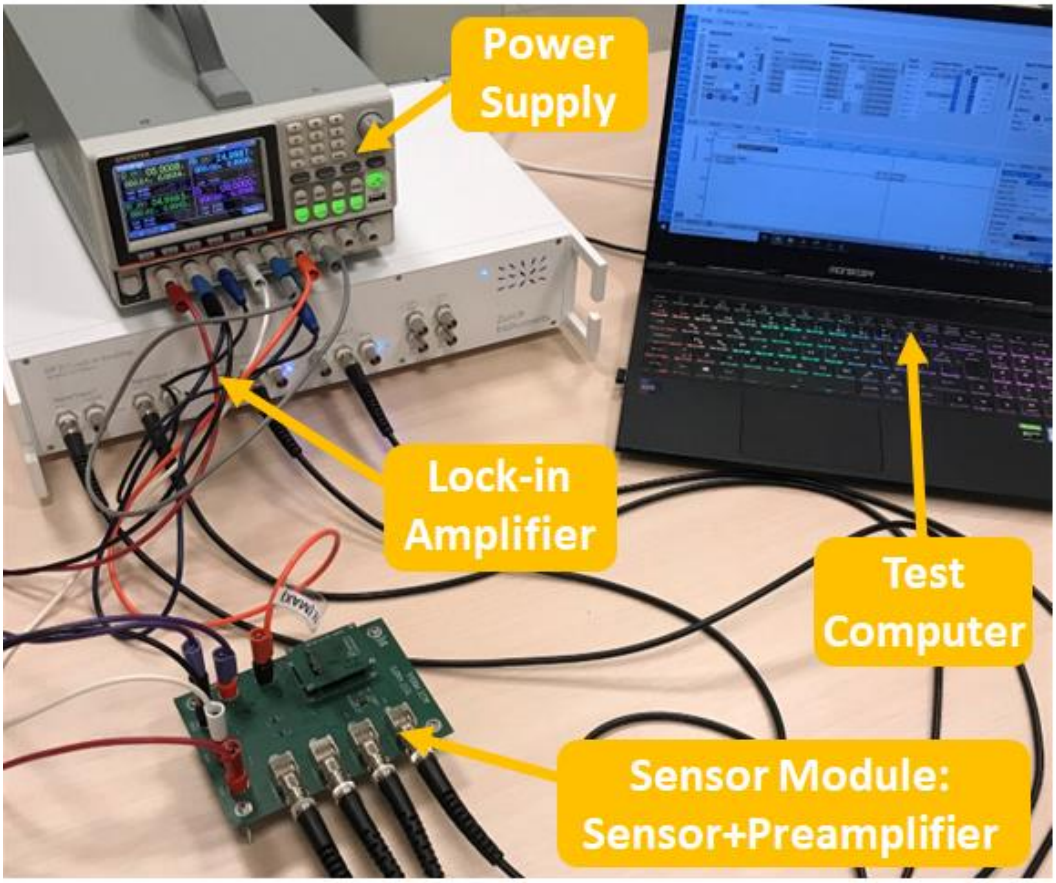


Figure 5.5: Test set-up with the lock-in amplifier for the system-level tests of the silicon resonant accelerometers.

5.3 4-Point Tumble Test for Scale Factor Measurements

The 4-point tumble test is performed to measure the approximate scale factor of the silicon resonant accelerometers by applying a gravity load along the sense axis. Figure 5.6 shows the schematic of the test set-up used for the 4-point tumble test. In this test, the test PCB is rotated by hand along the non-sense axis of the sensor with a 90° angle step, and the sense axis is exposed to the gravity loads between +1 g and -1 g.

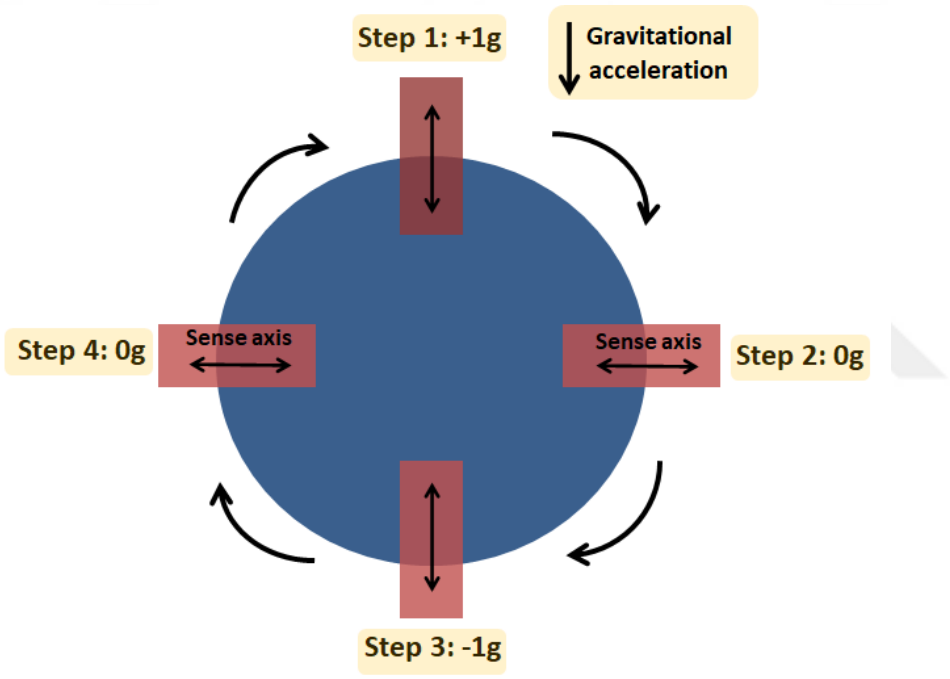


Figure 5.6: Schematic of test set-up for the 4-point tumble test.

The tumble test is applied to each accelerometer one by one to measure the scale factor of the corresponding sensor. Figure 5.7 demonstrates the frequency variations of the differential DETF resonators of the accelerometer Acce#1 in response to the applied gravity loads along the measurement axis. The class of the accelerometer Acce#1 is SRA Design-1, which does not employ microlevers in the sensor structure.

According to the 4-point tumble test results, the scale factor of the accelerometer Acce#1 is found to be 12.44 Hz/g for the differential output.

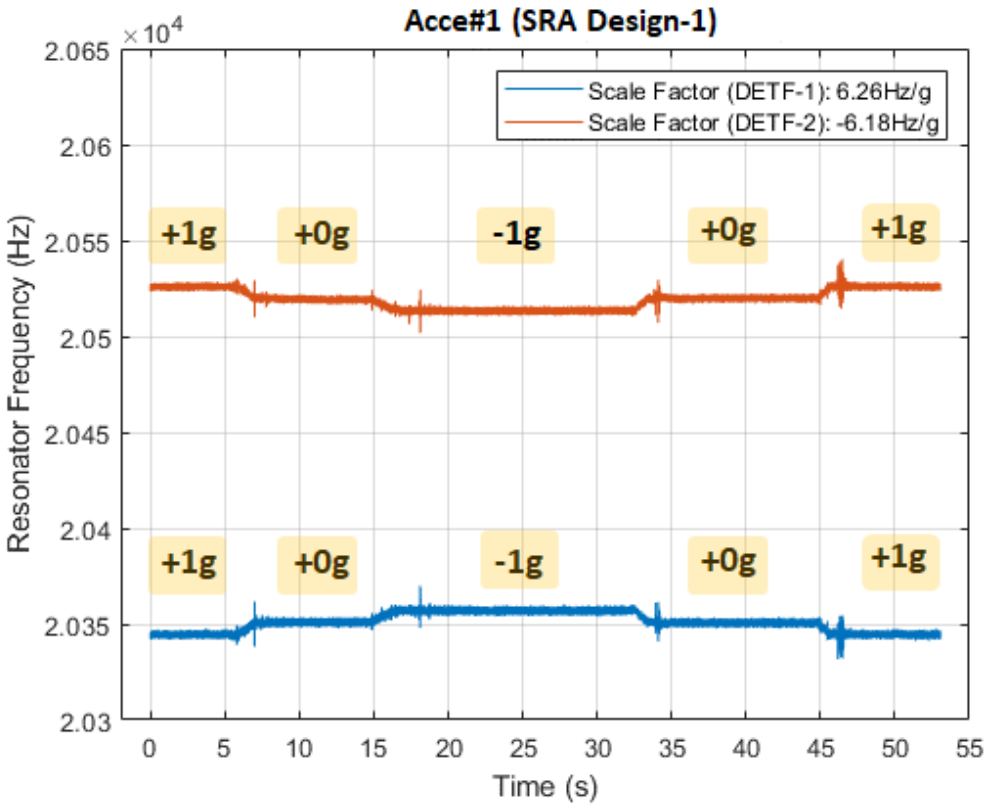


Figure 5.7: The differential DETF resonator outputs of the accelerometer Acce#1 as a response to the different gravity loads in the tumble test.

Figure 5.8 shows the frequency variations of the differential DETF resonators of the accelerometer Acce#2 in response to the applied gravity loads along the measurement axis. The class of the accelerometer Acce#2 is SRA Design-2, which employs microlevers in the sensor structure. According to the tumble test results, the scale factor of the accelerometer Acce#2 is found to be 63.8 Hz/g for the differential output.

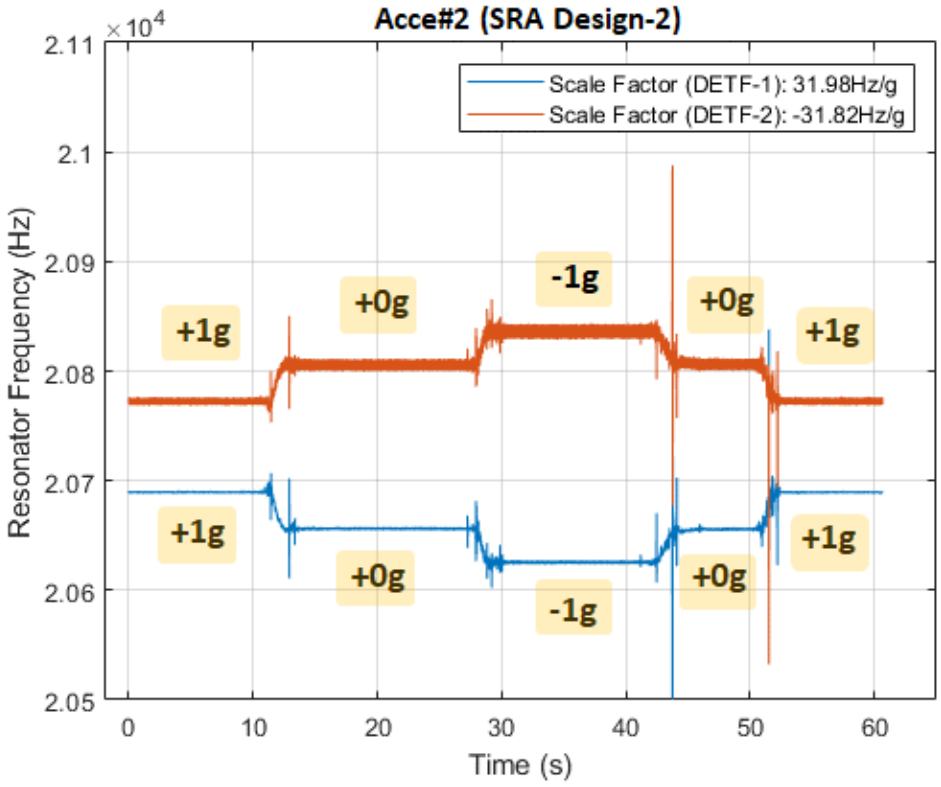


Figure 5.8: The differential DETF resonator outputs of the accelerometer Acce#2 as a response to the different gravity loads in the tumble test.

Figure 5.9 shows the frequency variations of the differential DETF resonators of the accelerometer Acce#3 in response to the applied gravity loads along the measurement axis. The class of the accelerometer Acce#3 is SRA Design-3, which employs microlevers in the sensor structure. According to the tumble test results, the scale factor of the accelerometer Acce#3 is found to be 73.54 Hz/g for the differential output.

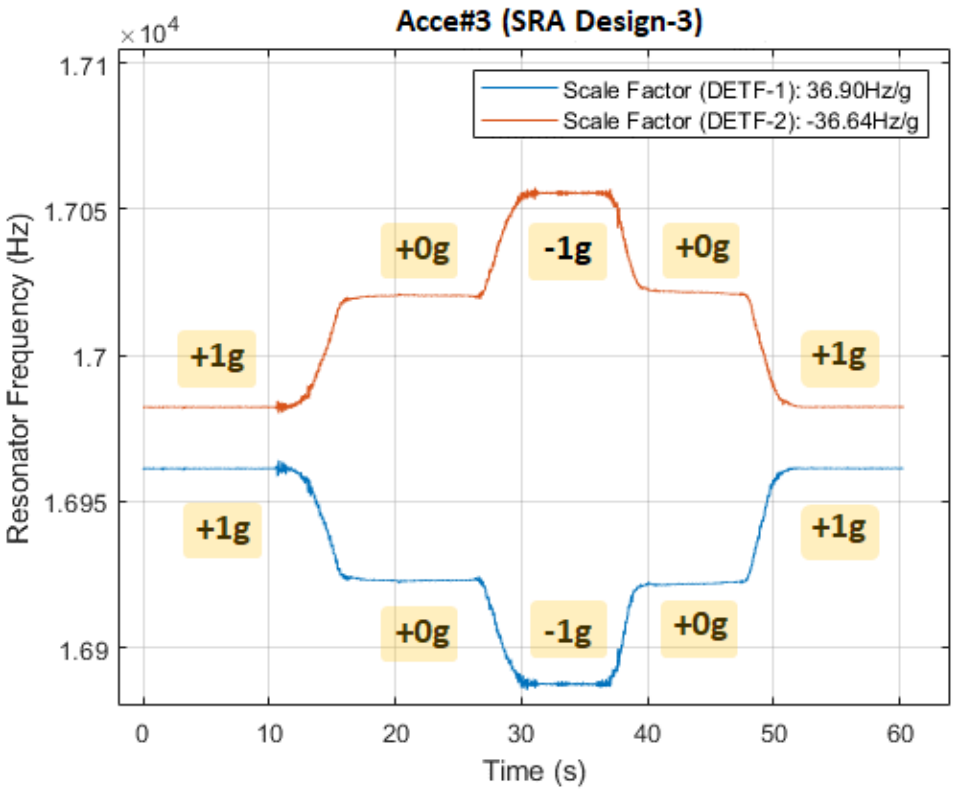


Figure 5.9: The differential DETF resonator outputs DETF resonators of the accelerometer Acce#3 as a response to the different gravity loads in the tumble test.

Figure 5.10 shows the frequency variations of the differential DETF resonators of the accelerometer Acce#4 in response to the applied gravity loads along the measurement axis. The class of the accelerometer Acce#4 is SRA Design-3, which employs microlevers in the sensor structure. According to the tumble test results, the scale factor of the accelerometer Acce#4 is found to be 96.05 Hz/g for the differential output. Table 5.3 gives a summary of the scale factor measurements for the all-tested silicon resonant accelerometers.

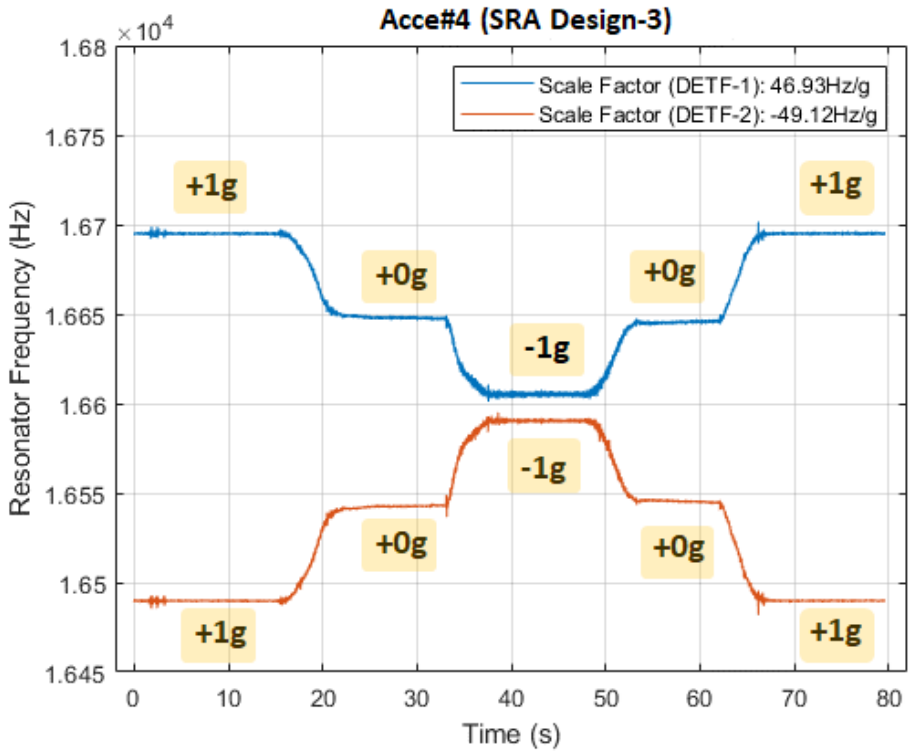


Figure 5.10: The differential DETF resonator outputs DETF resonators of the accelerometer Acce#4 as a response to the different gravity loads in the tumble test.

Table 5.3 Results for the scale factor measurements of the silicon resonant accelerometers.

Sensor No	Resonator	Scale Factor of Single Resonator (Hz/g)	Scale Factor of Differential Output (Hz/g)
Acce#1 (SRA Design-1)	R1	6.26	12.44
	R2	-6.18	
Acce#2 (SRA Design-2)	R1	31.98	63.80
	R2	-31.82	
Acce#3 (SRA Design-3)	R1	36.90	73.54
	R2	-36.64	
Acce#4 (SRA Design-3)	R1	46.93	96.05
	R2	-49.12	

The cross-axis sensitivities of the silicon resonant accelerometers are measured by applying the gravity loads between +1 g and -1 g to the non-sensitive axes of the accelerometers. The non-sensitive axes of the accelerometers are the other two axes, which are orthogonal to the measurement axis. However, the cross-axis sensitivity test for the single-axis accelerometer gives the result of the axis misalignment errors rather than the cross-axis sensitivities. The measured axis misalignment errors are caused by the misalignment of the sensor chip to the sensor module card and the misalignment of the sensor module to the test card. Therefore, the tested accelerometer measures some portion of the gravity vector when the gravity load is applied to the orthogonal axes of the sense axis for the cross-sensitivity measurement. Table 5.4 shows the cross-axis sensitivity or the equivalent axis misalignment measurement results of the silicon resonant accelerometers, assuming that the measurement axis is the axis for the sensors.

Table 5.4 Results for the cross-axis sensitivity or the equivalent axis-misalignment measurements for the silicon resonant accelerometers.

Sensor No	Res.	Cross-axis Sensitivity with y-axis	Cross-axis Sensitivity with z-axis	Equivalent Axis Misalignment with y-axis	Equivalent Axis Misalignment with z-axis
Acce#1 (SRA Design-1)	R1	-2.56%	0.74%	-25.7mrad	7.4mrad
	R2	-2.50%	0.73%	-25.0mrad	7.32mrad
Acce#2 (SRA Design-2)	R1	0.87%	-2.20%	8.7mrad	-22.0mrad
	R2	0.88%	-2.23%	8.8mrad	-22.3mrad
Acce#3 (SRA Design-3)	R1	1.31%	1.35%	13.1mrad	13.5mrad
	R2	1.40%	1.36%	14.0mrad	13.6mrad
Acce#4 (SRA Design-3)	R1	2.79%	-1.22%	27.9mrad	-12.2mrad
	R2	2.84%	-1.21%	28.4mrad	-12.1mrad

5.4 Temperature Tests

The main goal of this study is to develop a low-bias drift silicon resonant accelerometer with a low thermal sensitivity to replace its capacitive counterparts. Thus, the temperature tests are crucial for verifying the performance parameters of the sensors developed in the scope of this thesis. The temperature tests were done using the "ESPEC SH-662" oven located in the METU-MEMS facility, which has a temperature range of -40 °C to +85 °C. Figure 5.11 depicts the temperature test set-up placed inside the test oven. The frequency read-out circuit was implemented using the lock-in amplifier, as shown in Figure 5.5.

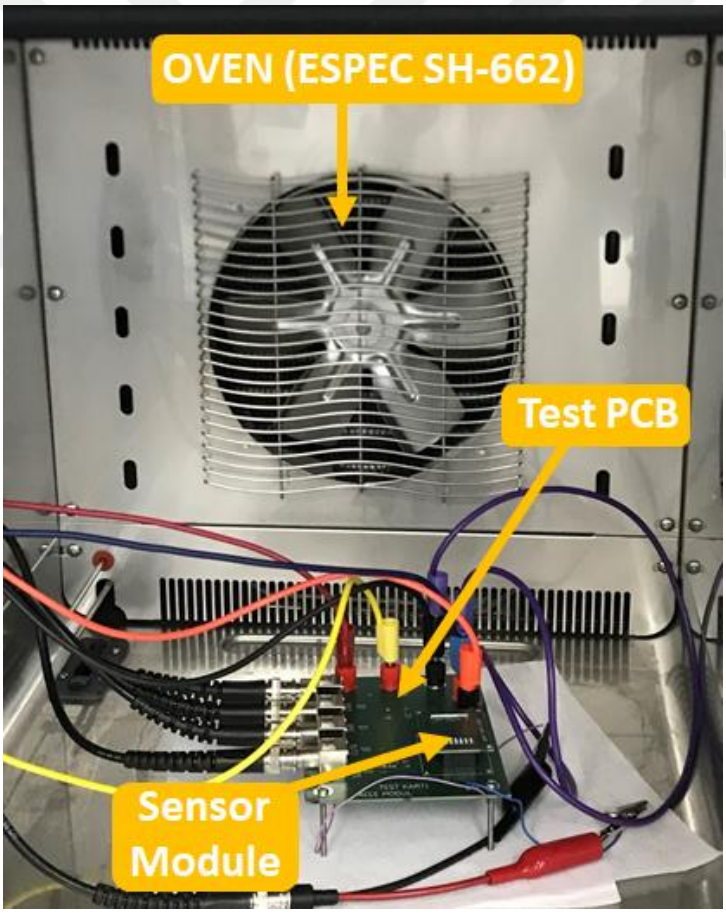


Figure 5.11: Test set-up for the temperature test of the silicon resonant accelerometers.

The temperature test is applied to each accelerometer one by one to measure the temperature sensitivity of the corresponding sensor. Figure 5.12 depicts the temperature test results of the accelerometer Acce#1, which belongs to the SRA Design-1 class. The temperature test results of the accelerometer Acce#1 show that the temperature characteristics of the two DETF resonators are quite different from each other. This difference can be explained by the deflection or crack of the beams connecting the proof mass to the stationary outer frame due to the stress, as mentioned in Section 3.2. The maximum change in the differential output of the accelerometer Acce#1 is measured to be 2033 mg for the temperature range from -40 °C to +85 °C.

Figure 5.13 demonstrates the temperature test results of the accelerometer Acce#2, which belongs to the SRA Design-2 class. Similar to the accelerometer (N4P7), the DETF resonators of the accelerometer Acce#2 give different responses to the temperature variation due to the stress caused by the stationary outer frame. The maximum change in the differential output of the accelerometer Acce#2 is measured to be 121.9 mg for the temperature range from -20 °C to +85 °C. The sensor frames of the SRA Design-1 and SRA Design-2 are similar: the proof mass is connected to the stationary outer frame. As explained in Section 3.2, these accelerometers have thermal stress after they have been manufactured.

The stress problems in SRA Design-1 and SRA Design-2 led to the development of a resonant accelerometer structure located on a single anchor, namely SRA Design-3. Figure 5.14 shows the temperature test results of the accelerometer Acce#3, which belongs to the SRA Design-3 class. According to the test results, the shift in the resonance frequencies of both DETF resonators is about 14.8 Hz for the temperature variation from -40 °C to +85 °C, and both resonators have the same temperature characteristics. So, the maximum change in the differential output of the accelerometer Acce#3 is measured to be 5.4 mg for the whole temperature range. This corresponds to an improvement factor of approximately 20 to 400 over the accelerometers Acce#2 and Acce#1, respectively.

Figure 5.15 depicts the temperature test results of the accelerometer Acce#4, which also belongs to the class of the SRA Design-3. Similar to the accelerometer Acce#3, both resonators have the same temperature characteristics, and the maximum shift in the resonance frequency of each resonator is about 12.8 Hz in the maximum temperature range. The maximum change in the differential output of the accelerometer Acce#4 is measured to be 4.2 mg for the temperature variation from -40 °C to +85 °C.

To compare the results of the silicon resonant accelerometers with the capacitive ones, the temperature characteristic of a typical commercial capacitive MEMS accelerometer developed at Mikrosistemler is analyzed. Figure 5.16 shows the temperature test results of a capacitive MEMS accelerometer for the temperature range from -32 °C to +55 °C. For the given temperature range, the tested capacitive accelerometer had a maximum output change of 110 mg.

Table 5.5 gives the summary of the temperature test results of four silicon resonant accelerometers and one capacitive MEMS accelerometer. Although the accelerometers in SRA Designs-1 and SRA Designs-2 suffer from thermal stress, SRA Design-3 overcomes this issue thanks to the single-anchor device structure, resulting in excellent temperature performance. Compared to the results of the capacitive ones, the temperature sensitivity of the SRA Design-3 accelerometers is at least 20 times better than that of their capacitive counterparts. So, the temperature tests show that the silicon resonant accelerometers developed in this study are much less sensitive to temperature than the capacitive ones.

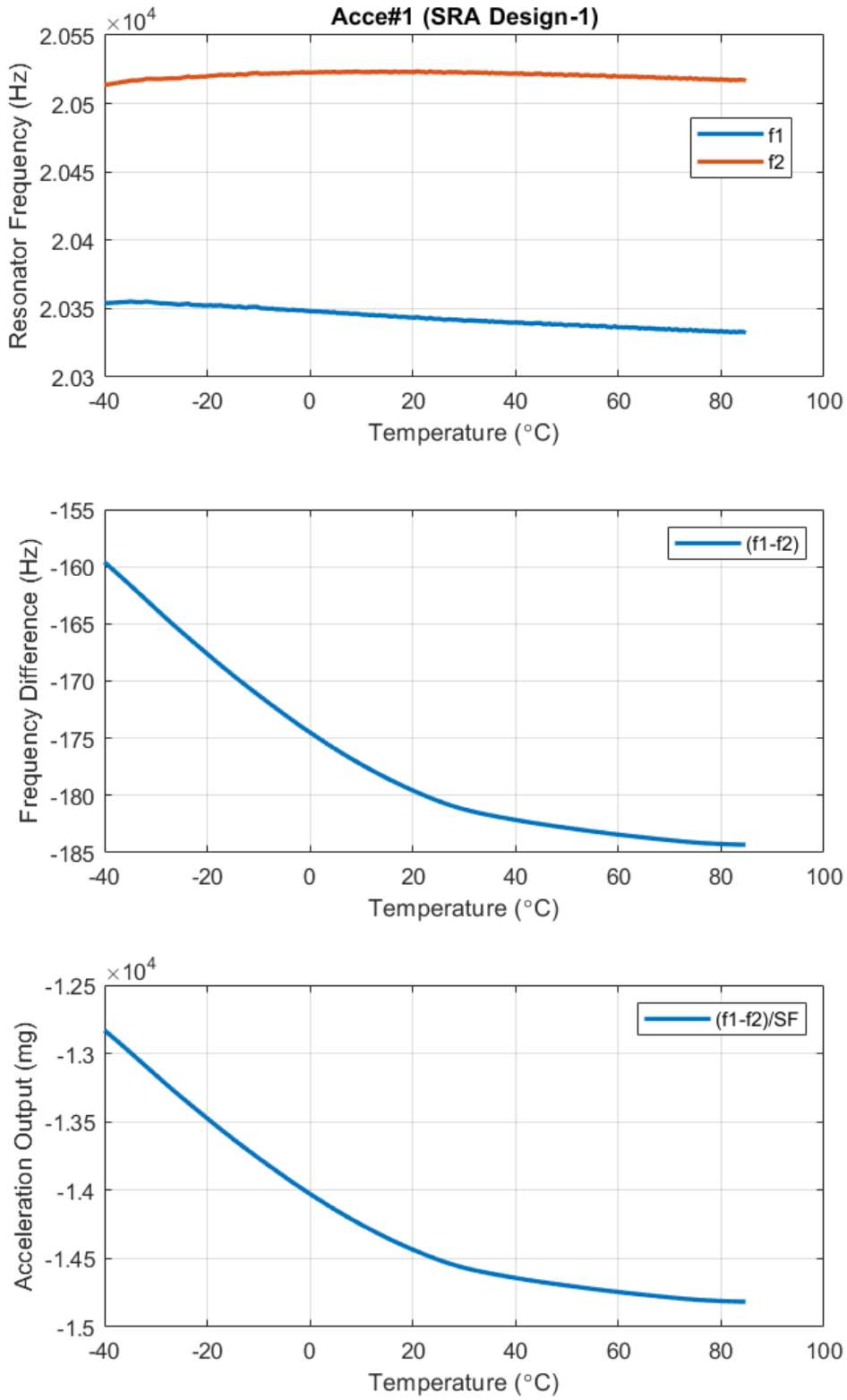


Figure 5.12: Temperature characteristics of the accelerometer Acce#1.

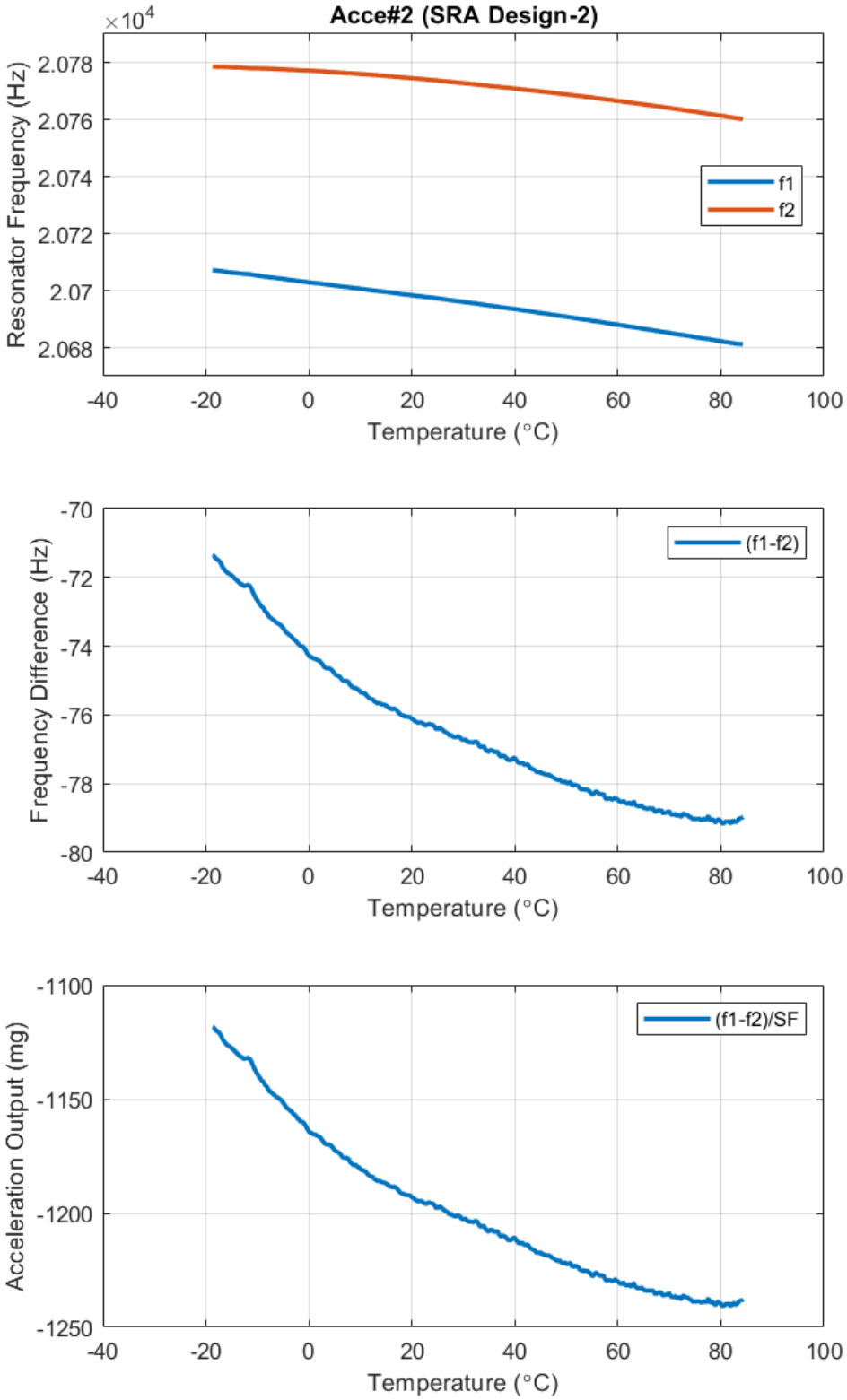


Figure 5.13: Temperature characteristics of the accelerometer Acce#2.

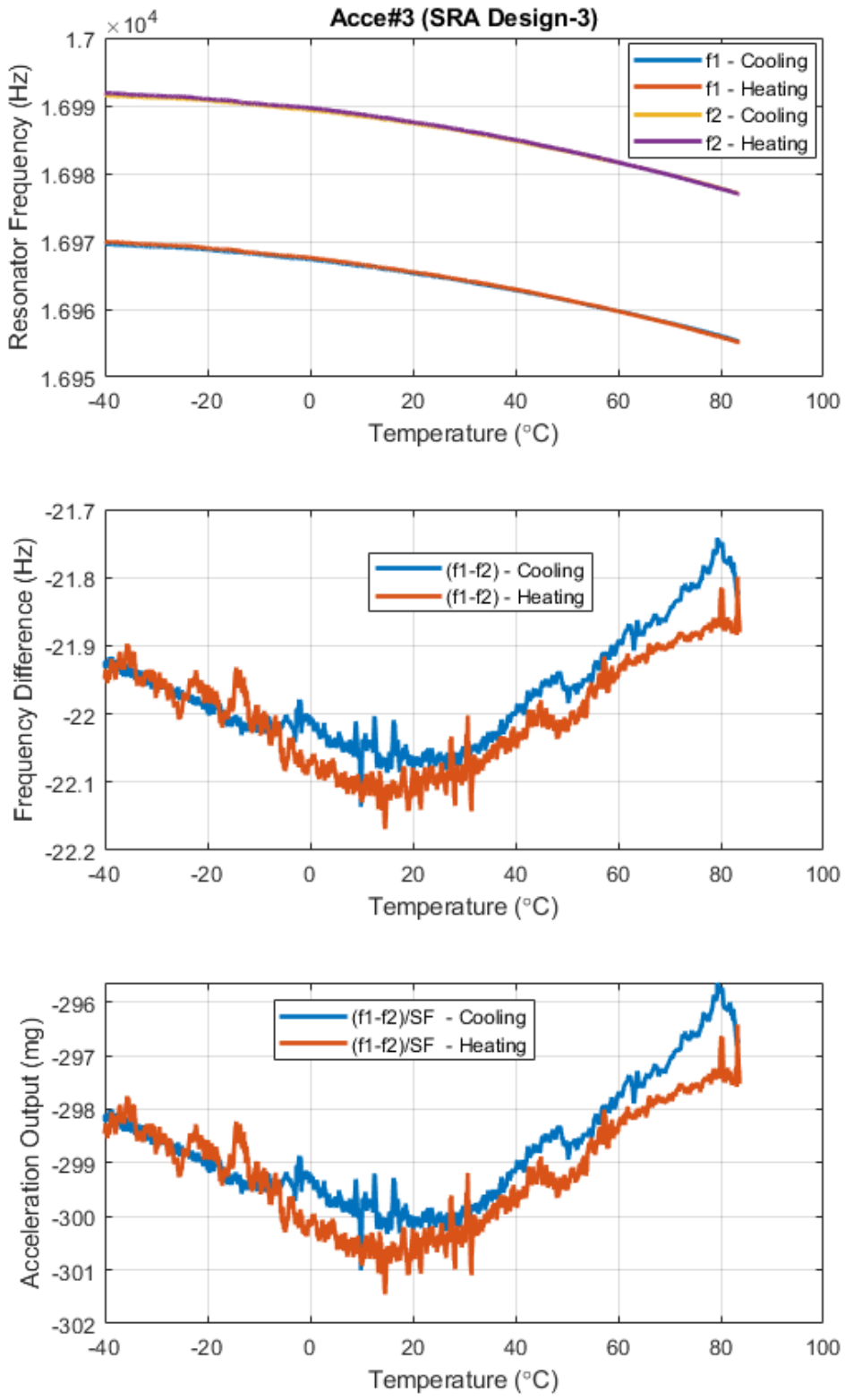


Figure 5.14: Temperature characteristics of the accelerometer Acce#3.

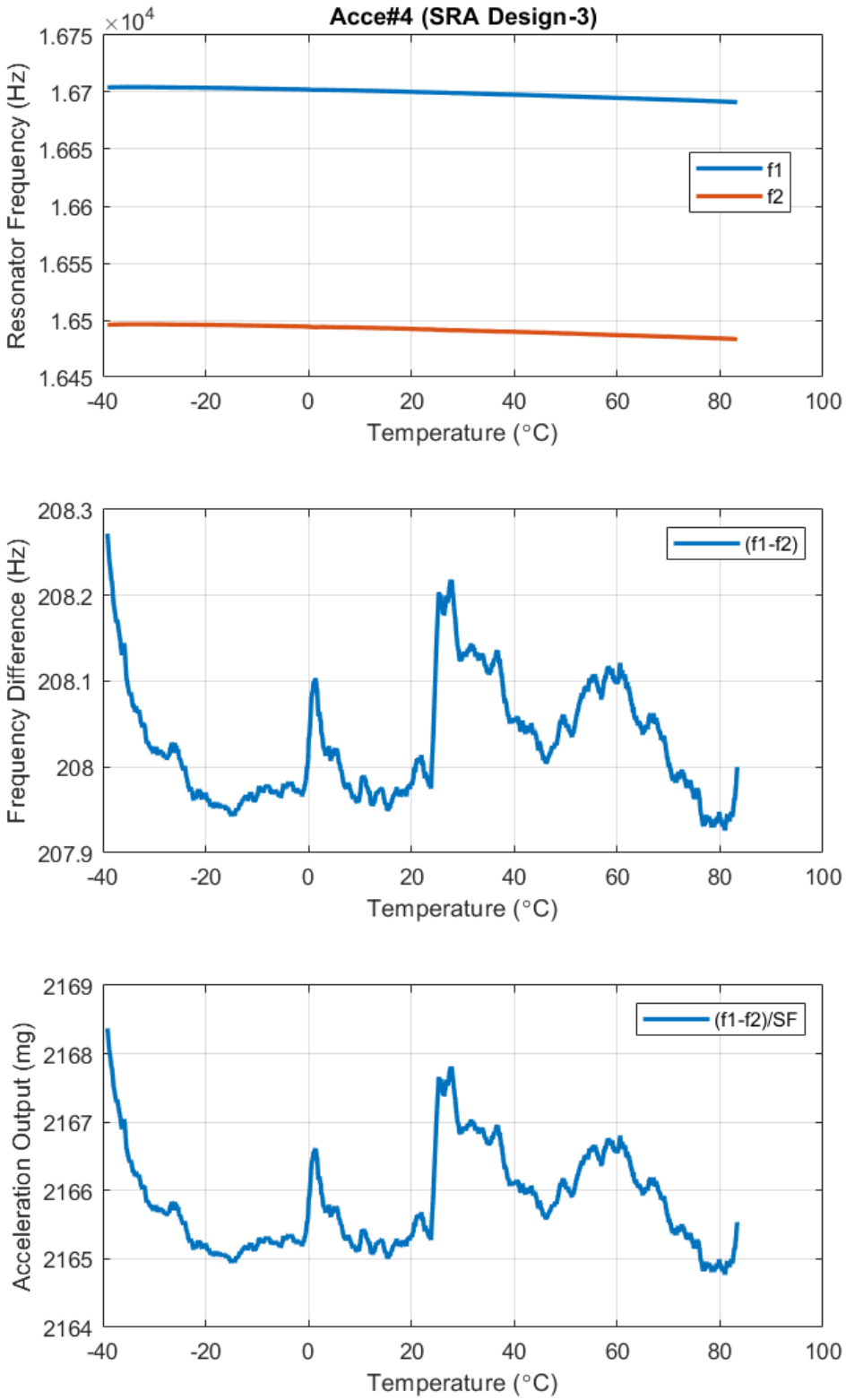


Figure 5.15: Temperature characteristics of the accelerometer Acce#4.

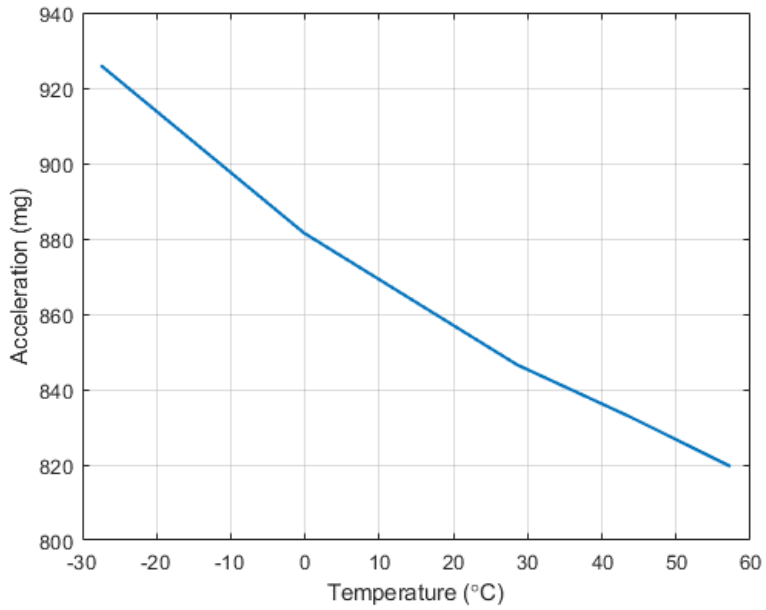


Figure 5.16: Temperature characteristics of a typical commercial MEMS accelerometer developed by Mikrosistemler for the temperature range from -32°C to +55 °C.

Table 5.5 Temperature test results of the silicon resonant accelerometers.

Sensor No	Temp. Range	Res.	Max. Freq. Change for Sing. Output	Max. Freq. Change for Diff. Output	Max. Acc. Change for Diff. Output
Acce#1 (SRA Design-1)	-40°C +85°C	R1	-25.4Hz	-25.3Hz	2033mg
		R2	+3.3Hz		
Acce#2 (SRA Design-2)	-20°C +85°C	R1	-26.0Hz	-7.8Hz	-121.9mg
		R2	-18.4Hz		
Acce#3 (SRA Design-3)	-40°C +85°C	R1	-14.8Hz	+0.4Hz	5.4mg
		R2	-14.8Hz		
Acce#4 (SRA Design-3)	-40°C +85°C	R1	-12.8Hz	+0.4Hz	4.2mg
		R2	-12.8Hz		
Cap.	-32°C +55°C	-	-	-	110mg

5.5 Allan Variance and Bias Repeatability Tests

The Allan variance technique is used to assess the performance characteristics of accelerometers, including velocity random walk (VRW) and bias instability. VRW is the accumulation of velocity inaccuracy over time owing to white noise in acceleration., while bias instability represents the smallest measurable acceleration. Figure 5.17 displays a general Allan variance plot. In this plot, the intersection points of the line with a slope of -0.5 and an average duration of 1 corresponds to the velocity random walk, whereas the lowest value of Allan deviation corresponds to the bias instability. The right side of the Allan deviation graph shows how fast the output of the accelerometer drifts over time. Thus, the more horizontal the right side of the graph stays, the better the long-term stability of the sensor.

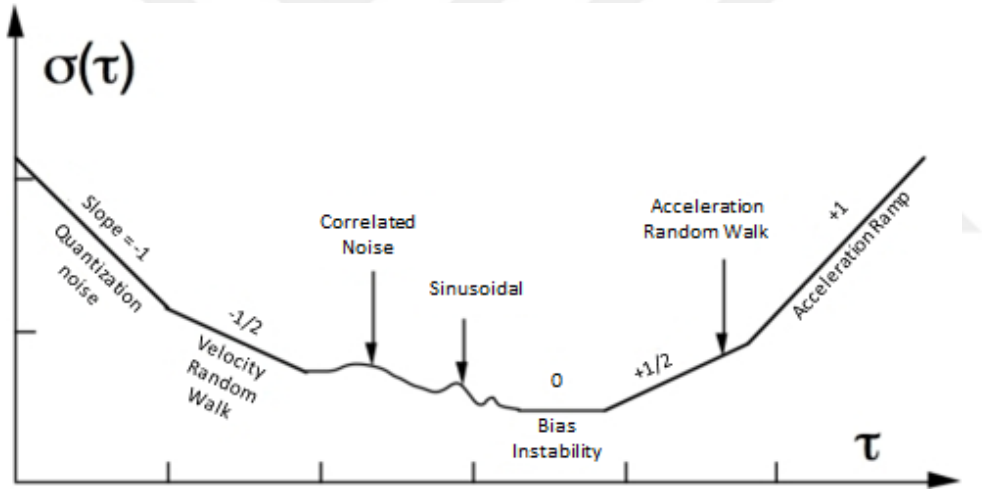


Figure 5.17: A general Allan variance plot for accelerometer.

The Allan variance test is performed by collecting data from the sensor in a stationary position for a set period of time and then evaluating the collected data using the Allan variance method. In this study, the Allan variance performance of each accelerometer is measured. Figure 5.18 demonstrates the Allan variance plots of the accelerometers Acce#1 and #Acce#2 at room temperature. The bias instability and VRW performances of the accelerometer Acce#1 are measured to be 77 μg and

245 µg/√Hz, respectively. On the other side, the bias instability and VRW performances of the accelerometer Acce#2 are measured to be 3.4 µg and 16.5 µg/√Hz, respectively. Although the scale factor of the accelerometer Acce#2 is equal to 5 times the scale factor of the accelerometer Acce#1, the noise performance of the accelerometer Acce#2 is at least 15 times better than the noise performance of the accelerometer Acce#1. This unexpected difference can be explained by the fabrication related mechanical stability problem of the accelerometer Acce#1. Eventually, the right sides of the Allan variance plots of both the accelerometers Acce#1 and Acce#2 do not stay horizontal with increasing averaging time since the biases of both accelerometers drift quickly.

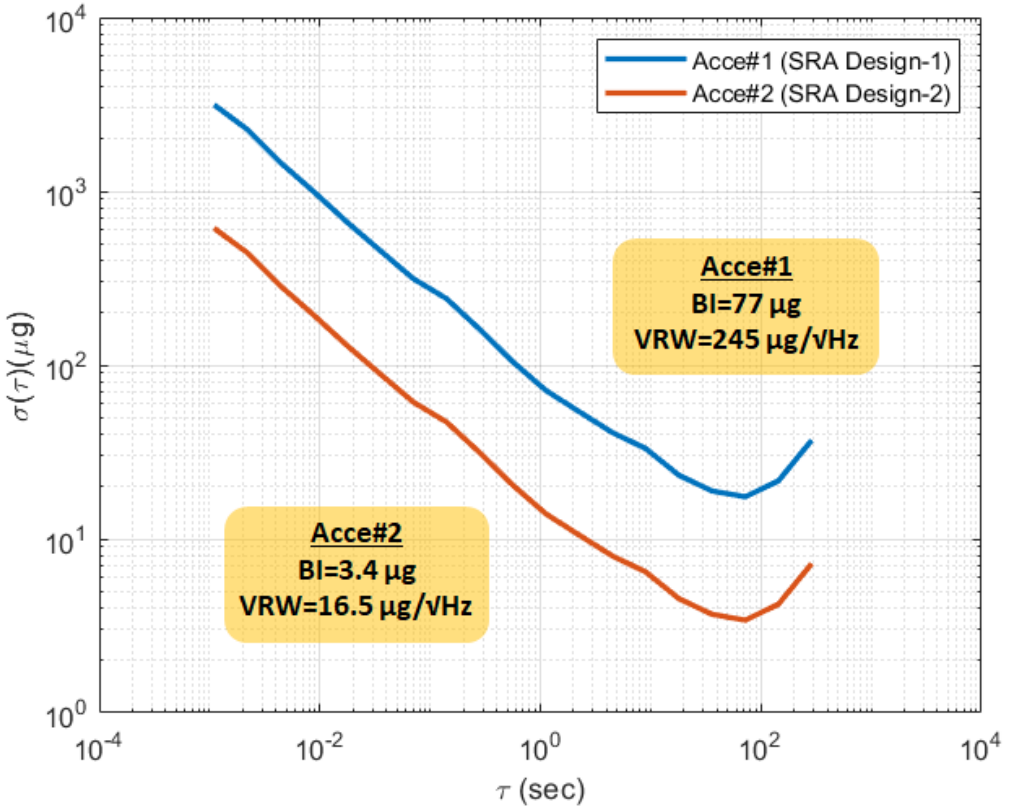


Figure 5.18: Allan Variance plots of the accelerometer Acce#1 and Acce#2 at room temperature.

The single-anchor resonant accelerometer structure, namely SRA Design-3, has significantly improved the bias stability performance of the sensor, suppressing the effects of thermal stress. Figure 5.19 demonstrates the Allan variance plots of the accelerometers Acce#3 and Acce#4 at room temperature. The bias instability and VRW performances of the accelerometer Acce#3 are measured to be 2.98 µg and 11.9 µg/√Hz, respectively. Similarly, the bias instability and VRW performances of the accelerometer Acce#4 are measured to be 1.25 µg and 6.1 µg/√Hz, respectively. As shown in Figure 5.19, the bias deviation remains less than 10 µg even when the averaging time, τ, exceeds 1000s. The horizontal stay on the right side of the Allan variance graphs confirms the long-term stability of the accelerometers.

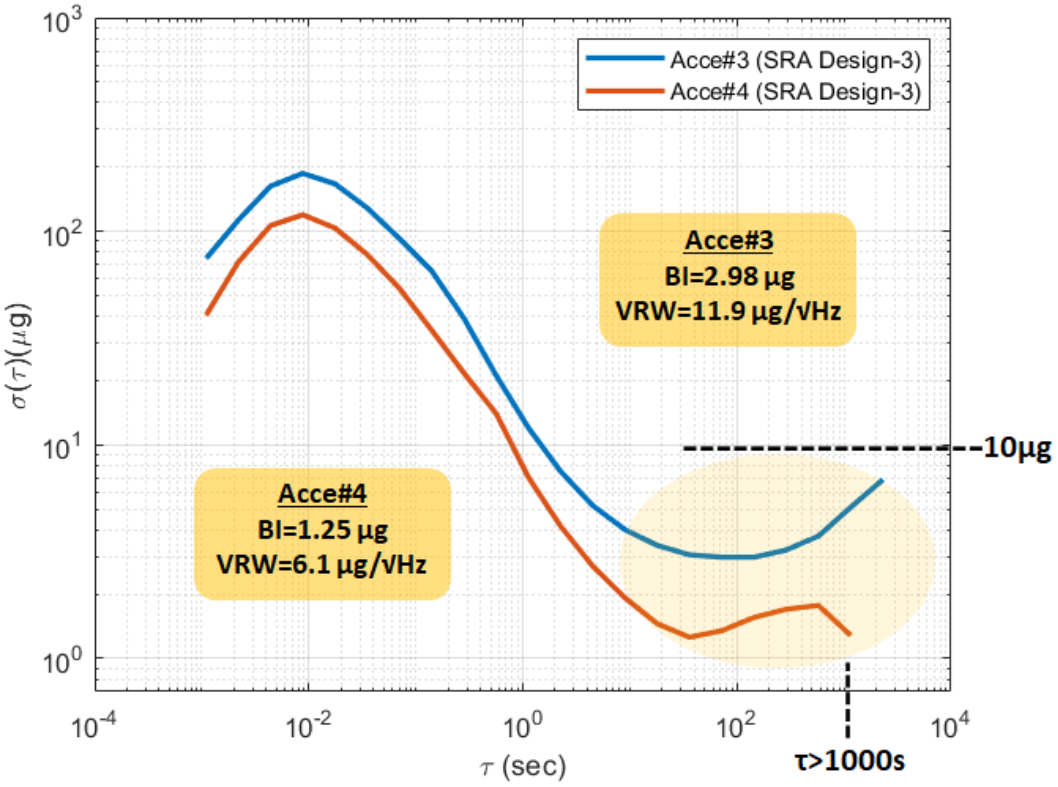


Figure 5.19: Allan Variance plots of the accelerometer Acce#3 and Acce#4 for 10 hour-data at room temperature.

To compare the results of the silicon resonant accelerometers with the capacitive ones, the Allan variance test result of a typical commercial capacitive MEMS accelerometer developed by Mikrosistemler is given. Figure 5.20 depicts the Allan variance plot of the typical capacitive MEMS accelerometer at 25°C in the temperature-controlled environment. The bias instability and VRW performances of the corresponding accelerometer are measured to be 9.9 µg and 13.1 µg/√Hz, respectively. As shown in Figure 5.20, the bias deviation exceeds 100 µg before the averaging time, τ, reaches to 500s.

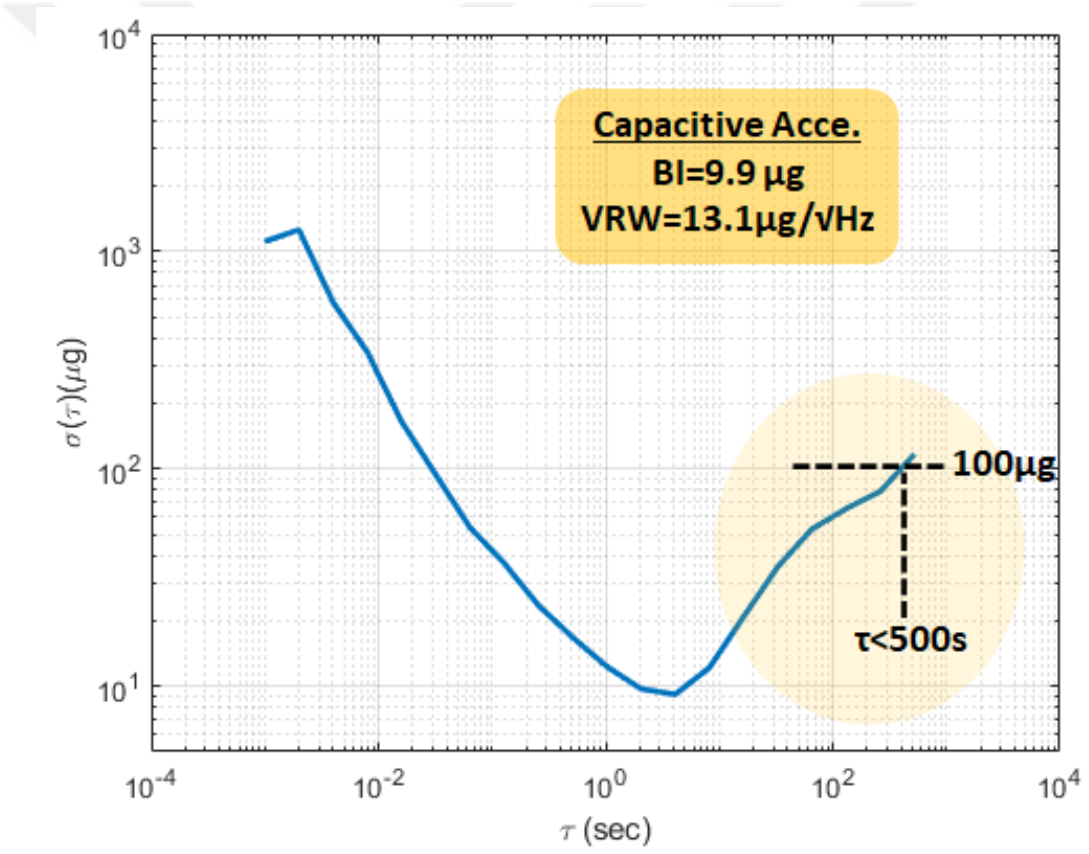


Figure 5.20: Allan Variance plot of the capacitive MEMS accelerometer at 25°C in the temperature-controlled environment.

Figure 5.21 depicts the raw data from the accelerometers Acce#3, Acce#4, and capacitive one, for which the Allan variance plots are shown in Figure 5.19 and Figure 5.20. The bias of the accelerometer Acce#3 shifts 0.15 mg in 11 hours at room temperature. The 1-hour and 10-hour bias stabilities of accelerometer Acce#3 are 3.7 μg and 33.7 μg, respectively. Similarly, the bias of the accelerometer Acce#4 shifts 0.25 mg in 10 hours at room temperature. The 1-hour and 10-hour bias stabilities of accelerometer Acce#4 are 2.8 μg and 26.6 μg, respectively. On the other hand, the bias of the capacitive accelerometer shifts 1.7 mg in 50 minutes at 25 °C in a temperature-controlled cabin. The 1-hour bias stability of the commercial capacitive MEMS accelerometer is 315 μg.

The repeatability of the bias is evaluated for the accelerometer Acce#3 and Acce#4 at the room temperature and for the commercial capacitive sensor at the constant 25 °C. During this test, data is collected from the corresponding sensor for 15 minutes at the stationary position, then, the power is shut down to cool for 15 minutes. This cycle is repeated for 5 times. The bias repeatability is calculated by taking the standard deviation of the 5 bias measurements. Table 5.6 shows the bias repeatability test results of the evaluated accelerometers.

Table 5.6 Bias repeatability test results of the evaluated accelerometers.

Test No	**Acce#3 (SRA Design-3)**	**Acce#4 (SRA Design-3)**	**Capacitive (Calibrated)**
Measurement #1	-299. 964 mg	2166.772 mg	-0.408 mg
Measurement #2	-299. 968 mg	2166.779 mg	-0.369 mg
Measurement #3	-299. 969 mg	2166.768 mg	-0.347 mg
Measurement #4	-299. 957 mg	2166.764 mg	-0.327 mg
Measurement #5	-299. 952 mg	2166.763 mg	-0.309 mg
Bias repeatability	7.3 μg	6.6 μg	38.3 μg

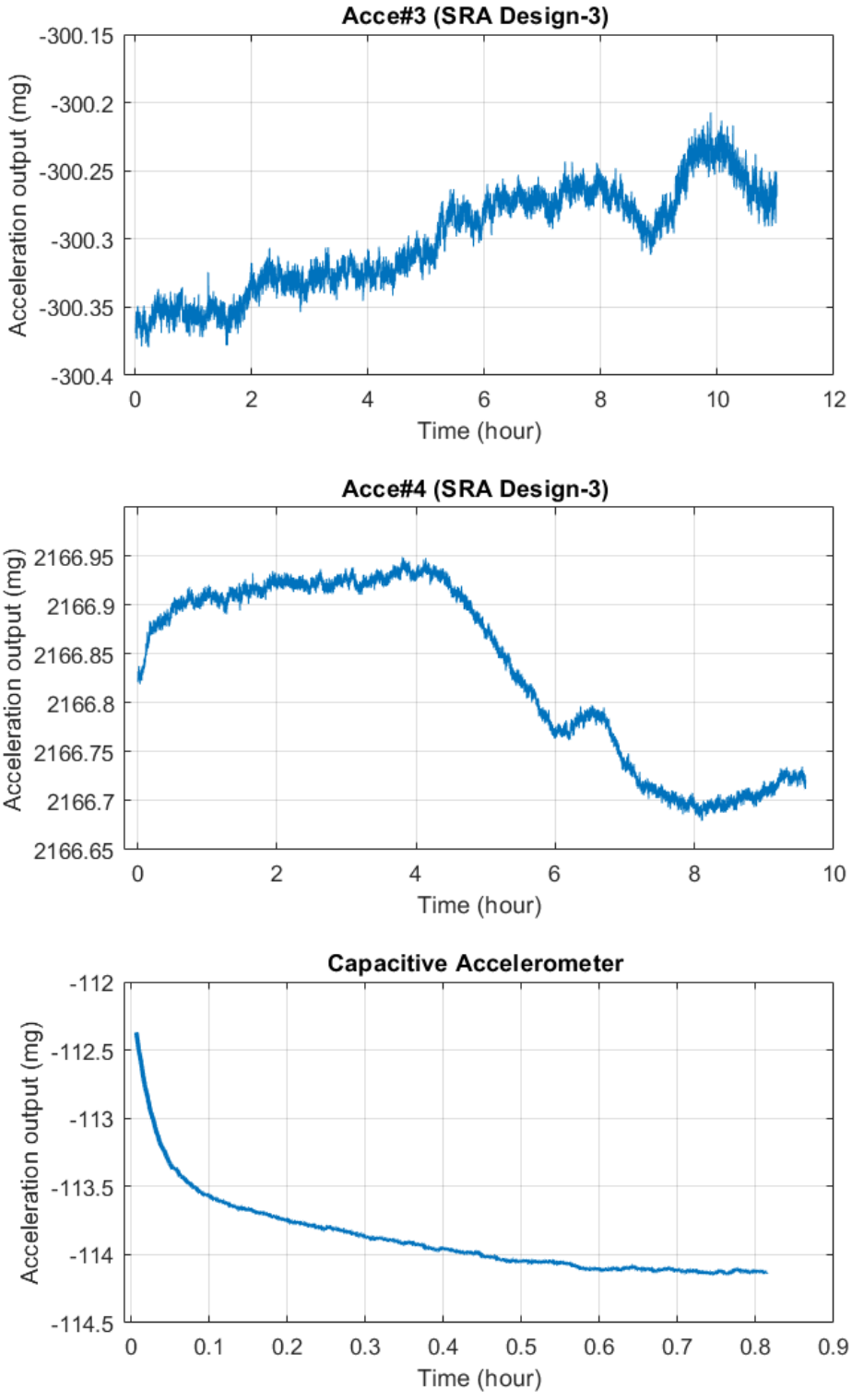


Figure 5.21: Comparison of the raw data of SRA Design-3 accelerometers and the typical commercial capacitive MEMS accelerometer developed by Mikrosistemler.

Table 5.7 summarizes the Allan variance results of four silicon resonant accelerometers and one capacitive MEMS accelerometer. Due to the stress effect, the bias drifts of the accelerometers in SRA Design-1 and SRA Design-2 are higher than expected. However, the single-anchor device structure of the accelerometers in SRA Design-3 makes them very stable over time.

Table 5.7 Comparison of the Allan variance results of the accelerometers

Sensor No	Condition	Bias Instability (μg)	Velocity Random Walk (μg/√Hz)	1-hour bias stability (μg)	Bias Repeatability (μg)
Acce#1 (SRA Design-1)	Room Temp.	77	245	-	-
Acce#2 (SRA Design-2)	Room Temp.	3.4	16.5	-	-
Acce#3 (SRA Design-3)	Room Temp.	2.98	11.9	3.7	7.3
Acce#4 (SRA Design-3)	Room Temp.	1.25	6.1	2.8	6.6
Capacitive	25°C, constant	9.9	13.1	315.4	38.3

5.6 Summary of Test Results

This chapter presented the test results of the silicon resonant accelerometers. Firstly, the resonance characterization results of the studied sensors are demonstrated. Then, the scale factor measurement results are given for the corresponding accelerometers. Next, the temperature characteristics of the sensors are shown. Finally, the Allan variance and bias repeatability test results of the silicon resonant accelerometers

were provided. Moreover, the test results of the silicon resonant accelerometers are compared with one of the commercial capacitive MEMS accelerometers developed by Mikrosistemler. Table 5.8 gives a summary of the test results for the studied accelerometers. Test results have confirmed that the SRA Design-3 accelerometers show excellent performance in terms of temperature sensitivity and bias stability compared to the capacitive ones. Furthermore, their noise performance is even better than that of their capacitive counterpart.

Table 5.8 Summary of the test results of the accelerometers.

Sensor No	**Res.**	**Res. Freq (Hz)**	**SF (Hz/g) (diff.)**	**Max. Acc. Output Change w/Temp. (mg)**	**BI (µg)**	**VRW (µg/√Hz)**	**Bias Stab. (1-h) (µg)**	**Bias Rep. (µg)**
Acce#1 (SRA Design-1)	R1	20344	12.4	2033 (-40°C /+85°C)	77	245	-	-
	R2	20525						
Acce#2 (SRA Design-2)	R1	20689	63.8	-121.9 (-20°C /+85°C)	3.4	16.5	-	-
	R2	20772						
Acce#3 (SRA Design-3)	R1	16964	73.5	5.4 (-40°C /+85°C)	2.98	11.9	3.7	7.3
	R2	16986						
Acce#4 (SRA Design-3)	R1	16763	96.1	4.2 (-40°C /+85°C)	1.25	6.1	2.8	6.6
	R2	16480						
Capacitive	-	-	-	110 (-32°C /+55°C)	9.9	13.1	315.4	38.3

CHAPTER 6

CONCLUSION

This research work presents the design and experimental verification of low temperature drift silicon resonant accelerometers for tactical grade applications. The working principle of a silicon resonant accelerometer is based on force sensing, in which the sensor output is a frequency proportional to the input acceleration. The stress-insensitive sensor design prevents the thermal stress produced by the mismatch of the thermal expansion coefficients (CTE) of glass and silicon in the device from transmitting to the DETF resonators. In the scope of this thesis, three different silicon resonant accelerometer structures are sequentially designed, fabricated, characterized, and tested with the frequency readout circuit. The first sensor structure consists of two DETF resonators and a large proof mass connected to a stationary outer frame. The second sensor structure utilizes microlevers to magnify the inertial force acting on the DETF resonators in addition to the sensor frame of the first sensor structure. Although specially designed stress release beams are implemented in the first and second sensor structures, they suffer from thermal stress caused by the stationary outer frame. In the third sensor design, the sensor structure is placed on a specially designed single anchor to overcome the stress problem encountered in the first two sensor designs. The FEM simulations are performed to analyze and optimize the mode shapes, force sensitivity, and temperature sensitivity of the sensor structures. The designed resonant accelerometers are fabricated using the aMEMS1 process with wafer-level hermetic encapsulation. The fabricated sensor chips are integrated with the capacitive preamplifier and digital signal processor (DSP)-based phase-locked-loop (PLL) system implemented on a Zurich Instrument HF-2 lock-in amplifier. The functionalities of the accelerometers are verified by the resonance and 4-point tumble

tests, and their performances are experimentally evaluated in terms of bias stability and thermal sensitivity by temperature and Allan variance tests.

The following are the findings and achievements of this study:

1. There are several design concerns for a silicon resonant accelerometer to satisfy the requirements for high-end applications. A large-scale factor for high acceleration sensitivity, vacuum packaging for minimizing phase noise, low stiffness nonlinearity, and temperature sensitivity for low-bias drift are needed to achieve a high-performance silicon vibrating beam accelerometer. Among these challenges, the thermal stress on the sensing element caused by the thermal expansion coefficient difference between the glass and silicon is the most important problem limiting the long-term stability of the sensor. Although there are different approaches for improving the thermal sensitivity of the silicon resonant accelerometers, such as implementing a micro-oven and calibrating the sensor output with external temperature sensor or an additional resonator, the most effective way is to optimize the sensor structure to minimize the temperature drift of resonant accelerometers. This work presents a low-temperature drift silicon micromachined resonant accelerometer mounted on a single anchor with specially designed stress release beams. The tested accelerometers provide lower thermal sensitivity, lower bias drift, and better noise performance compared to their commercial capacitive counterparts developed by Mikrosistemler.
2. The mechanical model of the silicon resonant accelerometer is investigated. The force sensitivity of the DETF resonators and mathematical equations microlever mechanism are analyzed, and the acceleration sensitivity of the overall sensor system is determined. The acceleration sensitivity of the resonant accelerometer is proportional to the length of the DETF flexures and inversely proportional to the width of the flexures. However, these device parameters are limited by the sensor fabrication process. A single-stage microlever mechanism helps to amplify the inertial force acting on the sensing beams. Operating the DETF resonators in out-of-phase mode

improves the quality factor and drive efficiency of the resonators. The separation between the in-phase and out-of-phase mode frequencies of the DETF resonator is adjusted by the dimension of the base beam connecting to flexures to prevent the interaction of two modes. The stiffness nonlinearity of DETF flexures is proportional to the beam length and oscillation amplitude and inversely proportional to the beam width. The device parameters are determined considering the force sensitivity of the DETF resonators, so the stiffness nonlinearity of the sensing beams is minimized by adjusting the oscillation amplitude. The flexures of the DETF resonators are excited at the resonance using the varying overlap area type capacitors. Although the varying-gap type capacitor provides higher capacitive sensitivity than the varying-overlap type capacitor, the electrostatic spring effect in the varying-gap type capacitor would pose a problem for the frequency stability of the resonator output.

3. Three different silicon resonant accelerometer architectures are designed based on the theoretical analysis of the mechanical model. The same DETF resonator design is used in each sensor structure. The in-phase and out-of-phase mode resonance frequencies of the DETF resonator are 21787 Hz and 23185 Hz, respectively. The first silicon accelerometer design (SRA Design-1) has a basic structure comprising two DETF resonators and a large proof mass connected to a stationary outer frame. The differential scale factor of this structure is calculated to be 11.2 Hz/g and simulated to be 11.0 Hz/g in FEM analysis. The second silicon accelerometer design (SRA Design-2) utilizes microlevers integrated into the proof mass to increase force sensitivity, in addition to the sensor structure of the first design. The differential scale factor of this structure is calculated to be 48.3 Hz/g and simulated to be 46.3 Hz/g in FEM analysis. The thermal stress-related problems of the first and second sensor designs led to a silicon resonant accelerometer mounted on a single anchor with specially designed stress release beams, namely the third silicon resonant accelerometer design (SRA

Design-3). The differential scale factor of the third structure is calculated to be 33.6 Hz/g and simulated to be 32.5 Hz/g in FEM analysis. The stress release beams are optimized on each device structure by thermal simulations in COMSOL. A realistic temperature simulation model is constructed for the third-generation silicon resonant accelerometer, and the thermal sensitivity of the accelerometer output is simulated for the silicon and glass anchor cases.

4. The designed silicon resonant accelerometers are fabricated using a wafer-level hermetic encapsulation process, namely the aMEMS1 process. In this process, the sensor structure is manufactured by Mikrosistemler using their patented Silicon-on-Glass (SOG) process, then it is vacuum packaged with an SOI cap wafer. After the fabrication of the first and second silicon resonant accelerometer designs, a deflection or crack on the springs connecting the proof mass to the stationary outer frame is observed because of the thermal expansion coefficient difference between glass and silicon after the anodic bonding. This problem is solved by using a single-anchor sensor design, SRA Design-3. During the fabrication of the sensor wafer, the technical problems associated with the DRIE system caused imbalanced etching of the DETF flexures on the sensor structure, resulting in wider capacitive gaps and narrower spring widths. This problem led to a resonance frequency difference between the DETF resonators of some sensor chips.
5. The fabricated silicon resonant accelerometers are chip-level characterized through the resonance tests. While the resonance frequencies of the DETF resonators in the first and second design sensors are measured to be about 20 kHz, the ones in the third design sensors are measured to be about 17 kHz. This resonance frequency difference arises from the imbalance and harsh etching in the latest DRIE processes during the fabrication of the SRA Design-3 accelerometers. The quality factors of the tested accelerometers range between 45,000 and 60,000, ensuring the inside of the sensor is vacuumed.

6. The chip-level characterized silicon resonant accelerometers are integrated with the capacitive preamplifier and a DSP-based phase-locked-loop (PLL) system implemented on a Zurich Instrument HF-2 lock-in amplifier. The capacitive preamplifier is preferred instead of the resistive one to improve the signal-to-noise ratio of the sensor system. The phase-locked loop (PLL) maintains the oscillation of the DETF resonator, and the automatic gain control loop adjusts the amplitude of the oscillation. The measurement bandwidth of the accelerometer is determined by the closed-loop bandwidth of the PLL, which is set to 33 Hz for this study. The amplitude of oscillation displacement for the DETF resonators is adjusted to 0.25 μm, avoiding the nonlinear stiffness effect of the flexures.
7. The functional silicon resonant accelerometers integrated into the frequency readout circuit undergo a series of tests to evaluate their performances in terms of scale factor, bias stability, noise, and temperature sensitivity. The accelerometer Acce#1 (SRA-Design-1) has a differential scale factor of 12.44 Hz/g, a bias instability of 77 μg, a velocity random walk of 245 μg/√Hz, and the maximum bias change of this sensor is about 2033 mg for the temperature range from -40 °C to +85 °C. The accelerometer Acce#2 (SRA-Design-2) exhibits a differential scale factor of 63.8 Hz/g, a bias instability of 3.4 μg, a velocity random walk of 16.5 μg/√Hz, and the maximum bias change of this sensor is about 121.9 mg for the temperature range from -20 °C to +85 °C. The utilization of the microlevers in the SRA-Design-2 greatly improves the bias instability and noise performances of the sensor due to the higher scale factor. However, the performances of the accelerometers Acce#1 and Acce#2 are still below their potential due to stress related problems during the sensor fabrication. The accelerometer Acce#3 (SRA-Design-3) shows a differential scale factor of 73.5 Hz/g, a bias instability of 2.98 μg, a bias stability of 3.7 μg, a bias repeatability of 7.3 μg, a velocity random walk of 11.9 μg/√Hz, and the maximum bias change of this sensor is about 5.4 mg for the temperature range from -40 °C to +85 °C.

Similarly, the accelerometer Acce#4 (SRA-Design-3) shows a differential scale factor of 96.1 Hz/g, a bias instability of 1.25 μg, a bias stability of 2.8 μg, a bias repeatability of 6.6 μg, a velocity random walk of 6.1 μg/√Hz, and the maximum bias change of this sensor is about 4.3 mg for the temperature range from -40 °C to +85 °C. The elimination of the stress problem with a single-anchor sensor structure drastically enhances the temperature stability of the accelerometer output. On the other hand, the typical commercial capacitive MEMS accelerometer developed by Mikrosistemler demonstrates a bias instability of 9.9 μg, a bias stability of 315.4 μg, a bias repeatability of 38.3 μg, a velocity random walk of 13.1 μg/√Hz, and the maximum bias change of this type of sensor is about 110 mg for the temperature range from -32°C to +55 °C. Comparing the results of the typical capacitive MEMS accelerometer and the SRA Design-3 accelerometers developed in this thesis, the silicon resonant accelerometers are at least 20 times better in terms of temperature sensitivity, at least 3 times better in terms of bias instability, at least 85 times better in terms of bias stability, and comparable or better in terms of velocity random walk. More importantly, while the bias of the typical capacitive MEMS accelerometer shifts 1.7 mg in 50 minutes at constant 25°C, the biases of SRA Design-3 accelerometers shift less than 0.25 mg in 10 hours at uncontrolled room temperature.

The major achievement of this study is the development of a silicon resonant accelerometer with much better bias drift and thermal sensitivity than its capacitive counterparts to replace them in high-end applications. Table 6.1 shows the comparison between this work and the results in the literature. To further improve the performance of the overall system, the following issues can be undertaken as future research topics:

1. The sensor fabrication process should be optimized for the DRIE step. The imbalanced and harsh etching of the device structure causes a frequency difference between the differential DETF resonators, resulting in a larger sensor offset, higher temperature sensitivity, and worse nonlinearity.

2. Device structure should be improved to increase the scale factor or the acceleration sensitivity of the sensor. This enhancement can be done in several ways. One method is to increase the proof mass area by optimizing the out-of-plane modes of the sensor structure. Another method is to implement a two-stage lever mechanism instead of a single-stage one. The noise performance of the overall system might be enhanced by increasing the poor capacitive sensitivity of the motor and sense electrodes of the DETF resonators, because the larger capacitive sensitivity of the electrodes leads to a better signal-to-noise ratio for the system.
3. The fabrication of the silicon resonant accelerometers using an all-silicon wafer-level packing process completely eliminates the thermal stress effects on the device structure. The aMEMS2 process [62] is a glass-free, all-silicon wafer-level fabrication and hermetic encapsulation technique for MEMS devices, consisting of two SOI wafers. However, this process is not appropriate for the fabrication of the devices with large area because of the inadequate thickness of the buried oxide layer as an anchor height. The aMEMS2 process should be optimized for the fabrication of the silicon resonant accelerometers. Alternatively, using the cavity SOI wafer instead of the standard SOI wafer might enable the fabrication of the silicon resonant accelerometers with the aMEMS2 process.

4. A low-noise frequency readout circuit should be developed on the PCB to commercialize the silicon resonant accelerometers as a product. The PLL circuit should be optimized to improve the noise performance of the system.

Table 6.1 Comparison between this work and results in the literature.

	[40]	**[19]**	**[29]**	**[22]**	**[48]**	**[45]**	**Cap.**	**This Work**
Year	2015	2016	2016	2017	2019	2020	2021	
Res. Freq. (kHz)	20	26	22.1	800	20	138.4	-	16.8
Scale Factor (Hz/g)	127	10	160	427	361	516	-	96
Range (g)	±20	±10	±20	-	±14	-	±30	±60
Bias Temp. Sens. (µg/°C)	35	65	-	203	4.4	420	1264	31
Temp. Range (°C)	-40/ +60	+5/ +95	-	-20/ +80	+30/ +60	-40/ +60	-32/ +55	-40/ +85
Bias Stability (µg)	11.5	-	10	-	1.77	-	315	2.8
Bias Inst. (µg)	4	-	1	-	0.06	-	9.9	1.25
VRW (µg/√Hz)	-	>100	13	-	-	-	13.1	6.6
Vacuum Pack. Method	Die-level	Wafer-level	Wafer-level	Wafer-level	Die-level	Die-level	Wafer-level	Wafer-level

REFERENCES

[1] A. Morcelli, S. Ferri, and A. Hofmeister, “MEMS: From a Bright Past Towards a Shining Future,” in *Silicon Sensors and Actuators*, B. Vigna, P. Ferrari, F.F. Villa, E. Lasalandra, S. Zerbini, Eds. Springer, Cham, 2022, doi:10.1007/978-3-030-80135-9_27.

[2] T. Divyanshi and B. Supradip, “MEMS Sensor Market Outlook-2026,” *Microelectromechanical System (mems) Sensor Market*, p. 335, 2019.

[3] Refet Firat Yazicioglu, " Surface Micromachined Capacitive Accelerometers using MEMS Technology," MS Thesis, August 2003.

[4] A. A. Seshia, M Palanian, T. A. Roessing, R. T. Howe, R. W. Gooch, T. R. Schimert, and S. Montague, "A Vacuum Packaged Surface Micromachined Resonant Accelerometer," in *Journal of Microelectromechanical Systems*, vol. 11, no. 6, pp. 784-793, Dec. 2002, doi: 10.1109/JMEMS.2002.805207.

[5] M. M. Torunbalci, S. E. Alper, and T. Akin**,** “A Method for Wafer Level Hermetic Packaging of SOI-MEMS Devices with Embedded Vertical Feedthroughs using Advanced MEMS Process,” *Journal of Micromechanics and Microengineering*, Vol. 25, 125030, pp. 1-11, 2015. http://dx.doi.org/10.1088/0960-1317/25/12/125030.

[6] "IEEE Standard Specification Format Guide and Test Procedure for Linear, Single-Axis, Non-Gyroscopic Accelerometers," in *IEEE Std 1293-1998*, vol., no., pp.1-252, 16 April 1999, doi: 10.1109/IEEESTD.1999.89857.

[7]” Inertial Navigation Primer,” Vectornav. Accessed November 17, 2022. [Online]. Available: https://www.vectornav.com/resources/inertial-navigation-primer/theory-of-operation/theory-inertial

[8] Hopkins, R., Miola, J., Sawyer, W., Setterlund, R., Dow, B., "The Silicon Oscillating Accelerometer: A High-Performance MEMS Accelerometer for Precision Navigation and Strategic Guidance Applications," *Proceedings of the 2005 National Technical Meeting of The Institute of Navigation*, San Diego, CA, January 2005, pp. 970-979.

[9] N. S. Michel, "Force Multiplier in a Microelectromechanical Silicon Oscillating Accelerometer," *M.Sc. Thesis,* Massachusetts Institute of Technology, May 2000.

[10] X. L. Le, K. Kim, and S. H. Choa, "Analysis of Temperature Stability and Change of Resonant Frequency of a Capacitive MEMS Accelerometer," *International Journal of Precision Engineering and Manufacturing*, vol. *23*(3), pp. 347–359, 2022, doi.org/10.1007/s12541-021-00602-1.

[11] M. Helsel, G. Gassner, M. Robinson, and J. Woodruff, "A Navigation Grade Micro-Machined Silicon Accelerometer," *Proceedings of 1994 IEEE Position, Location and Navigation Symposium- PLANS'94*, pp. 51-58, 1994, doi: 10.1109/PLANS.1994.303295.

[12] D.W. Burns, R.D. Homing, W.R. Herb, J.D. Zook, and H. Guckel, "Sealed-Cavity Resonant Microbeam Accelerometer," *Sensors and Actuators A: Physical*, vol. 53, no 1–3, pp. 249-255, 1996, doi.org/10.1016/0924-4247(96)01135-1.

[13] T. A. Roessig, R. T. Howe, A. P. Pisano, and J. H. Smith, "Surface-Micromachined Resonant Accelerometer," *Proceedings of International Solid-State Sensors and Actuators Conference (Transducers '97),* pp. 859-862, Chicago, USA, 1997.

[14] R.E. Hopkins, J.T. Borenstein, B. M. Ankowiak, P. A. Ward, R. D. Elliot, M. S. Weinberg, M.S. Depiero, and J. A. Miola, "The Silicon Oscillating Accelerometer: A MEMS Inertial Instrument for Strategic Missile Guidance," *In Proceedings of the Missile Sciences Conference*, Monterey, CA, USA, pp. 45–51, 2000.

[15] S. Seok, H. Kim, and K. Chun, "An Inertial-Grade Laterally-Driven MEMS Differential Resonant Accelerometer," *IEEE SENSORS*, vol.2, pp. 654-657, 2004, doi:10.1109/ICSENS.2004.1426251.

[16] H. C. Kim, S. Seok, I. Kim, S.-D. Choi, and K. Chun, "Inertial grade out-of-plane and in-plane differential resonant silicon accelerometers (DRXLs)," in *13th Int. Conf. Solid-State Sens., Actuators Microsyst. (TRANSDUCERS) Dig. Tech. Papers*, Jun. 2005, vol. 1, pp. 172–175, 2005.

[17] D. Pinto, D. Mercier, C. Kharrat, E. Colinet, V. Nguyen, B. Reig, and S. Hentz, "A Small and High Sensitivity Resonant Accelerometer," *Procedia Chemistry*, vol. 1, no 1, pp. 536-539, 2009, doi.org/10.1016/j.proche.2009.07.134.

[18] C. Comi, A. Corigliano, G. Langfelder, A. Longoni, A. Tocchio and B. Simoni, "A Resonant Microaccelerometer with High Sensitivity Operating in an Oscillating Circuit," in *Journal of Microelectromechanical Systems*, vol. 19, no. 5, pp. 1140-1152, Oct. 2010, doi: 10.1109/JMEMS.2010.2067437.

[19] C. Comi, A. Corigliano, G. Langfelder, V. Zega, and S. Zerbini, "Sensitivity and temperature behavior of a novel z-axis differential resonant micro accelerometer," *Journal of Micromechanics and Microengineering*. vol. 26, pp. 1-11, 2016, doi: 26. 1-11. 10.1088/0960-1317/26/3/035006.

[20] D. L. Christensen et al., "Hermetically Encapsulated Differential Resonant Accelerometer," 2013 Transducers & Eurosensors XXVII: The 17th International Conference on Solid-State Sensors, Actuators and Microsystems (TRANSDUCERS & EUROSENSORS XXVII), Barcelona, Spain, 2013, pp. 606-609, doi: 10.1109/Transducers.2013.6626839.

[21] Y. Yang, E. J. Ng, Y. Chen, I. B. Flader and T. W. Kenny, "A Unified Epi-Seal Process for Fabrication of High-Stability Microelectromechanical Devices," in *Journal of Microelectromechanical Systems*, vol. 25, no. 3, pp. 489-497, June 2016, doi: 10.1109/JMEMS.2016.2537829.

[22] D. D. Shin, C. H. Ahn, Y. Chen, D. L. Christensen, I. B. Flader and T. W. Kenny, "Environmentally Robust Differential Resonant Accelerometer in a Wafer-Scale Encapsulation Process," *2017 IEEE 30th International Conference on Micro Electro Mechanical Systems (MEMS)*, 2017, pp. 17-20, doi: 10.1109/MEMSYS.2017.7863328.

[23] D. D. Shin, Y. Chen, I. B. Flader and T. W. Kenny, "Epitaxially Encapsulated Resonant Accelerometer with an on-Chip Micro-Oven," *2017 19th International Conference on Solid-State Sensors, Actuators and Microsystems (TRANSDUCERS)*, 2017, pp. 595-598, doi: 10.1109/TRANSDUCERS.2017.7994119.

[24] X. Zou, P. Thiruvenkatanathan, and A. A. Seshia, "A High-Resolution Micro-Electro-Mechanical Resonant Tilt Sensor," *Sensors and Actuators A: Physical*, vol. 220, pp. 168-177, 2014, doi: 10.1016/j.sna.2014.10.004.

[25] C. Zhao *et al*., "A Resonant MEMS Accelerometer With 56ng Bias Stability and 98ng/Hz1/2 Noise Floor," in *Journal of Microelectromechanical Systems*, vol. 28, no. 3, pp. 324-326, June 2019, doi: 10.1109/JMEMS.2019.2908931.

[26] M. Pandit *et al*., "An Ultra-High Resolution Resonant MEMS Accelerometer," *2019 IEEE 32nd International Conference on Micro Electro Mechanical Systems (MEMS)*, 2019, pp. 664-667, doi: 10.1109/MEMSYS.2019.8870734.

[27] G. Sobreviela-Falces *et al*., "A Navigation-Grade Mems Vibrating Beam Accelerometer," *2022 IEEE 35th International Conference on Micro Electro Mechanical Systems Conference (MEMS)*, 2022, pp. 782-785, doi: 10.1109/MEMS51670.2022.9699447.

[28] G. M. Xia, A. P. Qiu, Q. Shi and Y. Su, "A Wafer Level Vacuum Packaged Silicon Vibration Beam Accelerometer," *2015 IEEE International Symposium on Inertial Sensors and Systems (ISISS) Proceedings*, 2015, pp. 1-4, doi: 10.1109/ISISS.2015.7102378.

[29] G. Xia, Y. Zhao, J. Zhao, Q. Shi and A. Qiu, "Silicon Vibrating Beam Accelerometer with Ppm Grade Scale Factor Stability and Tens-Ppm Grade Full-Range Nonlinearity," *2016 IEEE International Symposium on Inertial Sensors and Systems*, 2016, pp. 117-118, doi: 10.1109/ISISS.2016.7435560.

[30] J. Zhang, S. D. Jiang, and A. P. Qiu, "Modeling of Nonlinear Stiffness of Micro-Resonator in Silicon Resonant Accelerometer," *In Key Engineering Materials*, vol. 562–565, pp. 374–379, 2013, doi: 10.4028/www.scientific.net/kem.562-565.374.

[31] X. Xiong, W. Zheng, K. Wang, Z. Li, W. Yang and X. Zou, "Sensitivity Enhancement of Mems Resonant Accelerometers by Using Electrostatic Spring," *2020 IEEE International Symposium on Inertial Sensors and Systems (INERTIAL)*, pp. 1-3, 2020, doi: 10.1109/INERTIAL48129.2020.9090015.

[32] Hong Ding, Jiuxuan Zhao and Jin Xie, "A Novel Biaxial Resonant Micro Accelerometer with Microleverage Mechanism," *10th IEEE International Conference on Nano/Micro Engineered and Molecular Systems*, 2015, pp. 50-53, doi: 10.1109/NEMS.2015.7147355.

[33] H. Ding, W. Wang, B. F. Ju, and J. Xie, "A MEMS Resonant Accelerometer with Sensitivity Enhancement and Adjustment Mechanisms," *Journal of Micromechanics and Microengineering*, vol. 27, 2017, doi: 10.1088/1361-6439/aa8d99.

[34] L. He, Y. P. Xu and M. Palaniapan, "A CMOS Readout Circuit for SOI Resonant Accelerometer With 4-μg Bias Stability and 20-μg/Hz−−−√ Resolution," in *IEEE Journal of Solid-State Circuits*, vol. 43, no. 6, pp. 1480-1490, June 2008, doi: 10.1109/JSSC.2008.923616.

[35] Y. Zhao *et al*., "A Sub-μg Bias-Instability MEMS Oscillating Accelerometer with an Ultra-Low-Noise Read-Out Circuit in CMOS," in *IEEE Journal of Solid-State Circuits*, vol. 50, no. 9, pp. 2113-2126, Sept. 2015, doi: 10.1109/JSSC.2015.2431076.

[36] X. Wang *et al*., "A 0.4 μg Bias Instability and 1.2 μg/√ Hz Noise Floor MEMS Silicon Oscillating Accelerometer with CMOS Readout Circuit," in *IEEE Journal of Solid-State Circuits*, vol. 52, no. 2, pp. 472-482, Feb. 2017, doi: 10.1109/JSSC.2016.2609385.

[37] J. Zhao *et al*., "A System Decomposition Model for Phase Noise in Silicon Oscillating Accelerometers," in *IEEE Sensors Journal*, vol. 16, no. 13, pp. 5259-5269, July1, 2016, doi: 10.1109/JSEN.2016.2557458.

[38] J. Zhao, G. Xia, Y. Zhao, A. Qiu and Y. Su, "A low power MEMS-ASIC silicon resonant accelerometor with sub-μg bias instability and ±30g full-scale," *2016 IEEE International Symposium on Inertial Sensors and Systems*, 2016, pp. 46-49, doi: 10.1109/ISISS.2016.7435541.

[39] J. Lee, and J. Rhim, "Temperature Compensation Method for the Resonant Frequency of a Differential Vibrating Accelerometer Using Electrostatic Stiffness Control", *Journal of Micromechanics and Microengineering*, vol. 22, no. 9, 2012. doi:10.1088/0960-1317/22/9/095016.

[40] Z. Jing, Q. Anping, S. Qin, B. You, and X. Guoming, "Research on Temperature Compensation Method of Silicon Resonant Accelerometer Based on İntegrated Temperature Measurement Resonator," *2015 12th IEEE International Conference on Electronic Measurement & Instruments (ICEMI)*, 2015, pp. 1577-1581, doi: 10.1109/ICEMI.2015.7494478.

[41] A. Mustafazade and A. A. Seshia, "Compact High-Precision Analog Temperature Controller for MEMS Inertial Sensors," *2018 IEEE International Frequency Control Symposium (IFCS)*, 2018, pp. 1-2, doi: 10.1109/FCS.2018.8597565.

[42] Y. Guo, Z. Ma, T. Zhang, X. Zheng, and Z. Jin, "A Stiffness-Tunable MEMS Accelerometer," *Journal of Micromechanics and Microengineering*, vol. 31, 2020, doi: 10.1088/1361-6439/abcedb.

[43] R. Shi, J. Zhao, A.P. Qiu, G.M. Xia," Temperature Self-Compensation of Micromechanical Silicon Resonant Accelerometer," *Applied Mechanics and Materials*, vol. 373–375, pp. 373–381, 2013, doi: 10.4028/www.scientific.net/amm.373-375.373

[44] P. Cai, X. Xiong, K. Wang, J. Wang, and X. Zou, "An Improved Difference Temperature Compensation Method for MEMS Resonant Accelerometers," *Micromachines*, vol. 12, no. 9, p. 1022, Aug. 2021, doi: 10.3390/mi12091022.

[45] J. Cui, M. Liu, H. Yang, D. Li and Q. Zhao, "Temperature Robust Silicon Resonant Accelerometer with Stress Isolation Frame Mounted on Axis-Symmetrical Anchors," *2020 IEEE 33rd International Conference on Micro Electro Mechanical Systems (MEMS)*, 2020, pp. 791-794, doi: 10.1109/MEMS46641.2020.9056157.

[46] Y. Yin, Z. Fang, J. Dong, Y. Liu and F. Han, "A Temperature-Insensitive Micromachined Resonant Accelerometer with Thermal Stress Isolation," *2018 IEEE SENSORS*, 2018, pp. 1-4, doi: 10.1109/ICSENS.2018.8630282.

[47] Y. Yin, Z. Fang, Y. Liu, and F. Han, "Temperature-Insensitive Structure Design of Micromachined Resonant Accelerometers," *Sensors*, vol. 19, no. 7, p. 1544, Mar. 2019, doi: 10.3390/s19071544.

[48] Z. Fang, Y. Yin, X. He, F. Han, and Y. Liu, "Temperature-Drift Characterization of a Micromachined Resonant Accelerometer with a Low-Noise Frequency Readout," *Sensors and Actuators A: Physical*, vol. 300, 2019, doi.org/10.1016/j.sna.2019.111665.

[49] Y. Terzioglu, " High Performance Closed-Loop Analog Readout Circuit for Capacitive MEMS Accelerometers," in *M.S. Thesis*, Middle East Technical University, 2015.

[50] U. Aykutlu, " 5th Order Sigma Delta MEMS Accelerometer System with Enhance Linearity," in *M.S. Thesis*, Middle East Technical University, 2015.

[51] K. Azgın and L. Valdevit, “The Effects of Tine Coupling and Geometrical Imperfections on the Response of DETF Resonators.” *Journal of Micromechanics and Microengineering*, vol. 23, 2013, doi: 10.1088/0960-1317/23/12/125011.

[52] Wang, X., Huan, R., Pu, D., and Wei, X., “Effect of Nonlinearity and Axial Force on Frequency Drift of a T-Shaped Tuning Fork Micro-Resonator”, *Journal of Micromechanics and Microengineering*, vol. 28, no. 12, 2018, doi:10.1088/1361-6439/aae9c5.

[53] S. X. P. Su and H. S. Yang, “Analytical Modeling and FEM Simulations of Single-Stage Microleverage mechanism,” International Journal of Mechanical Sciences, vol. 44, pp. 2217-2238, 2002, doi: 10.1016/S0020-7403(02)00162-5

[54] Y. P. Xu, MEMS silicon oscillating accelerometers and readout circuits. River Publishers, 2022.

[55] A. H. Nayfeh and D. T. Mook, Nonlinear oscillation. New York etc.: John Wiley and Sons, 1979.

[56] S. E. Alper, "MEMS Gyroscopes for Tactical-Grade Inertial Measurement Applications," in *Dissertation for the Degree of Doctor of Philosophy*, Middle East Technical University, 2005.

[57] H. D. Gavcar, "Compensation Methods for Quasi-Static Acceleration Sensitivity of MEMS Gyroscopes," in *M.S. Thesis*, Middle East Technical University, 2014.

[58] M. M. Torunbalci, "Development of New, Simple, and Robust Wafer Level Hermetic Packaging Methods for MEMS Sensors," in *Ph.D. thesis*, METU, 2015

[59] M. M. Torunbalci, S. E. Alper, and **T. Akin**, “Advanced MEMS (aMEMS) Process for Wafer Level Hermetic Encapsulation of MEMS Devices using SOI Cap Wafers with Vertical Feedthroughs,” IEEE/ASME Journal of Microelectromechanical Systems, Vol. 24, No. 3, pp. 556-564, June 2015. 10.1109/JMEMS.2015.2406341

[60] E. Tatar, M. M. Torunbalci, S. E. Alper, and T. Akin, “A Method and Electrical Model for the Anodic Bonding of SOI and Glass Wafers,” *The 25th IEEE International Conference on Micro Electro Mechanical Systems (MEMS 2012)*, pp. 68-71, Paris, France, Jan. 29-Feb.2, 2012.

[61] “HF2 User Manual”, Zurich Instrument, Accessed November 20, 2022. [Online]. Available: https://docs.zhinst.com/hf2_user_manual

[62] M. M. Torunbalci, H. D. Gavcar, F. Yesil, S. E. Alper, and T. Akin, "An All-Silicon Process Platform for Wafer-Level Vacuum Packaged MEMS Devices," in IEEE Sensors Journal, vol. 21, no. 13, pp. 13958-13964, 1 July1, 2021, doi: 10.1109/JSEN.2021.3073928.

INTERNATIONAL CONFERENCE PUBLICATIONS

[1] H. D. Gavcar, K.Azgin, S. E. Alper, and T. Akin, “An Automatic Acceleration Compensation System for A Single-Mass MEMS Gyroscope,” *The 18th International Conference on Solid-State Sensors, Actuators and Microsystems (TRANSDUCERS 2015)*, pp. 19-22, Alaska, USA, June 2015, doi:10.1109/TRANSDUCERS.2015.7180850.

[2] S. Sonmezoglu, H. D. Gavcar, K. Azgin, S. E. Alper, and **T. Akin**, “Simultaneous Detection of Linear and Coriolis Accelerations on a Mode-Matched MEMS Gyroscope,” *The 27th IEEE International Conference on Micro Electro Mechanical Systems (MEMS 2014)*, pp. 32-35, San Francisco, U.S.A., January 2014, doi:10.1109/MEMSYS.2014.6765566.

INTERNATIONAL JOURNAL PUBLICATIONS

[1] M. M. Torunbalci, H. D. Gavcar, F. Yesil, S. E. Alper and T. Akin, "An All-Silicon Process Platform for Wafer-Level Vacuum Packaged MEMS Devices," in *IEEE Sensors Journal*, vol. 21, no. 13, pp. 13958-13964, 1 July1, 2021, doi: 10.1109/JSEN.2021.3073928.